

Numerical Modelling and Model Reduction of Heat Flow in Robotic Welding

Mads Martinussen

Master of Science in Engineering Cybernetics

Submission date: July 2007

Supervisor: Jan Tommy Gravdahl, ITK

Co-supervisor: Erik Stiklestad, Aker Verdal

Problem Description

The topic of this thesis is to develop a numerical model of heat flow in robotic welding. The ultimate goal of the work is to apply the model to trajectory planning and speed control of the welding robot, and thereby achieve better quality welds.

Sub tasks:

1. Perform a literature study on robotic welding.
2. Describe the heat flow problem in robotic welding using partial differential equations.
3. Present the finite element method.
4. Use the above methods to develop a numerical model of heat flow. Specifically, provide an estimate of the cooling time from 800 C to 500 C in the seam.
5. Present a number of methods in model order reduction, with particular weight on proper orthogonal decomposition(POD).
6. Perform model reduction of the numerical model using POD, and do an evaluation of the reduced model's general performance.
7. Perform experiments in temperature measurements of welding using an infrared camera. More specifically, there will be performed an evaluation on whether or not this method may be used as a decision parameter in an automated system.

Assignment given: 28. February 2007
Supervisor: Jan Tommy Gravdahl, ITK

Preface

This master's thesis is a compulsory part of the fifth year masters study of engineering cybernetics at NTNU. The project was done in cooperation with Aker Kværner Verdal A/S.

Through the term at which the thesis has been done, I have learnt a lot about the complex nature of welding and the relating fields of study. At the initial point of the project, the framework was not very well defined. This resulted in a lot of work in identifying the nature of the problem, and finding out how to approach it. This resulted in many hours of frustration. When later having similar large projects like this, there will be put more work in finding a proper frame-work.

I would like to thank my supervisor, Jan Tommy Gravdahl, for great support throughout the thesis. I would also like to thank Erik Stiklestad at Aker kværner Verdal A/S for making this project possible. He supported me with relevant information regarding the projects nature. He made the welding experiments with the IR-camera possible, providing equipment and time on the robot gantry. I would also like to thank Øystein Grong for constructive critics of my work, and giving me guidance on how to approach problems related to thermal analysis of welds. A thank you should also be directed toward Svein Hovland for giving me a crash course in model reduction. I would never have been able to complete the work without his help. Last but not least, my fellow students at GG48 have been a great support throughout the entire period, giving me encouraging feedback all the way.

Trondheim, July 18, 2007

Mads Martinussen

Abstract

This thesis is a case study of robotic welding, where the majority of the work has been done on studying the complex nature of the partial differential equations governing the heat distribution in steel plates. In order to get fundamental knowledge about welding and, in principal concern, on the automated side of it, there has been done a general literature study on robotic welding in Chapter 2. Here the major issues concerning welding are covered. The topics covered are equipment used, parameters governing the process and sensors used in automated systems. In Chapter 3, the partial differential equations are introduced, where the basic assumptions in the case of welding are taken, and an analytical solution, valid for thick plates in pseudo steady state is derived. This solution will later in the thesis be used as a reference temperature distribution in order to validate the model made through numerical modelling. The numerical model has been made in a software environment based on the finite element method. As an introduction to this method, Chapter 4 goes through the basic ideas behind the method, and introduces the weak form, a method for solving the weighted integral statement. The basic procedure in making the model, obtaining a $\Delta t_{8/5}$ and comparing the results with the reference model from Chapter 3, are covered in Chapter 6. In Chapter 5 the theory behind some model order reduction techniques are outlined. The main focus will be put on Proper Orthogonal Decomposition. The theory is put into practice in Chapter 7, where a reduced model is obtained through a number of steps based on the model obtained in Chapter 6. As an introductory study to future work on the full automated system, experiments in online measurements of the temperature in the welded specimen are done in Chapter 8. Discussions are done after each relevant chapter and conclusions are drawn in Chapter 9.

Keywords: Robotic welding, welding equipment and parameters, heat flow modelling, the finite element method, $\Delta t_{8/5}$, model reduction, IR-thermography.

Table of Contents

1	Introduction	1
2	A literature study in robotic welding theory	3
2.1	Welding equipment	4
2.1.1	Power source	4
2.1.2	Electrode feed unit	4
2.1.3	Welding torch	4
2.2	Process parameters	5
2.2.1	Current	5
2.2.2	Voltage	5
2.2.3	Welding speed	5
2.2.4	Electrode extension	5
2.2.5	Shielding gas	6
2.2.6	Electrode diameter	6
2.2.7	Welding Angle	6
2.3	Welding sensors	6
2.4	Sensors for technological parameters	7
2.4.1	Arc voltage	7
2.4.2	Welding current	7
2.4.3	Wire Feed Speed	7
2.5	Sensors for geometrical parameters	7
2.5.1	Contact sensors	7
2.5.2	Optical sensors	8
2.5.3	Arc Sensors	8
2.6	Sensors Detecting Temperature	8
3	Heat flow modelling	11
3.1	The general heat flow equation	11
3.2	Heat input and arc efficiency factor	12
3.3	The thick plate solution	12
3.4	Temperature decay rate	15
4	The finite element method	17
4.1	The basic features of the method	18
4.2	The weighted integral and weak form formulations	18

4.2.1	The weighted integral statement	18
4.2.2	The weak form	19
4.2.3	Summary	22
5	Model order reduction	23
5.1	Problem statement	24
5.2	Proper orthogonal decomposition	24
5.3	Rational Krylov algorithms	25
5.4	Fourier model reduction	26
5.5	Balanced realization and truncation	28
6	Numerical modelling and analysis of heat flow in a single-pass butt welding seam	29
6.1	Construction of the model	29
6.2	Response analysis	30
6.2.1	Relation between Q and q_0	30
6.2.2	Relevant Plots	30
6.3	Discussion	32
7	Applying POD to the numerical FEM-model	39
7.1	Linearizing the model	39
7.2	Reducing the order of the model	43
7.2.1	Snapshot matrix from one simulation	43
7.2.2	Snapshot matrix from several initial value simulations	43
7.2.3	Snapshot matrix from several simulations including input u	48
7.2.4	Applying other inputs to the reduced model	48
7.3	Discussion and evaluation	53
8	Temperature experiments at Aker Kværner Verdal	55
8.1	Test rig and set up	55
8.2	Test procedures	55
8.2.1	Session 1	57
8.2.2	Session 2	57
8.2.3	Session 3	57
8.2.4	Session 4	58
8.2.5	Session 5 and 6	60
8.2.6	Session 7 and 8	60
8.3	Hardness testing for quality confirmation	61
8.3.1	Quick review of Vickers hardness test	63
8.3.2	Results from Vickers hardness test	63
8.4	Discussion	63
9	Conclusion	67
9.1	Future work	68
	Bibliography	70

Appendices	70
A Modelling of a single-pass weld	72
A.1 Application modes and modules used in the model	72
A.2 Constants used in the model	72
A.3 Geometries in the model	73
A.4 Geometry 1, 3D	74
A.4.1 Mesh statistics	74
A.4.2 Application mode:Heat Transfer by Conduction (ht)	74
A.5 Geometry 2, 1D	75
A.5.1 Scalar Expressions	75
A.5.2 Mesh statistics	76
A.5.3 Application Mode: Weak Form, Subdomain w	76
A.6 Geometry 3	77
A.7 Materials/Coefficients Library: Steel AISI 4340	77
A.8 Extrusion Coupling Variables: Geom 1, Source Subdomain: 1	78
A.9 Solver Parameters	78
A.9.1 Direct(UMFPACK)	78
A.9.2 Time Stepping	78
A.9.3 Advanced options	79
A.10 Variables	79
A.10.1 Boundary Variables	79
A.10.2 Subdomain Variables	79
B Figures relevant for Chapter 6	81
C Figures relevant to Chapter 7	87
D ThermaCAMTM S65	95
E Results from Vicker 10 hardness test	99
F Sample Welding	103
G Matlab code and FEM-model	105

Chapter 1

Introduction

In today's modern manufacturing where productivity and low cost is equalized with high quality, robots is a mean to improve and maintain these virtues. There has been put a lot of effort into robotics in order to automate welding in recent decades. The major research has been done in fields where landscape mapping is used to control the weld-quality. This is very important in the sense that the weld is performed in the correct area, but doesn't say anything about the temperature distribution in the welded material. It's not certain that the weld is performed under optimal temperature-conditions. Later research has shown that temperature dependent variables are many. Characteristics such as welding residual stress, distortion and micro structural properties follow from temperature affection from the heat source. The temperature distribution during welding and the materials cooling gradient is an important parameter to get the optimal strength in the welded material. This is done best under optimal temperature conditions. The scope of this project is to perform such an analysis and use the gathered information to optimize the weld with respect to the welds' ability to withstand mechanical stress. This is done in such a way that a numerical mathematical model is made through partial differential equations describing the thermal physical behavior of the welded material. The results from these equations, giving a temperature distribution in the specimen, will be used online to control the temperature by the means of manipulating available variables and keeping the temperature on a desired and optimal level.

The describing equations are in their original form complex and difficult to solve. The scope of this project is to make a model which is as simple as possible, but still gives a valid picture of the temperature distribution. This is not straight forward, and modelling is therefore emphasized throughout the report. The model is made in a software environment, which is GUI-based, where models are drawn and governing equations are being tied up to their respective domains. When a satisfactory model is acquired, model reduction will be performed on the model. Reducing the order of the model, makes it more suited for controller design with shorter simulation time. A welding trial with IR-camera will be performed, investigating the possibility of using the camera to gather temperature information from the welded specimen, using it as a decision parameter in the final closed loop control system. A future goal of the project is to implement the system in a live environment, performing welds in a temperature controlled environment.

Chapter 2

A literature study in robotic welding theory



Figure 2.1: A Panasonic robotic welder with 6 Degrees of freedom(DOF).

This chapter will try to express and sort out the basic theory behind basic welding and its applications. It will go through the equipment needed in an automated process, and which welding technique parameters are possible to manipulate in order to perform a weld. There will also be a section describing the sensors that a robotic manipulator use in welding today. The method used here is Gas shielded Flux Cored Metal Arc Welding (G-FCAW). See Fig. 2.2 for more details. The study is based on material found in (Pires

et al. 2006), (Jiluan 2003), (Grong 1994) and (Nguyen 2004).

2.1 Welding equipment

Basic equipment for a G-FCAW is a power source, electrode feed unit, welding torch and shielding gas regulator.

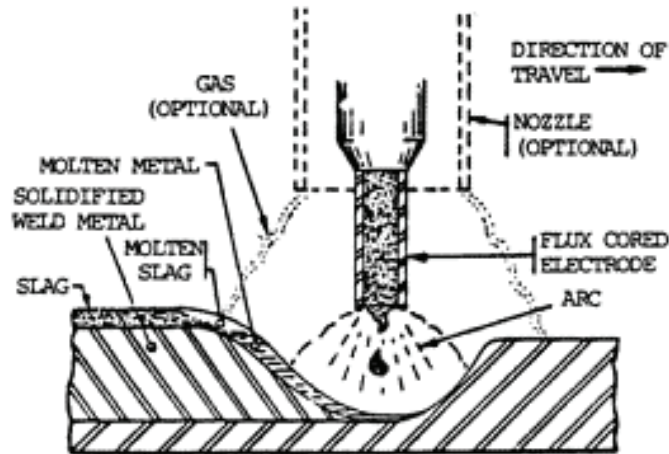


Figure 2.2: Schematic presentation of a G-FCAW welding process

2.1.1 Power source

The power source architecture is of the inverter type. Both the output voltage and the wire feed speed are kept constant. This makes it possible to self-adjust and stabilize the arc-length.

2.1.2 Electrode feed unit

The feed unit and the welding control mechanism will typically be integrated in the same package. The electrode feed unit pulls the electrode from the reel and pushes it through a conduit to the welding torch (gun). In automatic and robotic welding systems, the electrode is fed from a large spool (15-18 kg) or large drum (200-475 kg) to minimize wire supply changing.

The control mechanism regulates the electrode feed, start and stop of the electrode, shielding gas delivery, current and cooling water (when necessary) to the torch.

2.1.3 Welding torch

The torch's main functions are to supply the electrode with electrical current and direct the electrode and gas-flow to the work piece. Main components are the contact tube, the nozzle, the torch switch and the handle. Also included in a robotic manipulator is usually

an emergency-stop mechanism to prevent damage to the robot and the welding torch in the event of a collision. There is also often included an automatic cleaning mechanism.

2.2 Process parameters

The process parameters affect the way the electrode is transferred to the work-piece, arc stability, spatter generation, weld bead geometry and overall weld quality. The parameters, including current, voltage, travel speed and stick out, are not necessarily independent of each other. This means that changing one parameter may effect another one.

2.2.1 Current

Direct current electrode positive (DCEP) is most used in G-FCAW because of stable electric arc, low spatter, good weld bead geometry and great penetration depth. The current in G-FCAW may span from 100 A up to approx 800 A. With high current you get a good burn-in, which is a measure for how deep the Heat Affected Zone (HAZ) is.

2.2.2 Voltage

Arc voltage is directly related to the current. Arc length increases the voltage. The voltage is also dependent on shielding gas and electrode extension.

- Increased arc voltage flattens and widens the weld bead.
- Low arc voltage increases the weld reinforcement.
- Too high voltage can cause arc instability, spatter, porosity and even undercut.

2.2.3 Welding speed

Increased welding speed decreases the linear heat input to the work piece and the filler metal deposition rate per unit of length. Initial increase can cause initially deeper penetration depth, but it will decrease in effect as speed increases, and can cause undercut. This is due to the fact that you don't fill inn the cavity produced by the arc. This means that high welding speed decreases the amount of heat input to the metal.

2.2.4 Electrode extension

This is the electrode length that is outside of the contact tube, also called stick-out. Electrode extension, produced by increase in torch distance to the work-piece for specific parameters set, increases electrode melting rate caused by the Joule effect.

2.2.5 Shielding gas

Shielding gases effect arc-stability, metal transfer mode, weld bead shape and melting rate, but the main purpose is to protect the arc and the weld-pool from effects from the surrounding air. Gases used can be pure gases or mixes of two or more gases for different effects. The most common mixture used in G-FCAW is a mixture of carbon dioxide (CO_2) and Argon (Ar). Aker Verdal uses a mixture of 82% CO_2 and 18% Ar with a supply of 17 – 18 l/min gas into the weld pool (Helden & Dreyer 1999).

2.2.6 Electrode diameter

The electrode, being the wire added to the working piece, can differ in diameter for different purposes. Diameters commonly differs between 0.8 mm and 4 mm. The different ranges of use are thin electrodes for welding thinner materials, and thicker when welding thicker materials. When using a thicker wire, the size of welding pool increases due to the need of higher current.

2.2.7 Welding Angle

Welding may be performed in different angles, differing between $\pm 10^\circ$.

- Forward pointing gives less burn-in and the risk of pores.
- Backward pointing gives a deeper burn-in and less risk of pores.
- By having the gun perpendicular to the welding material, one gets a sufficient burn-in and a low risk of pores. This is the recommended angle to perform a weld in.

2.3 Welding sensors

In welding, and even more so in automated welding, sensor technology play a major part in making the final result satisfactory. The sensors need to be very precise, and also robust because of the hostile environment a robotic welder will work in. The main task of sensors are to provide the manipulators control system with data, which will be used to perform the correct actions according to its task. There are mainly two different kinds of sensors. A third one is added here, relating to the scope of this project:

- Sensors that measure geometrical parameters which are used to control the position and/or speed of the manipulator.
- Sensors measuring voltage, current, wire feed speed and other process-dependent variables.
- Sensors detecting non-mechanical parameters such as temperature.

2.4 Sensors for technological parameters

2.4.1 Arc voltage

Measurements of the arc voltage should be made as close to the welding arc as possible.

2.4.2 Welding current

There is two basic sensors for measuring the current in the welding wire:

- Hall effect sensors.
This sensor consists of a circular core of cast iron where the cable that carries the current flow goes through. The sensor is of non-contact type, and will not affect the current of the welding power source. It is limited in bandwidth, and can be used in applications below 100 kHz and a slew rate of typically $50 A/\mu s$.
- Current shunt.
Using the principle of letting the current flow through a resistor and measuring the voltage across. In order to have as small a loss across the resistor as possible, the problem with noise arises. A small resistor is more sensible to noise, making the shunt sensor less applicable.

2.4.3 Wire Feed Speed

This is a major control parameter to achieve a stable welding process. The most common is to apply a constant voltage and wire feed speed, and let the current adjust itself to that accordingly. This means that a high wire feed speed will produce a high current and vice versa. The wire is being fed by the use of a feeding mechanism, and the speed will be adjusted through this mechanism. The most reliable way of measuring this is through the speed of the feeder system. This may cause a problem if the feeder has some slip or any other uncertainties.

2.5 Sensors for geometrical parameters

This type of sensors are designed to get information about the weld and its groove. This information will then be used to perform seam tracking and quality control. Typical types of information that is desired to gather are deviations from nominal path, orientation changes and gap size. There are four main types of sensors used; touch-, optical-, arc- and electro-magnetical- sensors(Jiluan 2003).

2.5.1 Contact sensors

The typical way these sensors are designed is through a probe detecting deviation of the torch from its position in the groove. The probe is designed with pressure sensors in the tip which detects the direction of deviation. A major flaw of these types of sensors is the

need of a deep and well defined groove. Also needed is special probes for different shaped grooves. This makes this approach bothersome and not well suited for highly adaptive systems.

2.5.2 Optical sensors

Optical sensors can not only detect deviation from the groove, but also the shape of the groove, arc and molten pool. This gives an advantage in comparison to touch sensors. Optical sensors can be further divided into four major categories:

- **Single spot light sensor.**
A light-source using a single beam of light to detect angles, depth and edges of the groove. The source may be photoelectric, infrared, visible or the actual arc.
- **Linear Light Sensors.**
Light is being projected through a lens and a slit onto the surface of the work piece, perpendicular to the weld seam. A camera then detects the shape of the curved line, thus giving an image of the grooves width, depth and centerline.
- **Scanning Light Sensors.**
A laser source is being oscillated over the groove. The image is being captured synchronously by a CCD camera and processed through a computer to give information about groove shape, size and center line.
- **CCD-image Sensors.**
The entire weld pool, including arc, torch and wire tip, are being imaged by a CCD-camera. The imaging system gives information about width, relative wire position with respect to the groove, and wire extension.

Optical sensors in general give a lot of information about the weld groove, and are well designed to be used in adaptive control of the welding parameters.

2.5.3 Arc Sensors

This method of tracking the groove is based on the change of current when the distance between the contact tube and the work-piece varies. When the current is measured through f.ex. a hall sensor, the distance from the work-piece has in practice a proportional relation with the current. This method is based on the assumption that all parameters except the current are held constant throughout the entire welding process. The measurement will in practice be done with a weaving motion over the groove, and gets a variable current giving an image of how the groove looks.

2.6 Sensors Detecting Temperature

The major motivation for using sensors detecting temperature are to gather temperature information about the welded materials to ensure weld-quality. The temperature-field determines the micro structure and mechanical properties of the welded material. Beside

the fact that mathematical modelling may be used, there exists sensors that measure the temperature-field with the help from different techniques. There are three main-types of sensing which are applicable for online use based on infrared radiation:

- **Brightness Method.**
This method is based on the principle that a body effected by temperature will increase in brightness as temperature increases. As a comparison-reference a standard calibrated light source is placed next to the object as a means of visual comparison.
- **Radiation Method.**
This method is based on the principle that the intensity of radiation at a certain wavelength corresponds to its temperature. Subject to drift, which means that calibration is important.
- **Colorimetric Method.**
This method is based on the principle that the ratio of the intensities of two different radiation wavelengths emitted by a body is a function of its temperature. This gives the true temperature if it is an ideal black or gray body.

Chapter 3

Heat flow modelling

Heat flow modelling is a highly complex and difficult physical phenomena to model. There has been intense research on this subject for the past decades in order to get better performance and quality in welding. This may include the welds ability to withstand mechanical stress and corrosion. The heat flow equations are governed by partial nonlinear differential equations. This means that analytical solutions of the equations may be difficult, and even impossible, to obtain without assumptions, simplifications and loss of generality. The most important characteristics in welding are the fact that peak temperatures are very high, temperature gradients are high and temperature fluctuates rapidly. This means that in order to capture the speed and complexity of the temperature distribution in a welding specimen, the model needs to have a high order of accuracy. On the other hand, high accuracy often leads to high order of complexity, which may lead to a model difficult to control. In this chapter, a mathematical model capturing the wanted characteristics of the problem posed will be abbreviated.

3.1 The general heat flow equation

The governing equation used here neglects the effects of heat losses due to radiation and convection as described in (Nguyen 2004). The general equation is

$$\left[\frac{\partial^2 T}{\partial x^2} + \frac{\partial^2 T}{\partial y^2} + \frac{\partial^2 T}{\partial z^2} \right] = \frac{1}{a} \frac{\partial T}{\partial t} + f(x, y, z, t), \quad (3.1)$$

where a is thermal diffusivity of the body material ($a = k/\rho c$), where k is thermal conductivity, ρ is density and c is specific heat of the material. There are five boundary conditions to this general case:

1. Prescribed surface temperature: $T(x, y, z, t) = f(x, y, z, t)$.
2. Prescribed heat input: $k\partial T(x, y, z, t)/\partial n = g(x, y, z, t)$,
where n is normal to the surface.
3. Perfectly insulated surface: $\partial T(x, y, z, t)/\partial n = 0$.

4. Convection at the surface: $k\partial T(x, y, z, t)/\partial n = h [T_0 - T(x, y, z, t)]$,
where h is film coefficient of surface conductance.

5. Two-solid bodies in contact: $T_1(x, y, z, t) = T_2(x, y, z, t)$ and
 $k_1\partial T(x, y, z, t)/\partial n = k_2\partial T(x, y, z, t)/\partial n$

where T_1 and T_2 are temperatures at the contact surface, and k_1 and k_2 are the corresponding thermal conductivities of the two contact bodies.

In welding, the heat sources may be modelled in such a manner that the effect of radiation and convection are negligible in comparison to the effect of conduction. This means that boundary term number 4 and 5 will be neglected in the analysis. This assumption gives the fact that one regard the welded material as a solid. In reality, the welded metal will go through phase changes and thus be liquefied for a certain period of time. This is crucial in real life in order to get a homogeneous material after welding is finished.

3.2 Heat input and arc efficiency factor

The heat-input Q is one of the parameters that effects the temperature the most. This can be interpreted as the net heat input or energy applied. In general the heat input is defined as follows:

$$Q = \left(\frac{U \cdot I \cdot 60}{\nu \cdot 1000} \right) \eta, \quad (3.2)$$

where Q is the heat input [kJ/mm], U is the voltage [V], I is the electric current [A], ν is the welding speed [mm/min] and η is the arc efficiency factor.

The arc efficiency factor is the factor describing the heat losses due to convection and radiation. It is defined as follows:

$$\eta = \frac{q_0}{IU}, \quad (3.3)$$

where q_0 is the net power received by the weldment, and U and I are as described above. The typical η is in the range of 66 – 85% for G-FCAW.

3.3 The thick plate solution

As the model in this paper will be made with the help from numerical tools, it is important to have a comparison reference related to the numerical model. *Rosenthal's Thick Plate solution* is used as a reference throughout the modelling. This is because it represents a good approximation of the posed problem. It is a special result from *the general thick plate solution* developed by Ryaklin. The deduction of this solution is taken from (Grong 1994). The assumptions made here, are as follows:

The specimen welded on is a semi-infinite body which is isotropic and has an initial temperature T_0 limited in one direction by a plane that is impermeable to heat. At initial time, a point source of constant power q_0 moves with constant speed (ν) in the positive x -direction starting in the origin. The wanted information is the rise of temperature $T - T_0$ in a point P at time t as seen in Fig. (3.1).

Over a small time step dt' , the amount of heat released at the surface is $dQ = q_0 dt'$. According to the equation for *point source on heavy slab* the rise of temperature will be as follows:

$$\begin{aligned} dT &= \frac{2q_0 dt'}{\rho c [4\pi a(t-t')]^{3/2}} \exp\left[-\frac{(R')^2}{4a(t-t')}\right] \\ &= \frac{-2q_0 dt''}{\rho c [4\pi a(t'')]^{3/2}} \exp\left[-\frac{(R'')^2}{4a(t'')}\right], \end{aligned} \quad (3.4)$$

where $t'' = t - t'$ is the time available for conduction over the distance $R' = \sqrt{(x_0 - \nu t')^2 + y_0^2 + z_0^2}$ to point P . As this is a representation of the pseudo steady state solution, the position P must be represented in reference to the moving heat source. This is done through the shifting of the coordinate system as seen in Fig. (3.1).

$$\begin{aligned} y &= y_0, \quad z = z_0, \quad x = x_0 + \nu t \\ \text{and} \\ x_0 + \nu t' &= x + \nu t - \nu t' = x + \nu t''. \end{aligned} \quad (3.5)$$

By inserting this into (3.4) the following expression appears:

$$dT = \frac{-2q_0 dt''}{\rho c [4\pi a(t'')]^{3/2}} \exp\left[-\frac{\nu x}{2a} - \frac{(R)^2}{4a(t'')} - \frac{\nu^2 t''}{4a}\right], \quad (3.6)$$

where $R = \sqrt{x^2 + y^2 + z^2}$. By substituting the following into (3.6) the total rise of temperature at P is obtained:

$$\begin{aligned} u^2 &= \frac{R^2}{4at''}, \quad dt'' = -\left(\frac{R^2}{2au^3}\right) du \\ \text{and} \\ m &= \frac{\nu R}{4a}, \quad \frac{m^2}{u^2} = \frac{\nu^2 t''}{4a}. \end{aligned} \quad (3.7)$$

By integrating between the limits $u = R^2/4at$ and $u = \infty$, this gives the following integral:

$$T - T_0 = \frac{q_0}{2\pi\lambda R} \left(\frac{2}{\sqrt{\pi}}\right) \exp\left(\frac{-\nu x}{2a}\right) \int_u^\infty \exp\left(-u^2 - \frac{m^2}{u^2}\right) du. \quad (3.8)$$

The following identity is known:

$$\int_0^\infty \exp\left(-u^2 - \frac{m^2}{u^2}\right) du = \frac{\sqrt{\pi}}{2} \exp\left(-\frac{\nu R}{2a}\right).$$

The general thick plate solution may then be written as:

$$T - T_0 = \frac{q_0}{2\pi\lambda} \left(\frac{1}{R}\right) \exp\left(\frac{-\nu x}{2a}\right) \left[\exp\left(\frac{-\nu R}{2a}\right) - \frac{2}{\sqrt{\pi}} \int_0^u \exp\left(-u^2 - \frac{m^2}{u^2}\right) du \right]. \quad (3.9)$$

The integral will tend to zero when u is sufficiently small. This means that welding has been performed over a sufficient period of time, giving the pseudo-steady state temperature distribution known as *Rosenthals Thick Plate solution*.

$$T - T_0 = \frac{q_0}{2\pi\lambda} \left(\frac{1}{R} \right) \exp \left[-\frac{\nu}{2a}(R + x) \right]. \quad (3.10)$$

For further analysis, the equation above is transformed into dimensionless parameters. According to (Grong 1994), this is done with the following definitions of parameters:

- Dimensionless temperature:

$$\theta = \frac{T - T_0}{T_c - T_0}, \quad (3.11)$$

where T_c is the chosen reference temperature.

- Dimensionless operating parameter:

$$n_3 = \frac{q_0\nu}{4\pi a^2 \rho c (T_c - T_0)} = \frac{q_0\nu}{4\pi a^2 (H_c - H_0)} \quad (3.12)$$

- Dimensionless x-coordinate:

$$\xi = \frac{\nu x}{2a} \quad (3.13)$$

- Dimensionless y-coordinate:

$$\psi = \frac{\nu y}{2a} \quad (3.14)$$

- Dimensionless z-coordinate:

$$\zeta = \frac{\nu z}{2a} \quad (3.15)$$

- Dimensionless radius vector:

$$\sigma_3 = \frac{\nu R}{2a} \quad (3.16)$$

- Dimensionless time:

$$\tau = \frac{\nu^2 t}{2a} \quad (3.17)$$

The dimensionless form of 3.10 is obtained by inserting the above defined parameters:

$$\frac{\theta}{n_3} = \left(\frac{1}{\sigma_3} \right) \exp(-\sigma_3 - \xi). \quad (3.18)$$

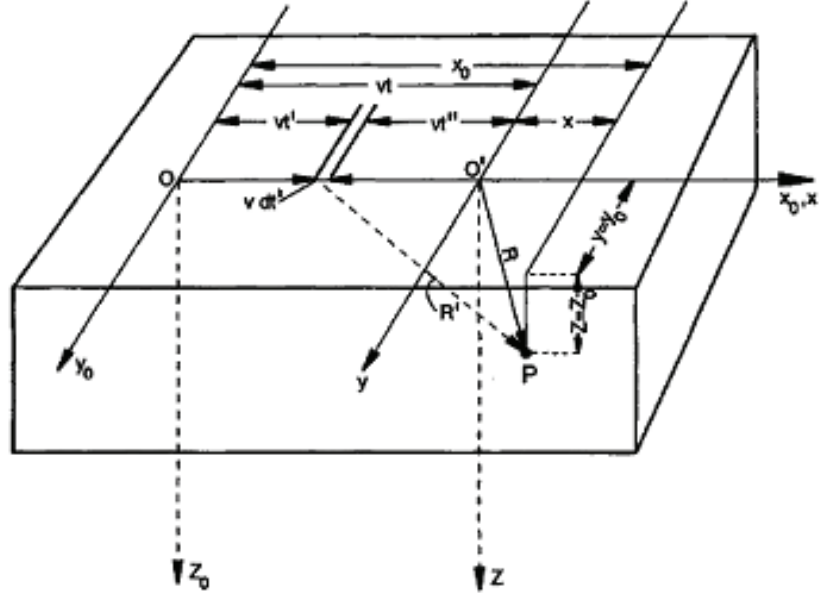


Figure 3.1: Moving point source on a semi-infinite slab.

3.4 Temperature decay rate

A crucial factor in determining the quality and strength of the weld, is the rate at which cooling takes place. There is a widely accepted fact that the austenite to ferrite transformation (Grong 1994) takes place between 800 and 500 °C. From the definition of (3.18) the decay rate on the weld centre-line behind the source gives $\psi = \zeta = 0$ and $\sigma_3 = -\xi = \tau$. This deduces the following expression:

$$\frac{\theta}{n_3} = \frac{1}{\tau}. \quad (3.19)$$

Which leads to the difference:

$$\Delta\tau_{8/5} = n_3 \left(\frac{1}{\theta_{500}} - \frac{1}{\theta_{800}} \right). \quad (3.20)$$

Computing the relation by inserting the dimensionless variables and using the same reference temperature T_c gives the relation

$$\Delta t_{8/5} = \frac{q_0}{2\pi a \rho c v} \left(\frac{1}{500 - T_0} - \frac{1}{800 - T_0} \right), \quad (3.21)$$

which is a measure of the time the austenite to ferrite transformation takes. (3.21) will be used throughout the analysis in order to validate the results obtained from the numerical model.

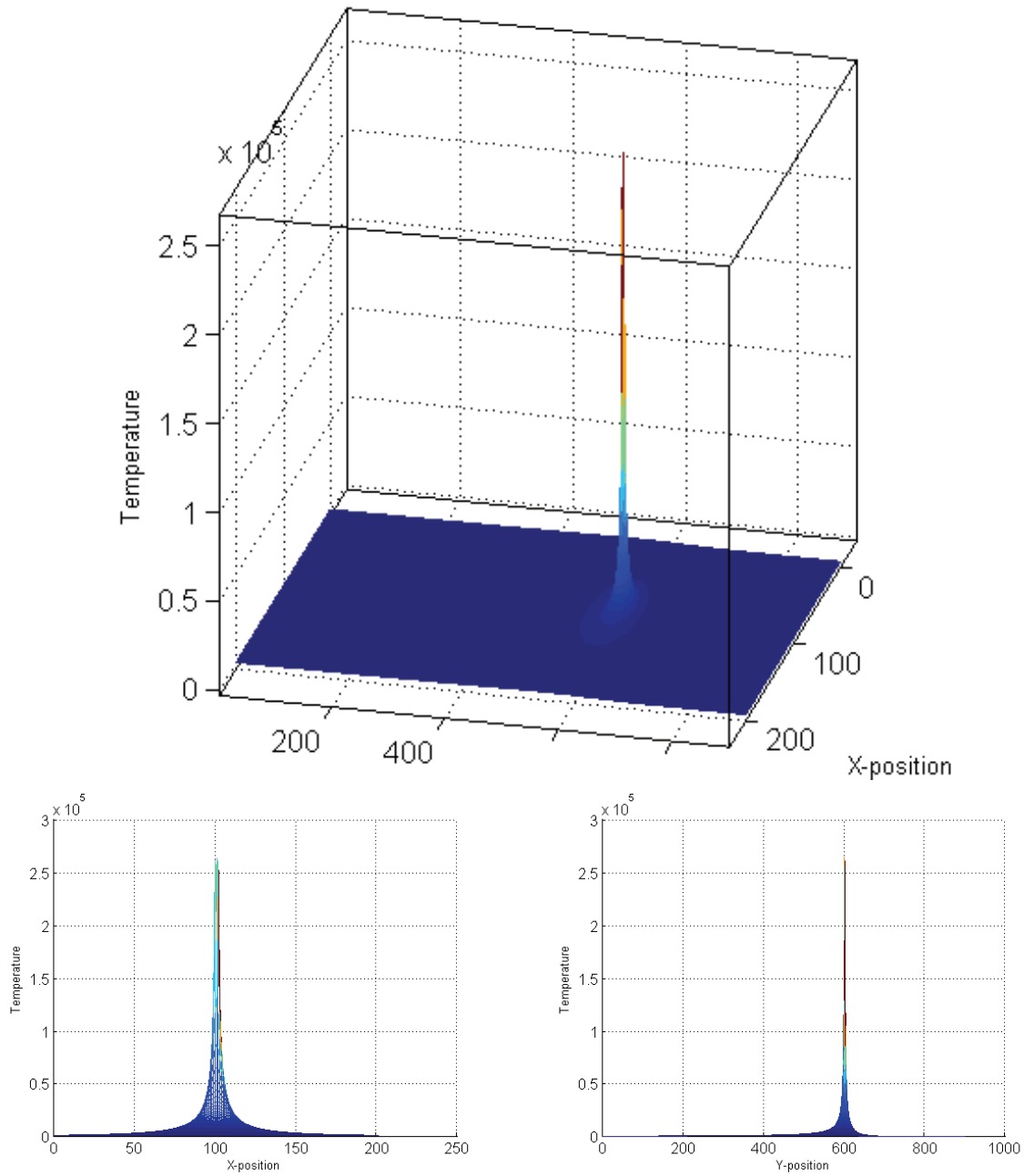


Figure 3.2: Plot of the temperature distribution in a plate according to Rosenthal's thick plate solution. This plot is made with $I = 200A$, $U = 23V$ and $\nu = 5mm/min$.

Chapter 4

The finite element method

Modelling of physical phenomena may be done in several ways. For a long time, the governing method of analysis has been the analytical one, where a mathematical model is derived from the governing set of equations. This is a very powerful method of analysis, but has its drawback in the way it handles large problems with advanced dynamics. In recent decades the increase in computer power has changed this to a large extent. It is now possible to simulate and solve large sets of equations through numerical modelling. There has been developed many ways of modelling in the numerical manner. One of the most used, and certainly one of the most powerful ones, is the Finite Element Method (FEM). On the FEM one may apply partial differential equations (PDE's) on complicated geometries with boundary conditions. This makes it immensely versatile and flexible.

The basic idea behind the FEM is to divide a continuous domain into smaller discrete domains as seen in Fig. 4.1. The governing equations are then applied to each sub domain. It is easier to represent a complicated function as a collection of polynomials. The theory from this chapter is gathered from (Reddy 2006) and (Com 2005).

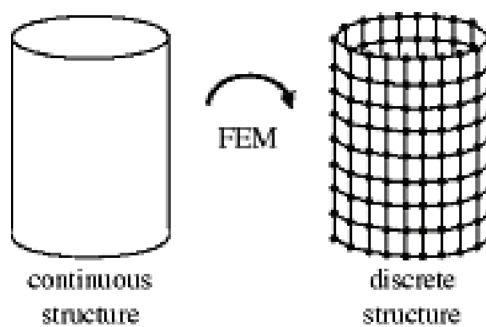


Figure 4.1: Transforming a domain from a continuous structure to a discrete structure using FEM.

4.1 The basic features of the method

The method is characterized by three basic features which makes it superior to other numerical methods:

- A geometrical domain is represented as a collection of smaller sub domains with simple geometrical shape called *finite elements*, as seen in Fig. 4.1. Each element is seen as an independent domain by itself.
- The governing equations of the problem are applied to develop algebraic expressions over each single sub domain.
- The independent domains are, with a governing equation, put back together to their respective position using certain inter element relationships.

The whole method includes three stages, and they are all based on numerical modelling, and will thus be an approximation of the real physical phenomena. This introduces errors in all the three stages of the modelling. In the sub domain division into finite elements there may be elements which make the assembled sub domains not fitting the original domain. The unknowns u in the element-equation derivation are approximations using the basic idea that a continuous function can be a linear combination of known functions ϕ_i and undetermined coefficients c_i , making $u \approx \sum c_i \phi_i$. The relation between the unknowns c_i are determined satisfying the governing equations in a weighted integral sense. ϕ_i are polynomials often determined through interpolation theory. This introduces errors both in representing u and evaluating the integrals. Last of all, errors are introduced in solving the assembled system of equations.

Some of the above discussed errors may be zero. If all errors are zero, the solution is exact. This is in most cases not the fact. The magnitude of the errors will decrease as the resolution of the grid introduced increases. Through the rise in computer-power, the possibility of increased accuracy has risen immensely the last couple of decades. For more thorough explanations on the basic theory behind the FEM, look in chapter 1 of (Reddy 2006).

4.2 The weighted integral and weak form formulations

In classical terms the variational principle is a way of creating a set of equations equivalent to the governing equations of the problem. The modern way of defining the variational principle is to transform the governing equations into weighted integral-statements. The weighted integral may be used to express almost all physical principles.

4.2.1 The weighted integral statement

The solution of differential and/or integral equations is almost always, when using approximate methods, in the form:

$$u(\mathbf{x}) \approx U_N(\mathbf{x}) = \sum_{j=1}^N c_j \phi_j(\mathbf{x}), \quad (4.1)$$

where u represents the exact solution of the particular equation and associated boundary conditions, and U_N is its approximation. The approximate U_N is represented as a linear combination of unknown parameters c_j and known functions ϕ_j of position \mathbf{x} on domain Ω , where the problem is posed. To obtain the approximate solution, one needs to find N algebraic relations among the N parameters c_1, c_2, \dots, c_N . The sum of all these coefficients give the approximate solution of U_N . If one can find a U_N that satisfies the governing differential equation in every point \mathbf{x} on the domain Ω , and satisfying boundary conditions, then the solution is exact.

When trying to find an exact solution on the form of (4.1), working from known polynomials ϕ_j , the exact solution satisfying the boundary conditions may give *no solution* to the equations because of inconsistency in the statement of the equations. In order to bypass this problem, the weighted integral has some preferable features.

$$\int_0^1 w(x)R dx = 0, \quad (4.2)$$

where $w(x)$ is called a *weight function* and R denotes the differential equation called the *residual*. This is defined as,

$$R \equiv -\frac{dU_N}{dx} - x\frac{d^2U_N}{dx^2} + U_N.$$

From (4.2), we obtain as many linearly independent equations as there are linearly independent functions of $w(x)$.

The advantage is that with the integral (4.2) stated as it is, one gets all higher order terms cancelled out because of the limits set, and does not get inconsistency in determining the unknown coefficients as one gets in the original case. In addition, the number of choices of w must be restricted to N , so that there is the same number of equations as there are unknown coefficients c_j . For more info look in chapter 2.1. of (Reddy 2006).

4.2.2 The weak form

As the FEM is a method of determining approximate solutions of larger systems, the boundary conditions of the problem are also crucial to be fulfilled. *The weak form* facilitates these problems in an elegant way. It classifies the boundary conditions into natural and essential types. It is defined to be a weighted-integral statement of a differential equation in which the differentiation is transferred from the dependent variable to the weight function such that all natural boundary conditions of the problem are included in the integral statement.

As an example of deriving and explaining the weak form formulation, the following one-dimensional differential equation is formulated:

$$-\frac{d}{dx} \left[a(x) \frac{du}{dx} \right] = f(x) \quad \text{for} \quad 0 < x < L, \quad (4.3)$$

for $u(x)$, subject to the boundary conditions:

$$u(0) = u_0, \quad \left(a \frac{du}{dx} \right) \Big|_{x=L} = Q_L. \quad (4.4)$$

Here $a(x)$ and $f(x)$ are known functions of x , and u_0 and Q_L are known values. L is the size of the one-dimensional domain. The boundary conditions are said to be non-homogeneous when the specified values are nonzero, and homogeneous when they are zero.

After the problem is stated, one seeks an approximation of $u(x)$ in the form:

$$u(x) \approx U_N(x) = \sum_{j=1}^N c_j \phi_j(x) + \phi_0(x), \quad (4.5)$$

and then determine c_j such that $U_N(x)$ satisfies the differential equation 4.3. Inserting the approximation into 4.3 gives:

$$-\frac{d}{dx} \left[a(x) \frac{dU_N}{dx} \right] = f(x) \quad \text{for} \quad 0 < x < L. \quad (4.6)$$

As U_N is an approximation of the real function, the equality does not necessarily hold, and a *residual* approximation of the differential equation is defined:

$$R(x, c_j) \equiv -\frac{d}{dx} \left[a(x) \frac{dU_N}{dx} \right] - f(x) \neq 0 \quad \text{for} \quad 0 < x < L. \quad (4.7)$$

The residual approximation may be solved in a weighted integral sense in order to get $R = 0$, because of the fact that it can't be exactly zero. There are several different methods developed, where the form of the weight function w_i is chosen. There exists four primary methods determining the form of w_i :

$$\begin{aligned} \text{Petrov-Galerkin method:} & \quad w_i = \psi_i \neq \phi_i \\ \text{Galerkin's method:} & \quad w_i = \phi_i \\ \text{Least squares method:} & \quad w_i = \frac{d}{dx} \left(a(x) \frac{d\phi_i}{dx} \right) \\ \text{Collocation method:} & \quad w_i = \delta(x - x_i), \end{aligned} \quad (4.8)$$

where δ is the dirac's delta. The methods will give different results, and thus have their different area of application. With the origin in the differential equation stated above with the governing boundary conditions, the weak form is developed in three steps.

Step 1. (The Weighted Integral statement.) One moves the terms of (4.3) over to one side so that it equals zero, multiply with a function $w(x)$, and integrate over the entire domain $\Omega \in (0, L)$:

$$0 = \int_0^L w \left[-\frac{d}{dx} \left(a \frac{du}{dx} \right) - f \right] dx. \quad (4.9)$$

Since the expression in the brackets in the above integral is nonzero, it is made zero in the weighted integral sense. The integral statement allows the freedom to choose N linearly independent functions for w and obtain N equations for c_1, c_2, \dots, c_N of (4.5).

At this point the boundary conditions of the problem is not included. Since the weight-function can be any non-zero integrable function, and has no differentiability requirements, it may be exploited.

Step 2. When developing the weak term, one makes some changes in comparison to when solving the conventional weighted integral. The weighted integral statement demands that U_N (see (4.5)) is differentiable as many times as called for in the original differential equation(see (4.3)), and satisfy the specified boundary conditions.

When the approximate functions ϕ_j are such that U_N is not continuously differentiable, as in many cases, one makes use of ϕ_j for $w \sim w_i$. It will then make sense to shift half of the derivatives from u to w so that both are equally differentiated, and thus there will be fewer or weaker continuity requirements on ϕ_j . This is known as the weak formulation, and has two desirable characteristics. The dependent variable requires a weaker continuity, and always result in a symmetric coefficient matrix for self-adjoint equations. The other characteristic is that the natural boundary conditions are included in the weak form, and U_N is only required to satisfy the essential boundary conditions of the problem.

The *primary variable* of the problem in this case is the dependent variable u expressed in the same form as the weight function (w) appearing at the boundary. By performing the integral of (4.9), and introducing the variables, the equation becomes:

$$Q \equiv \left(a \frac{du}{dx} \right) n_x, \quad (4.10)$$

Q represents the heat, and is called a *secondary variable*, n_x is the direction cosine, which is simply the angle between positive x -axis and the normal to the boundary. We then get the following result:

$$\begin{aligned} 0 &= \int_0^L \left(a \frac{dw}{dx} \frac{du}{dx} - wf \right) dx - \left[wa \frac{du}{dx} \right]_0^L \\ &= \int_0^L \left(a \frac{dw}{dx} \frac{du}{dx} - wf \right) dx - (wQ)_0 - (wQ)_L, \end{aligned} \quad (4.11)$$

and $n_x = \pm 1$ respectively. (4.11) is called the *weak form* of (4.3). The reason for the term *weak* is its reduced demand for continuity of u . In (4.9) u had to be twice differentiable, as in (4.11) it is only demanded once differentiable.

Step 3. The last step of the weak formulation is to impose the actual boundary conditions under consideration. One demands that the weight function w vanish at the specific boundary points. In other words, w has to satisfy the homogeneous form of the specified essential boundary conditions. To clarify, look at the above defined problem with boundary conditions (4.4). The essential boundary condition is $u = u_0$ and $(adu/dx)|_{x=L} = Q_L$ is the natural condition. Then (4.11) reduces to:

$$0 = \int_0^L \left(a \frac{dw}{dx} \frac{du}{dx} - wf \right) dx - w(L)Q_L, \quad (4.12)$$

because the weight function $w(0) = 0$, and

$$Q(L) = \left(a \frac{du}{dx} n_x \right) \Big|_{x=L} = \left(a \frac{du}{dx} \right) \Big|_{x=L} = Q_L. \quad (4.13)$$

(4.12) is the weak form equivalent to the original (4.3) and natural boundary condition (4.4).

4.2.3 Summary

To summarize, the weak form of a differential equation is a weighted integral statement which is the equivalent to the differential equation and its specified natural boundary conditions. It is possible to specify a weak form for all differential equation problems, linear or non-linear. There are three basic steps in the development of the weak form. All expressions are set equal to zero, then the entire equation is multiplied with a weight function w . The resultant statement is then integrated over the entire domain, and the resulting statement is called the weighted-integral form. One then integrate by parts in order to distribute the differentiations between the dependent variable and the weight-function. The boundary terms are used to identify the form of the primary and secondary variables. At last, the boundary terms are modified by restricting the weight function to satisfy the homogeneous form of the specified essential boundary conditions and replacing the secondary variables by their specified values.

The whole purpose of the weak form and/or the weighted integral statement is to obtain as many algebraic equations as there are unknowns in the approximation of the dependent variables of the equation.

Chapter 5

Model order reduction

When modelling phenomena which have a complex nature, the order of the equations describing the problem may reach very high order of complexities. This results in many states in the state-space making it infeasible to use in controller design. In order to bypass this problem, model order reduction is a powerful tool, which goal is to systematically develop a low-order model that catches the relevant system dynamics over an adequate range of frequencies and forcing inputs. There exists many different techniques for reducing the order of the model. They all have different advantages and prerequisites. Common for most of them, is that the resulting reduced model does not represent anything physical anymore. The states can not be associated with the physics in the original model. It may be seen as a black box, where the inputs and outputs of the model are the only known parameters related to the original physics. In this project, the model is linear but has a very large number of states. With this in mind, many of the methods existing will not be investigated, and throughout this chapter the emphasis will be put on the following four methods:

- Proper Orthogonal Decomposition(POD)
- Rational Krylov algorithms
- Fourier model reduction
- Balanced realization and truncation

POD will be used as the reduction technique in the consecutive work, whereas the three last methods mentioned are meant as an introductory study. The chapter is a literature study on model order reduction, and the methods described here are found in the following articles: (Willcox & Megretski 2005), (Gugercin et al. 2004), (Olsson 2002), (Gugercin & Wilcox 2007), (Hovland & Gravdahl 2006), (Camp & King 1997), (Astrid 2004) and (Cazemier 1997)

5.1 Problem statement

The main task of the model reduction in general is to find a low order state space model

$$\begin{aligned}\hat{G} : \hat{E} \frac{d}{dt} \hat{x}(t) &= \hat{A} \hat{x}(t) + \hat{B} u(t) \\ \hat{y}(t) &= \hat{C} \hat{x}(t),\end{aligned}\tag{5.1}$$

which approximates the original stable model

$$\begin{aligned}G : E \frac{d}{dt} x(t) &= Ax(t) + Bu(t) \\ y(t) &= Cx(t).\end{aligned}\tag{5.2}$$

$x(t) \in \mathfrak{R}^n$ is the state-vector containing the n unknowns. $\hat{x}(t) \in \mathfrak{R}^k$ is the k^{th} -order reduced representation of the state-vector. $u(t) \in \mathfrak{R}$ is the system input. For simplicity in further analysis, a single-input/single-output (SISO) system is considered which is regarded as stable and linear time-invariant (LTI). Input to the system is $u(t)$ and the output is contained in the vector $y(t)$. The quality of the reduced order model \hat{G} is defined as the H-infinity norm of the difference between the transfer functions:

$$\left\| \hat{G} - G \right\|_{\infty} = \sup_{\omega \in \mathfrak{R}} \left| \hat{G}(j\omega) - G(j\omega) \right|.\tag{5.3}$$

It does not exist an exact solution of (5.3), and thus making the present algorithms sub-optimal with respect to the constraints imposed on stability and order of \hat{G} .

5.2 Proper orthogonal decomposition

POD is a widely used model reduction method, and it is especially well qualified for large scale systems. It was first introduced by (Loève 1946) and (Karhunen 1946), and is also referred to as the Karhunen-Loève expansion. It is computationally expensive in general, so in order to apply it to a 3D domain, the only successful POD variant used with success before is the "snapshot" method, which will be considered here. This means that at distinct points in time t^i , a solution-vector x^i is taken out and saved. Stacking all the x^i vectors together forms the snapshot-matrix,

$$\chi = [x^1, x^2, \dots, x^M] = [x(t_1), x(t_2), \dots, x(t_M)].\tag{5.4}$$

For further developing the reduced space model, the correlation matrix R is formed as

$$R_{ik} = \frac{1}{M} (x^i, x^k),\tag{5.5}$$

where M is the number of solutions captured and (x^i, x^k) is the inner product between x^i and x^k . The next step is to compute the eigenvalues λ_i and the belonging eigenvectors ψ^i

of R . These are used to form the POD basis vectors, and are given as a linear combination of snapshots. The j^{th} POD basis vector, Φ_j , is given as

$$\Phi_j = \sum_{i=1}^M \psi_i^j x^i, \quad (5.6)$$

where ψ_i^j denotes the i^{th} element of the j^{th} eigenvector. The magnitude of the eigenvalues describes the relative importance of the corresponding POD-basis vector. Identifying and choosing a sufficient amount of basis-vectors N , mirroring the sufficient amount of energy from the snapshot matrix, gives the total projection-matrix $\Phi = \sum_{j=1}^N \Phi_j$. The reduced space matrices described in (5.1) are obtained as follows,

$$\begin{aligned} \hat{E} &= \Phi^T E \Phi && \in \mathfrak{R}^{k \times k}, \\ \hat{A} &= \Phi^T A \Phi && \in \mathfrak{R}^{k \times k}, \\ \hat{B} &= \Phi^T B && \in \mathfrak{R}^{k \times 1}, \\ \hat{C} &= C \Phi && \in \mathfrak{R}^{1 \times k}. \end{aligned} \quad (5.7)$$

When the computation of the orthonormal set of POD vectors is done, the reduced order model is obtained by projecting the solution of the original system onto the reduced-space basis

$$x(t) = \sum_{i=1}^M \hat{x}_i(t) \Phi_i. \quad (5.8)$$

Substituting this into (5.2) and using orthogonality, the reduced order system (5.1) is obtained. Normally the snapshots are taken from simulations of the original system. A problem is that the reduced order model will only mirror dynamics from the snapshots taken. This means that inputs to the simulations has to be chosen with great care. This may lead to problems in many applications. Snapshots may not always be accessible directly from a process. This may have several reasons. It is possible to bypass this problem by applying the POD in the frequency domain, but the frequency domain approach has an extensive computational cost and will not be regarded here. Other characteristics of POD, is that it does not guarantee the quality and stability of reduced order models, even though the original system itself is stable. This gives rise to the need for tuning in applications reduced with POD. POD is not an exact science. The heuristic criterion

$$P = \frac{\sum_{i=1}^k \sigma_i^2}{\sum_{i=1}^M \sigma_i^2}, \quad (5.9)$$

may be used as an indication of the amount of energy conserved in the model reduced order model. The number of basis functions k denotes the number of states in the reduced order model. If $P \approx 1$, then almost all the energy is captured in the system.

5.3 Rational Krylov algorithms

When working with Krylov based methods, one takes origin in the systems transfer function

$$G(s) = C(sI - A)^{-1}B. \quad (5.10)$$

The reduced order transfer function $\hat{G}(s)$ is obtained through interpolation with $G(s)$ and some of its derivatives (called moments) at some points σ_k in the complex plane. Mathematically speaking, this means that one wants to find the matrices \hat{A} , \hat{B} and \hat{C} so that

$$\left. \frac{(-1)^j}{j!} \frac{d^j G(s)}{ds^j} \right|_{s=\sigma_k} = C(\sigma_k I - A)^{-(j+1)} B = \hat{C}(\sigma_k I - \hat{A})^{-(j+1)} \hat{B} = \left. \frac{(-1)^j}{j!} \frac{d^j \hat{G}(s)}{ds^j} \right|_{s=\sigma_k}, \quad (5.11)$$

where $k = 1, \dots, K$ and $j = 1, \dots, J$. K is the number of interpolation points σ_k and J is the number of moments to be matched at each interpolation point. When interpolating, it is desired to match the moments at several frequencies spanning the operation-frequency range of the system. This is done due to the fact that if one only matches the moment at one frequency, it will often lead to a very large error at other frequencies. However, it is very expensive to compute each single interpolation-point explicitly, and the rational Krylov method amongst others, is capable of computing $\hat{G}(s)$ without computing them explicitly. This is very important because of the fact that it is a very time-consuming operation to perform, and thus one of the main motivations behind the rational Krylov based methods. A Krylov space is defined as

$$\begin{aligned} K_j(F, g; \sigma) &:= \text{Im} \left([g \quad Fg \quad F^2g \quad \dots \quad F^{j-1}g] \right) \quad \text{if } \sigma = \infty, \\ K_j(F, g; \sigma) &:= \text{Im} \left([(\sigma I - F)^{-1}g \quad \dots \quad (\sigma I - F)^{-j}g] \right) \quad \text{if } \sigma \neq \infty, \end{aligned} \quad (5.12)$$

where matrix $F \in \mathbb{C}^{n \times n}$, vector $g \in \mathbb{C}^n$ and point $\sigma \in \mathbb{C}$ are the constructs of the Krylov space defined for index j .

When creating the reduced Krylov space, one needs to create the following two matrices:

$$\begin{aligned} \text{Range}(V) &= \text{Span} [K_{j_1}(A, B; \sigma_1), \quad \dots, \quad K_{j_K}(A, B; \sigma_K)] \\ \text{Range}(Z) &= \text{Span} [K_{j_{K+1}}(A^T, C^T; \sigma_{K+1}), \quad \dots, \quad K_{j_{2K}}(A, B; \sigma_{2K})], \end{aligned} \quad (5.13)$$

which then gives the property $Z^T V = I$. This gives the reduced order model $\hat{G}(s) = CV(sI - Z^T AV)^{-1} Z^T B$ matching j_k number of moments of $G(s)$ at each consecutive interpolation point σ_k . So to construct the reduced order model, all one has to do is to construct matrices V and Z as described above. This makes the method computationally efficient because it can be implemented iteratively due to the fact that one only require some matrix-vector multiplications and some sparse linear solvers.

5.4 Fourier model reduction

This method for performing model reduction is similar to that of Krylov, but is done in the discrete frequency domain. This means that one needs to put the transfer function over into discrete form. This is done by inserting the identity

$$z = \frac{s + \omega_0}{s - \omega_0}, \quad (5.14)$$

into

$$G(s) = g(z) = c(zI - a)^{-1}b, \quad (5.15)$$

and

$$\begin{aligned}
d &= C(\omega_0 I - A)^{-1} B, \\
a &= -(\omega_0 I + A)(\omega_0 I - A)^{-1}, \\
c &= 2\omega_0 C(\omega_0 I - A)^{-1}, \\
b &= -I(\omega_0 I - A)^{-1} B,
\end{aligned} \tag{5.16}$$

and ω_0 is some fixed positive real number. To complete the discrete time transform of $G(s)$ the following fourier decomposition is used

$$G(s) = \sum_{j=0}^{\infty} G_j \left(\frac{s - \omega_0}{s + \omega_0} \right)^j, \tag{5.17}$$

where

$$G_0 = d, \quad G_j = ca^{j-1}b \quad (j = 1, 2, \dots). \tag{5.18}$$

The fourier expansion just performed converges exponentially for $|z| > \rho(a)$ where $\rho(a)$ denotes the spectral radius of a , which is the maximal absolute value of a 's eigenvalues. The first m coefficients are calculated using the computationally cheap iterative process

$$G_j = ch_{j-1}, \quad h_j = ah_{j-1} \quad (j = 1, \dots, m), \tag{5.19}$$

where $h_0 = b$. It is expected to be stable because $\rho(a) < 1$.

For further development, the $m + 1$ fourier coefficients are used to construct a m^{th} order state-space model

$$\hat{g} : \quad \hat{x}[t + 1] = \hat{a}\hat{x}[t] + \hat{b}u[t], \quad \hat{y}[t] = \hat{c}\hat{x}[t], \tag{5.20}$$

where

$$\hat{a} = \begin{bmatrix} 0 & 0 & 0 & 0 & \dots \\ 1 & 0 & 0 & 0 & \dots \\ 0 & 1 & 0 & 0 & \dots \\ 0 & 0 & 1 & 0 & \dots \\ 0 & 0 & 0 & \ddots & \dots \end{bmatrix}, \quad \hat{b} = \begin{bmatrix} 1 \\ 0 \\ 0 \\ \vdots \end{bmatrix}, \quad \hat{c} = [g_1 \quad g_2 \quad \dots \quad g_m], \tag{5.21}$$

consists of up to several hundred states. It is possible to further reduce this by applying balanced truncation, which will be described in the next section. For use in balanced truncation, the controllability matrix is the identity matrix and the observability matrix is the Hankel matrix with \hat{c} as the first row. By computing the singular vectors from the m^{th} order Hankel matrix

$$\Gamma = \begin{bmatrix} g_1 & g_2 & g_3 & \dots & g_{m-1} & g_m \\ g_2 & g_3 & g_4 & \dots & g_m & 0 \\ g_3 & g_4 & g_5 & \dots & 0 & 0 \\ \vdots & \vdots & \vdots & & \vdots & \vdots \\ g_{m-1} & g_m & 0 & \dots & 0 & 0 \\ g_m & 0 & 0 & \dots & 0 & 0 \end{bmatrix}, \tag{5.22}$$

the balancing vectors can be obtained. The Hankel singular values are given by the singular values of Γ and is denoted as σ_i , $i = 1, 2, \dots, m$. Finally, the low-order model can be obtained using the following relationships

$$\hat{A} = \omega_0(\hat{a} - I)^{-1}(\hat{a} + I), \quad (5.23)$$

$$\hat{B} = 2\omega_0(\hat{a} - I)^{-1}\hat{b}, \quad (5.24)$$

$$\hat{C} = -\hat{c}(\hat{a} - I)^{-1}, \quad (5.25)$$

$$(5.26)$$

which completes the reduction through fourier techniques.

5.5 Balanced realization and truncation

The procedure called balanced truncation is a method based on finding and eliminating states that are difficult to control or to observe in the state space realization (5.2) and obtaining the reduced order model (5.1). The procedure is time-consuming and will not be applicable for very large scale systems due to need of large amounts of computer power.

To identify controllable and observable states, the controllability grammian

$$L_B = \int_0^{\infty} e^{At} B B^T e^{A^T t} dt, \quad (5.27)$$

and the observability grammian

$$L_C = \int_0^{\infty} e^{A^T t} C C^T e^{At} dt, \quad (5.28)$$

are defined. The reachable states are denoted by L_C and the observable ones by L_B . Both grammians are realization dependent, meaning that two different state-space systems which give the same transfer function, may have different grammians. A realization may have few controllable states but many observable states and vice versa. This problem is called balanced realization. Here states that are difficult to control coincide with states that are difficult to observe, and are realized as

$$L_B = L_C = \text{diag}(\sigma_1, \sigma_2, \dots, \sigma_n, \dots), \quad \sigma_1 \geq \sigma_2 \geq \dots \geq 0, \quad (5.29)$$

where $\sigma_i = \sqrt{\lambda_i(L_B L_C)}$ are the Hankel singular values and realization invariant. The balancing transformation T can be found from the following algorithm:

- Compute L_B and L_C from (5.2) which will be defined as Σ in the following.
- Following the fact that L_B is symmetric and positive definite, the Cholesky decomposition gives $L_B = R^T R$.
- Compute $R^T L_C R = U \Sigma^2 U^T$ where $\Sigma^2 = \text{diag}(\sigma_i)_{i=1}^{\infty}$ and U is unitary.
- Defining $T = \Sigma^{\frac{1}{2}} U^T R$, where it follows that $(T^{-1})^T L_C T^{-1} = \Sigma = T L_B T^T$.

T then gives rise to the balanced state space realization denoted as

$$\sum (A_{bal}, B_{bal}, C_{bal}) = \sum (T A T^{-1}, T B, C T^{-1}). \quad (5.30)$$

This concludes the balanced realization and truncation technique.

Chapter 6

Numerical modelling and analysis of heat flow in a single-pass butt welding seam

The problem investigated here, and as earlier described, is to model the heat-flow in a robotic weld. There are some assumptions made when studying the problem, which are regarded as reasonable. The whole process of multi pass-welding is very complex. From the fact that experience shows that the last pass of a weld is the most critical one (Grong 1994), the last pass of the weld will be the one analyzed here. The heat source is regarded as an optimal point source, moving at constant speed. The reason for this is to make the model as closely related as possible to the analytical solution used as a reference. The numerical modelling is done in a GUI-based program called Comsol MultiphysicsTM. The program is based on the theory explained in Chapter (4) about the FEM. The mass added in a pass of a weld is neglected, and the model simply becomes the equivalent to that of a Tungsten Inert Gas (TIG) source moving across the plate without adding filler-wire.

6.1 Construction of the model

The first approach to describe the problem using a mathematical model, was to create a single-pass weld in a $50mm$ thick plate. The heat source passed once over the plate on the top surface. The results, were as earlier described, compared to the solution deduced by Rosenthal.

As shown in Fig.(6.1), the mesh is refined along the centre line of the plate. This is where the heat-source is moved across, and this is done for two reasons. One reason is to make the model with as low complexity as possible, and to make the solution more exact along the line where the heat source is moved. The model itself is made with the same assumptions as the analytic solution. This means that the source is a point source, moved with a constant speed along the center line. The model itself takes into account transient effects. When comparing with the analytical solution, snapshots are taken of the temperature as a function of the position, as seen in Fig. (6.2). For more detailed information on how the model was made, see in Appendix A.

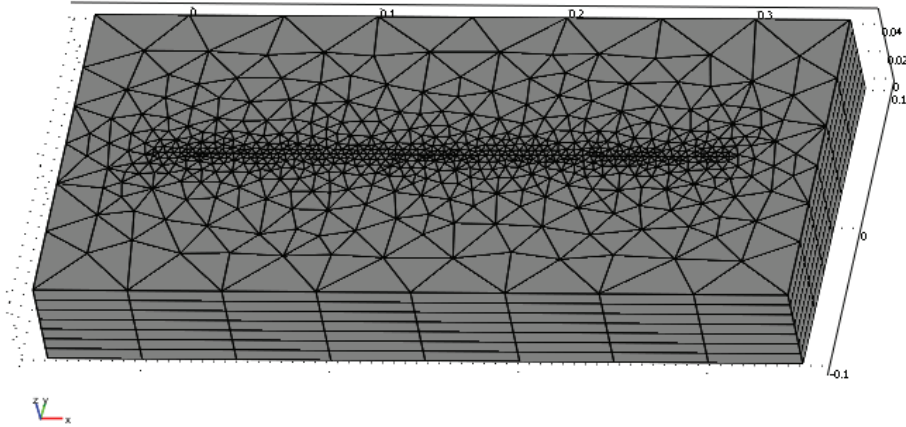


Figure 6.1: Meshed geometry of the steel plate. The weld was performed along the refined center line.

6.2 Response analysis

In order to validate the temperature distributions from the model, the temperature data from the model was plotted in Matlab, and compared to the solution from Rosenthal. The superior goal was to get a response which was within the range of 10% of the response from the analytical model. There were however some effects that had to be taken into account. The analytical solution has an infinite temperature in the origin of the moving reference frame. Because of this, the temperature peaks were not of major interest. However, the thing that was of more interest was the response after the heat source had passed. In this section, the scope is to show that the model has a satisfactory temperature response behind the source.

6.2.1 Relation between Q and q_0

The relationship between the two respective heat inputs in the model and the reference-model was a major task throughout the analysis of the heat distribution. This proved to be a difficult task, and it was decided to find the relation through trial and error, and find an expression such that it was easy to convert from one source to another. With the origin from Rosenthal and its heat input q_0 , extensive trial and error was done until a satisfactory result was found. The relationship between welding parameters and q_0 was found in (3.3). Relevant input parameters were taken from Appendix F. For each simulation, a β was found from the relation $\beta = \frac{Q}{q_0}$. After doing a sufficient amount of tests, an expression relating the above parameters was found, and is presented in Tab.6.1.

6.2.2 Relevant Plots

In order to validate the consistency of the model, it was tested for a multiple number of different input data. The focus was put on the $\Delta t_{8/5}$ value obtained from both the numerical and theoretical model. The late response in the model was also monitored, to be

Trial no.	Rosenthal's thick plate solution			Numerical model		
	Arc current [A]	q_0 [kJ/s]	$\Delta t_{8/5}$ [s]	Q	$\Delta t_{8/5}$ [s]	β
1	157.0	2888	1.69	$2.8 \cdot 10^6$	1.64	969.3
2	200.0	3680	2.16	$3.6 \cdot 10^6$	2.16	978.3
3	250.0	4600	2.70	$4.4 \cdot 10^6$	2.70	956.5
4	275	5072	2.97	$5.2 \cdot 10^6$	3.07	1025.0
5	320.0	5888	3.45	$6.6 \cdot 10^6$	3.52	1120.0

Table 6.1: Inputs and relevant data obtained from the different trials.

certain that the model will adapt to a multi pass environment. Plots of both the bottom and top surface were taken, in order to check if the welded specimen was semi-infinite as defined in Chapter (3). The plate is considered as semi-infinite if the temperature does not rise before after the source has passed the point. It will be more clear when looking at the plots. The current was varied in the trials, but the voltage was kept at 23[V] and η was set to 0.8 while the speed ν was kept at a constant rate equal to 0.005 m/s. For figures of trial no. 2-5, look in Appendix B.

6.3 Discussion

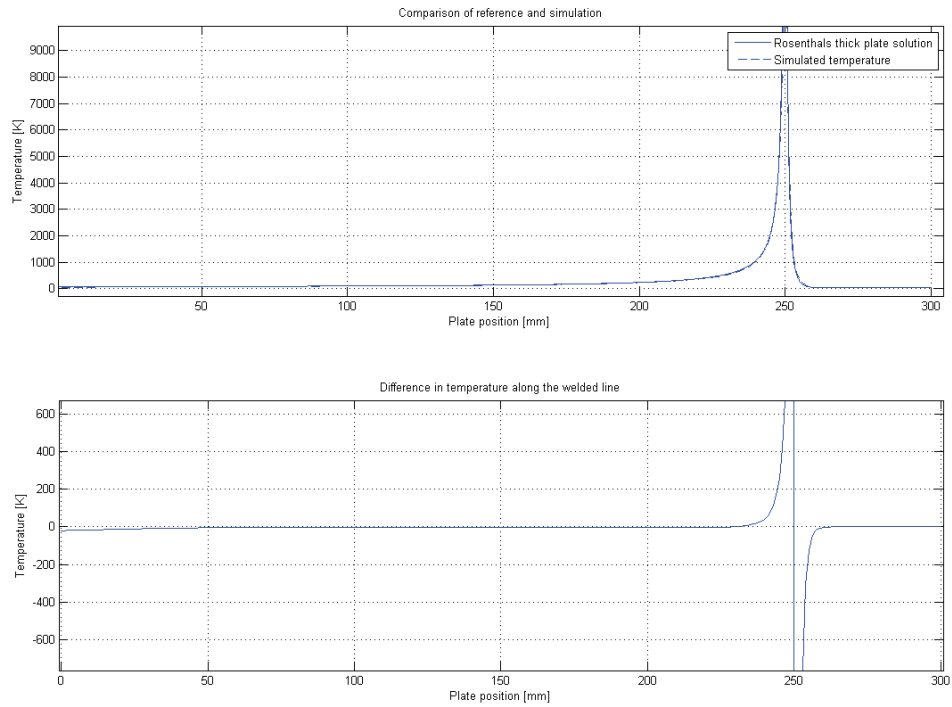
The results obtained in this chapter are based on numerical modelling done by the FEM, and will never be an exact copy of real life. This is however not the objective of the modelling. As this model in future work will be used in a control context, one would like a model which is reasonable in its physics, and still be as simple as possible. Errors in the modelling will be taken care of by the closed loop system. Because of this, one can allow simplifications and errors. In this model, the target was to stay within 10% of the reference temperature when looking at the temperature response before and after the heat-source has passed. The response in front of the heat-source comes from the physical fact that heat conducts forward in the material, and the slopes abruptness will follow from the heat-input and the welding speed. A high speed will thus give a steep curve, while a high heat-input will slacken the gradient. In the tests performed in this work, the speed has been kept constant and the only parameter which has been changed is the current. This is a valid assumption due to the fact that speed is kept constant in most robotic welding applications, and the only parameter being changed is the current and voltage.

The response in front of the heat-source is not of great importance, but is a good indicator for the validity of the model. The results show that the temperature in both model and reference starts to rise at the same point on the plate. The reference will, due to the singularity in origin rise to infinity, and thus have a gradient $\nabla_T \rightarrow \infty$. For the model, this will lead to significant deviance close to the origin. When looking in Fig.6.2c and Appendix B, it may be observed that the curves of the model shows some signs of low resolution. This is simply due to the fact that the curve from the FEM-model only is sampled each 0.5 second.

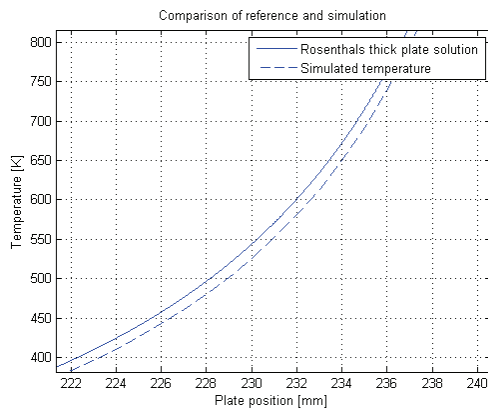
The peak temperature is not much emphasized in this projects work. The reference model has a singularity in the origin, and will in that point give an infinite temperature. The model will also not be completely valid at peak temperatures, because of the resolution of the mesh along the center line.

The response after the source has passed is more or less an equivalent to the heat equation in the homogeneous form, and is governed by the initial temperature and the physical properties of the material. The rate at which the temperature decays, will be reasonably low, meaning that the model will be able to follow with greater accuracy. This also means that the relatively coarse resolution of the mesh will be of less importance when reaching the point at which the temperature is in the transition between 800°C and 500 °C. This transition period is the one with highest priority. As earlier described, this is the interval at which the austenite to ferrite transformation takes place, and the mechanical properties of the weld is established. To secure this characteristic, it is important to keep $\Delta t_{8/5}$ as close to constant as possible for the whole length of the bead. It can be seen from the plots of the temperature response in Fig.6.2 and Appendix B, with the relation on β established, that the two trajectories are close to each other.

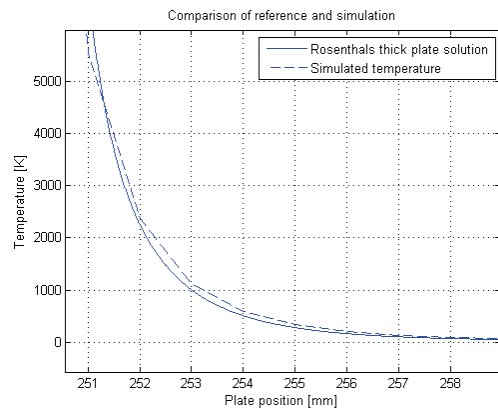
One of the criteria for the model of Rosenthal to be valid, is that the welded specimen is semi-infinite, as explained earlier. Looking at Fig.6.3, it can be seen that the plate experiences complete penetration at each pass. This will not make the model valid for this case. The present would be valid for a medium-thick plate solution, but as this is not part of the scope of this project, it will not be further pursued. A remedy for this is to simply



(a) Direct comparison of the temperature and temperature-difference in the responses.



(b) Temperature decay rate.



(c) Temperature increase rate

Figure 6.2: Comparison plots of the from trial number 1. Input into Rosenthal: $I = 157$ [A], $U = 23$ [V] and $\eta = 0.8$.

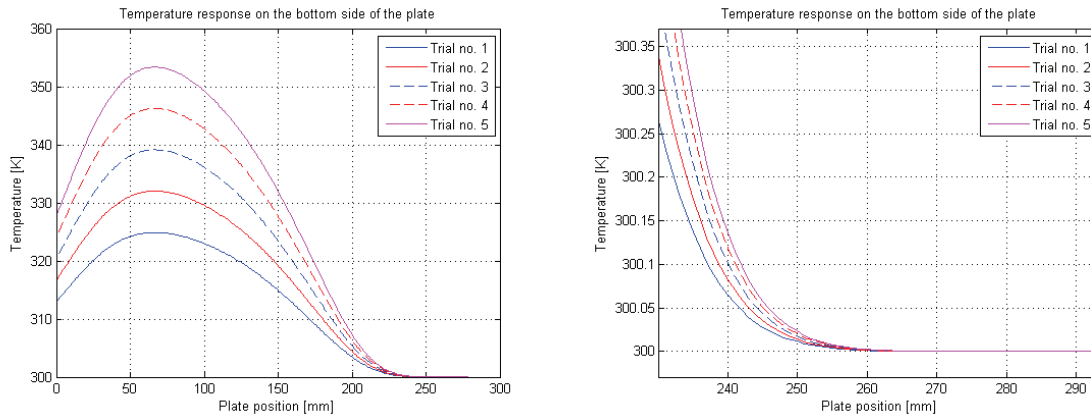
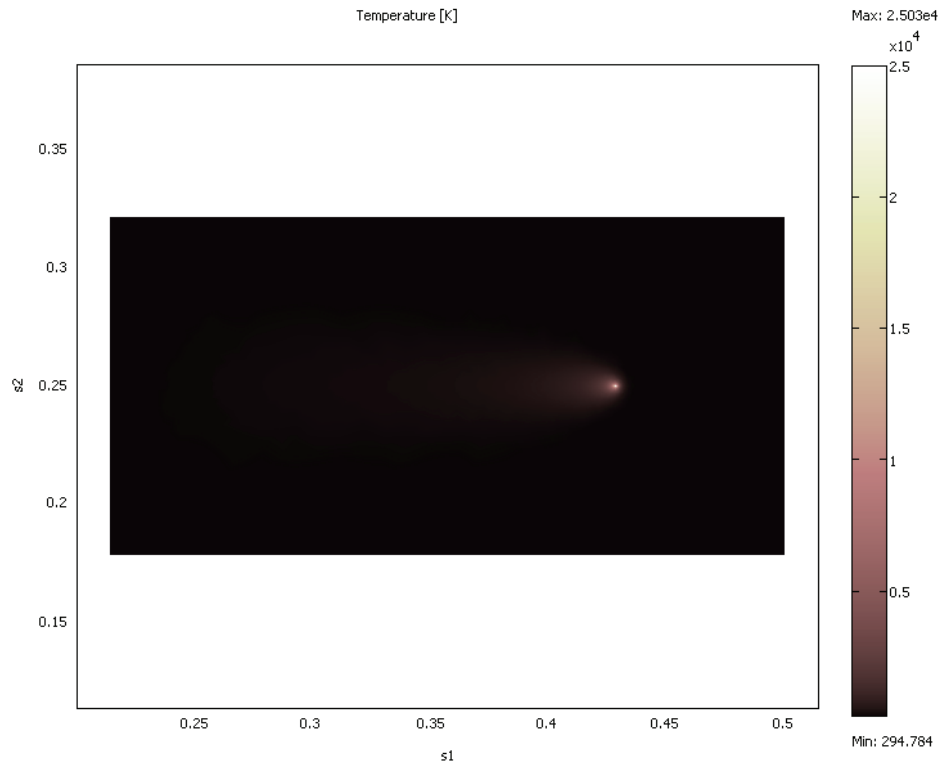


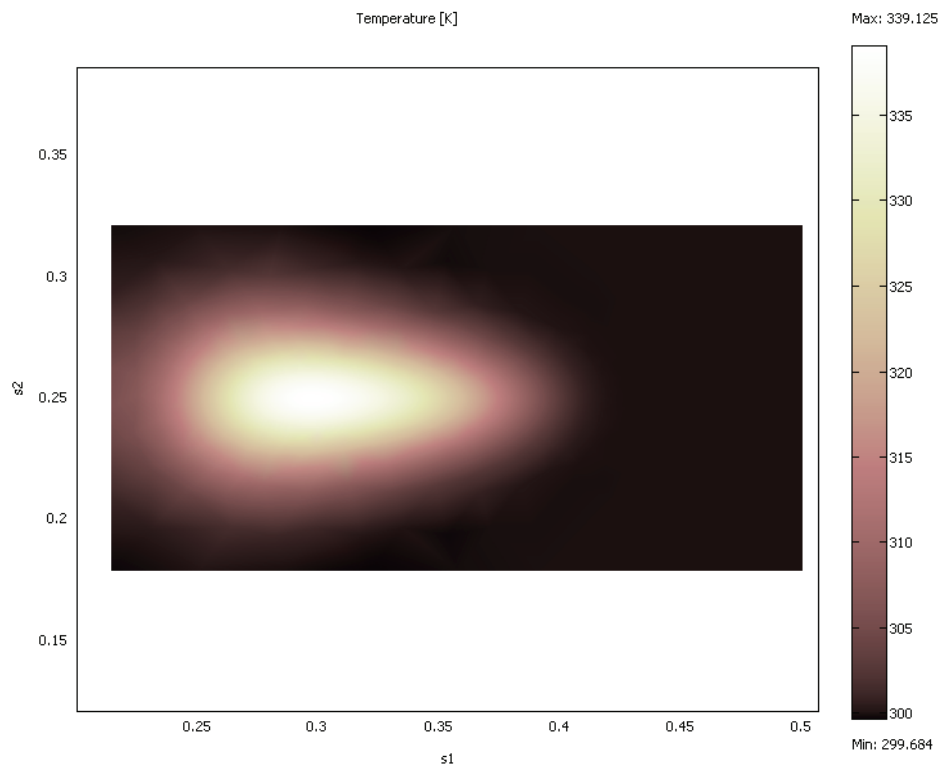
Figure 6.3: Temperature plot of the bottom surface of the welded plates. The different curves represents the different inputs into the model.

increase the plate thickness in the numerical model. Due to limitations in computer-power when performing the simulations, it was not possible to increase plate thickness in the present case. An increase in plate-thickness would make the model more closely related to the reference model, and thus giving a better response.

From Fig.6.6 and Table 6.1, one may analyze the data acquired and see how well the model performs. If one starts to look at Fig.6.6a, which is a presentation of the different $\Delta t_{8/5}$ found from the trials, it can be seen that the two values found for each consecutive test are close to each other. As expected the cooling time increases with heat-input. It can be seen from Fig.6.2 and Appendix B, that the shape of the curves are completely decoupled from the input. The interval $\Delta t_{8/5}$ will occur at a later position in the temperature response, and thus have a slacker gradient giving a longer cooling time in the specified interval. Fig.6.6c shows the plots of the percentage deviation the numerical model has from the two different references. It can be seen that all trials are well within 10% of the analytic solution with the maximal deviation of 3.22%. Which is a good result, regarding the problem with not being able to make a model satisfying the semi-infinte body requirement.



(a) Temperature on the surface where the heat source is located



(b) Temperature on the bottom side of the plate. The plot represents the heat-source penetrating the plate.

Figure 6.4: Surface temperature plots taken at $T = 50s$.

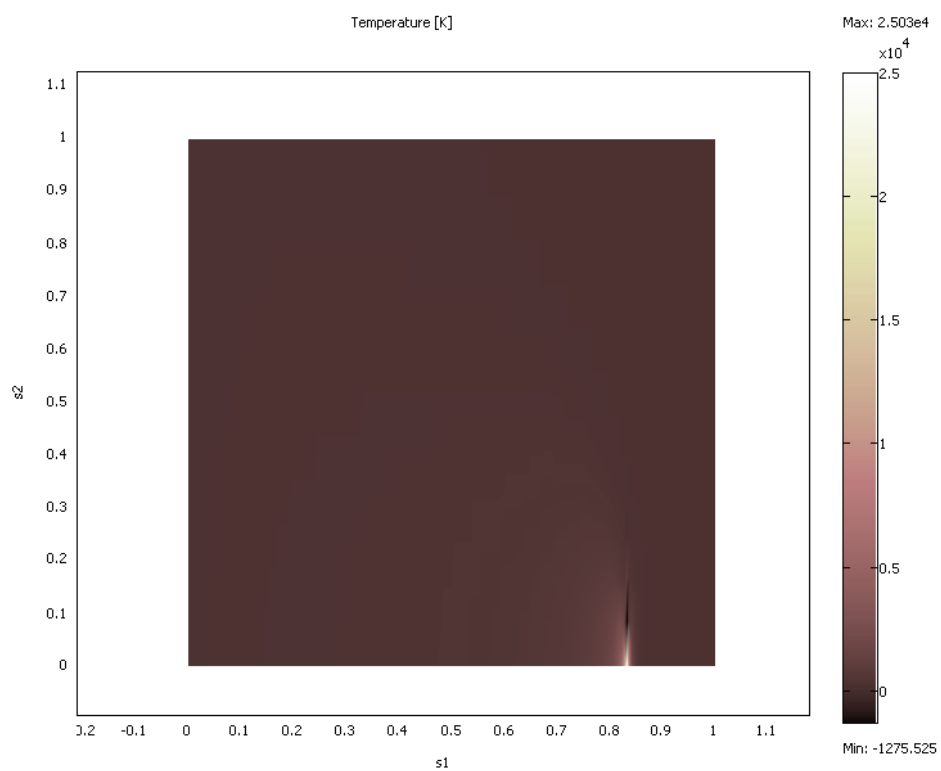
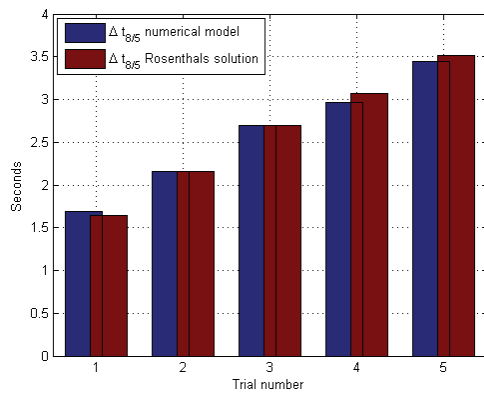
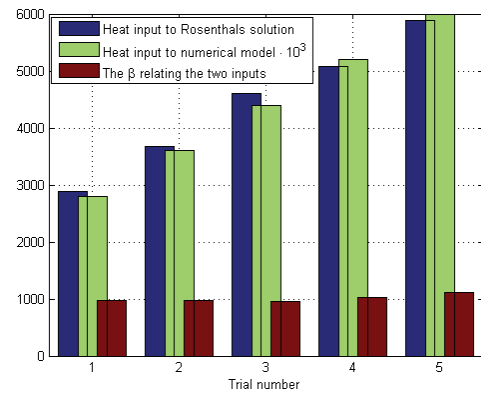


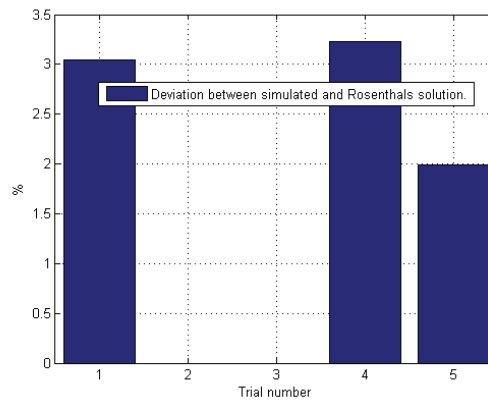
Figure 6.5: Temperature cross sectional plot along the welded center line taken at $T = 50s$. The Y-axis represents the penetration depth of the heat source, where the source is located at $Y=0$.



(a) The $\Delta t_{8/5}$ relation to each other.



(b) The relation parameter β together with the heat inputs q and Q .



(c) Deviation in % from the numerical model and the two different references.

Figure 6.6: Figures of $\Delta t_{8/5}$, the relation between heat inputs and statistics.

Chapter 7

Applying POD to the numerical FEM-model

The model developed in Chapter 6 is highly nonlinear, and has a complex nature. By using the theory from Chapter 5, it is possible to minimize the number of states needed in order to duplicate the response obtained in the nonlinear model. As earlier described, the transition region $\Delta t_{8/5}$ is important. In this chapter, the late response in the model is also important, making it possible to monitor the initial temperature for the next pass.

7.1 Linearizing the model

The following section used the same parameters as in Tab.6.1. The FEM-model was linearized around a time $t = t_0$, and exported to Matlab in the form

$$\begin{aligned} M\dot{x} &= MAx + MBu \\ y &= Cx + Du. \end{aligned} \tag{7.1}$$

The constraints (Dirichlet boundary conditions) were eliminated by writing the solution vector U as

$$U = Nullx + U_0, \tag{7.2}$$

where U_0 is the linearization point, and $Null$ is the null-space matrix for the constraints. To make the case as realistic as possible, the output was measured in a point on the body as seen in Fig.7.1, measuring the temperature as a function of time. When using the parameters set in Chapter 6, the source will pass over the highlighted point in Fig.7.1 at $t_0 = 30[s]$. The point in blue represents the source and will in the FEM-model move at a constant speed. When linearizing the model, one will make the point, representing the source, stationary. Fig.7.1 represents the plate at $t = 34[s]$.

First, the general dynamics at the respective points in time were investigated. The difference between the respective states at linearization points $t_0 = 31[s]$ and $t_0 = 33[s]$ are shown in Fig.7.2. Fig.C.1 represents the difference between the state matrix at two other linearization points $t = t_0$. It may be observed that the difference between the states are very small, and in particular in the first 5200 states, which represents the 3D-domain. Combining this with the fact that all the systems are stable, with eigenvalues

between $\lambda = 0$ and $\lambda = -16.163$. The eigenvalue distribution for $t_0 = 35$ may be seen in Fig.C.2. This means that the respective systems will behave almost identical for initial value problems, where the source is $u = 0$.

The last 52 states represents the 1D movable source. The relative position of the source in the plate is governed by the linearization point. The heat source's effect on the measured output may be seen in Fig.7.3. There are two effects that may be observed here. The first it that the peak temperature is lower, for later linearization points. This effect is due to the fact that the source is not capable of heating the entire plate due to loss in heat through the plate to the surroundings. The delay in temperature rise in the output is because of the relative position of the source (Fig.7.1), and the heat needs to conduct in the body toward the measurement point before temperature starts to rise. It may be observed that some of the temperature responses have a negative initial response containing oscillations. This may be explained by the complex poles in the system matrix and possible zeros in the right half plane.

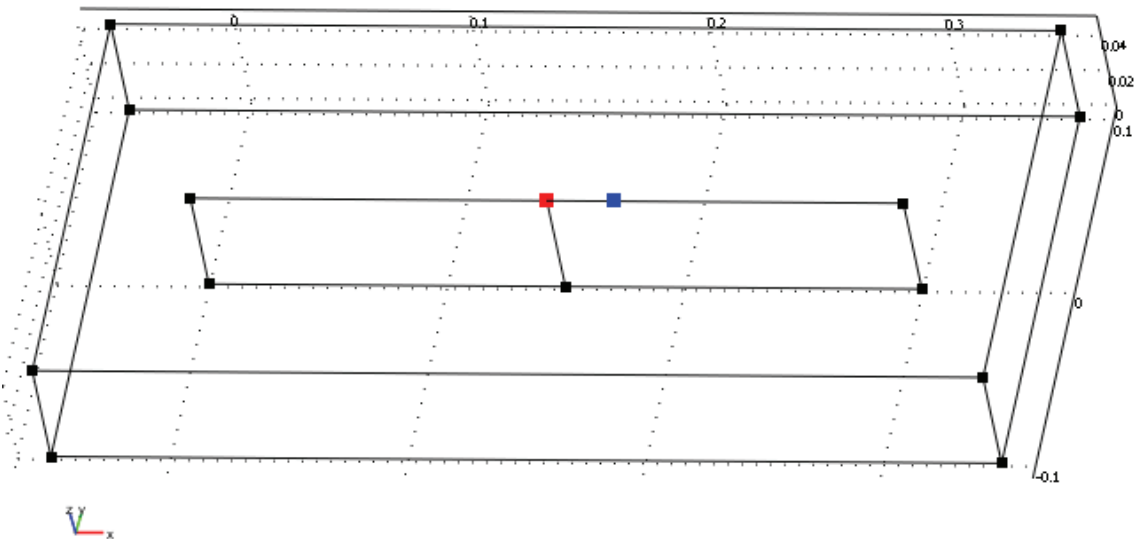


Figure 7.1: Relative position of measurement point and source at $t = 34[s]$. The source (in blue) will continuously move in the FEM-model, but will be stationary in the linear model.

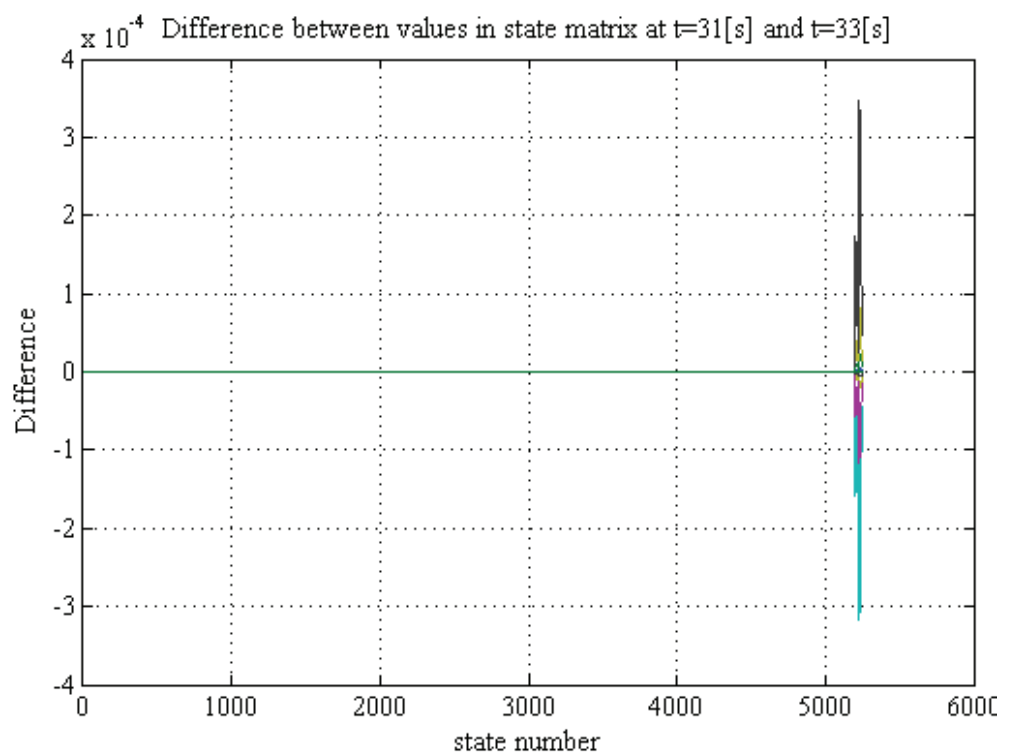


Figure 7.2: Difference between the states in the state matrix at linearization points $t_0 = 31[s]$ and $t_0 = 33[s]$.

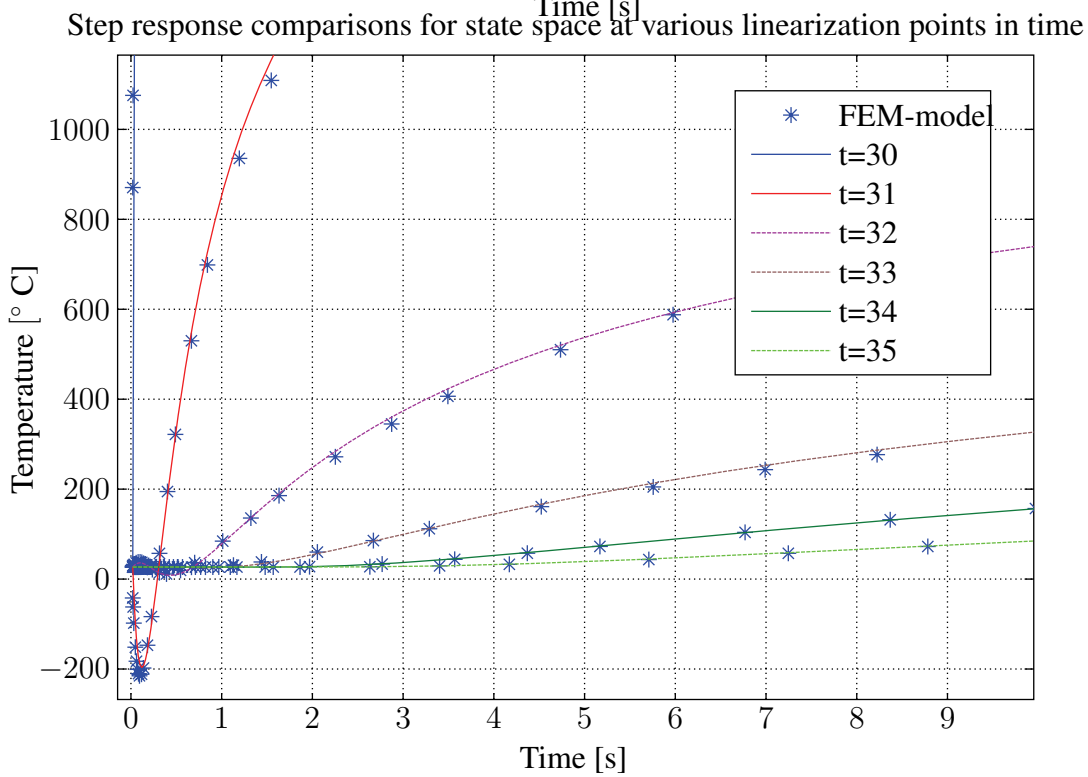
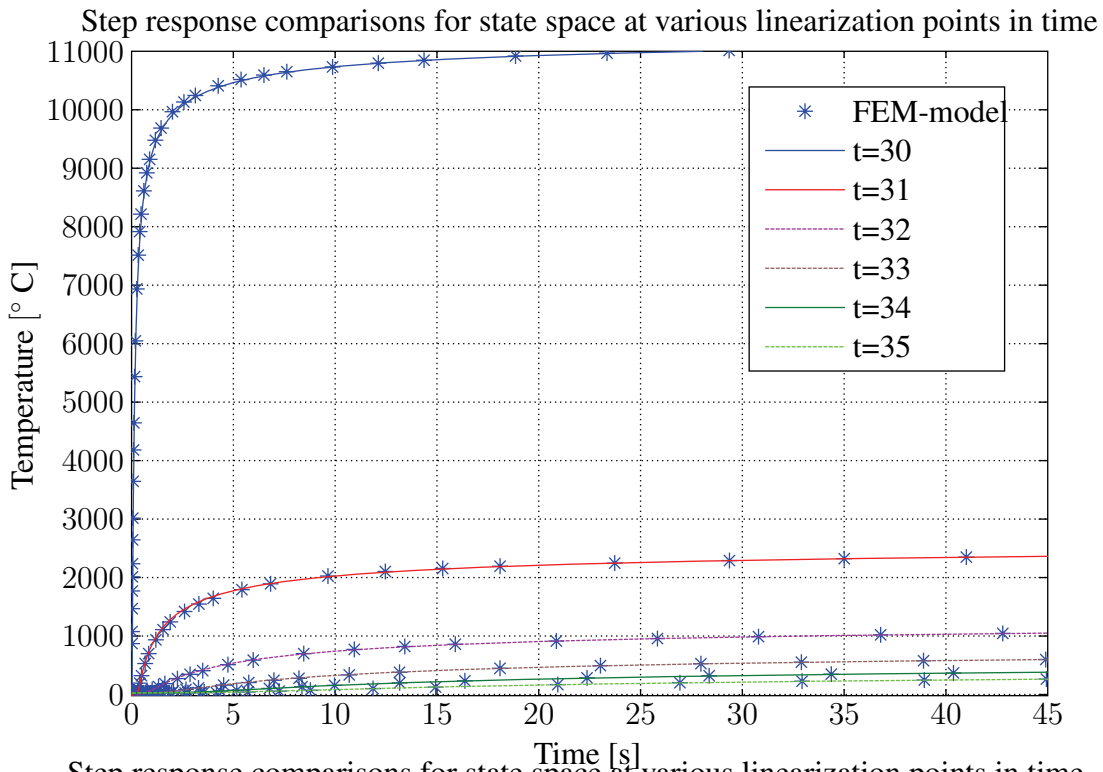


Figure 7.3: Step response seen from the output of the system at various linearization points t_0 , compared with similar simulations done on a stationary source FEM-model.

7.2 Reducing the order of the model

When the linear model was obtained, the relative position of the states on the plate had to be acquired. Because the mesh is refined along the centre-line of the model, as can be seen in Fig.6.1, the states are not uniformly distributed over the body. The relative position of the states can be seen in Fig.7.4. It can be easily observed that the number of states along the refined mesh centre line are higher than in the more peripheral parts of the body. This is to retain accuracy and still keep the number of states at a minimum. There will be presented three different procedures for reducing the model, and the main difference will be the way in which the snapshot matrix will be designed.

7.2.1 Snapshot matrix from one simulation

After the states relative position were obtained, it was possible to acquire initial values from the FEM-model, similar to that of Fig.7.5. It is a representation of the temperature in the top-sheet in the plate at $t = 32[s]$. By simulating the free response of the linear system with the initial value set as in Fig.7.5, snapshots mirroring the dynamics in the full rank linear model were obtained. Applying POD to these snapshots, the model with the result presented in Fig.7.6 was computed. When further looking at Fig.7.6, one may see that with just 10 states, the reduced model manages to closely follow the full rank linear model with with a maximum deviation of 0.24%. The problem however, is that the deviation between the reduced model, and then also the full rank model, is larger. The maximum deviation is slightly above 14%, which is outside the preset target of 10%. Looking at the $\Delta t_{8/5}$, the error is 34.8%. Applying (5.9) yields that the reduced model mirrors 99.98% of the energy in the snapshot matrix. The full rank model used 5727.25[s] in completing a total of 2500 time steps. Comparing this with the reduced order model, the same amount of time steps took a total of 0.0956[s], only $1.67 \times 10^{-3}\%$ of the time.

7.2.2 Snapshot matrix from several initial value simulations

As the previous section failed to miss the desired error, the next step was to create a snapshot matrix mirroring more dynamics of the system as explained in Chapter 5. By doing several initial value problems similar to the above section, it was possible to create a compound matrix. When solving initial value problems, the early stage in the response has close to no deviation, and the error will normally increase with time. By creating a "library" of initial value problems solved at different initial points in time, it was possible to build the desired response from Rosenthal, by building up a compound snapshot matrix. The response from some of the initial value problems may be seen together with the solution of Rosenthal in Fig.C.3. By only using snapshots from the linear response where it stays within 10% of the reference trajectory, the compound matrix in Tab.7.1 was created.

Performing POD on the compound snapshot matrix, and simulating the resulting reduced system, gives the response seen in Fig.7.7. Investigating the response obtained, it's quite clear that the reduced model now has a response closer to the desired trajectory. The number of states in the reduced model had to be increased in order to mirror enough of the dynamics in the snapshot matrix. Investigating the total amount of energy captured from

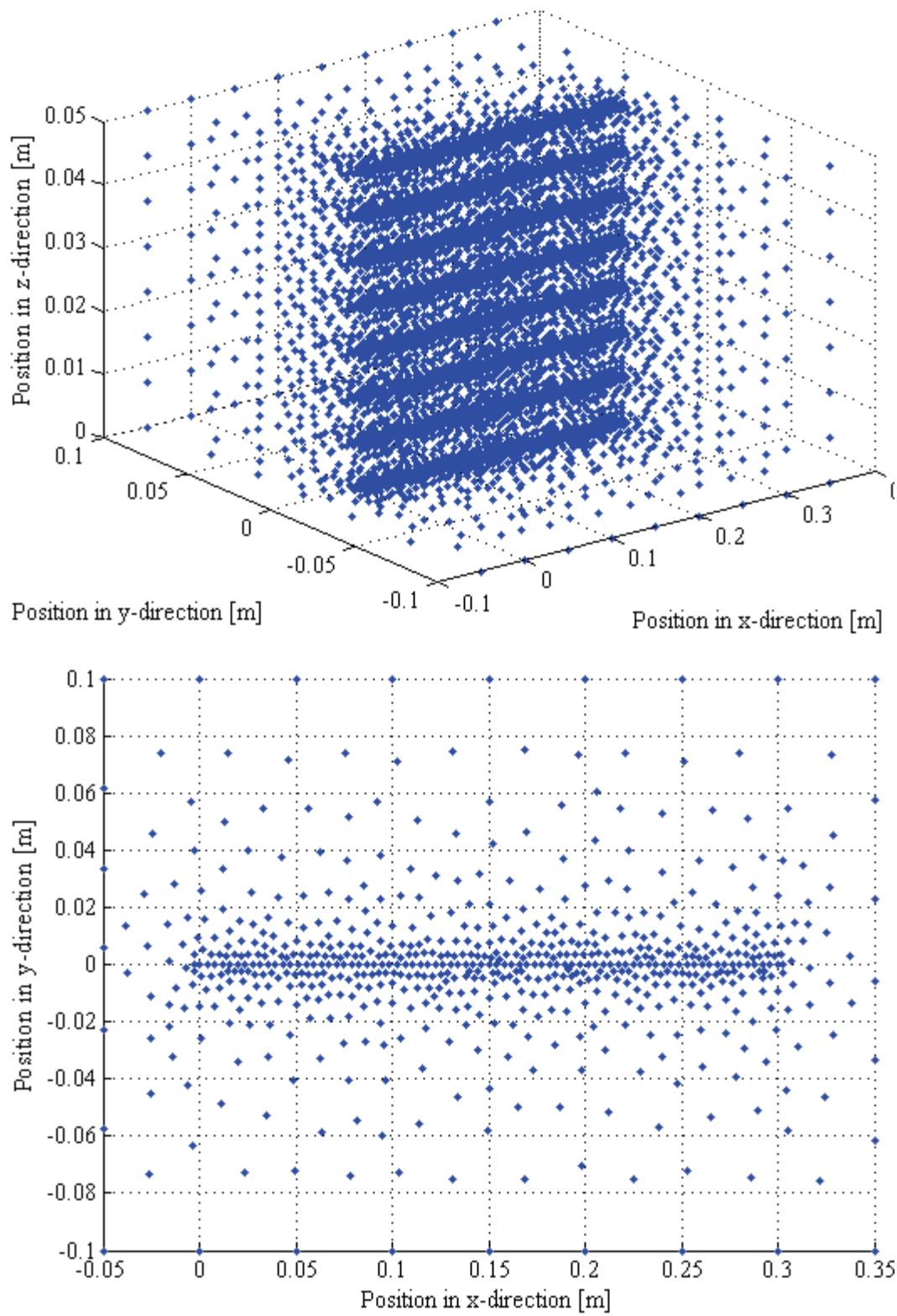


Figure 7.4: View of the distribution of the states in the plate

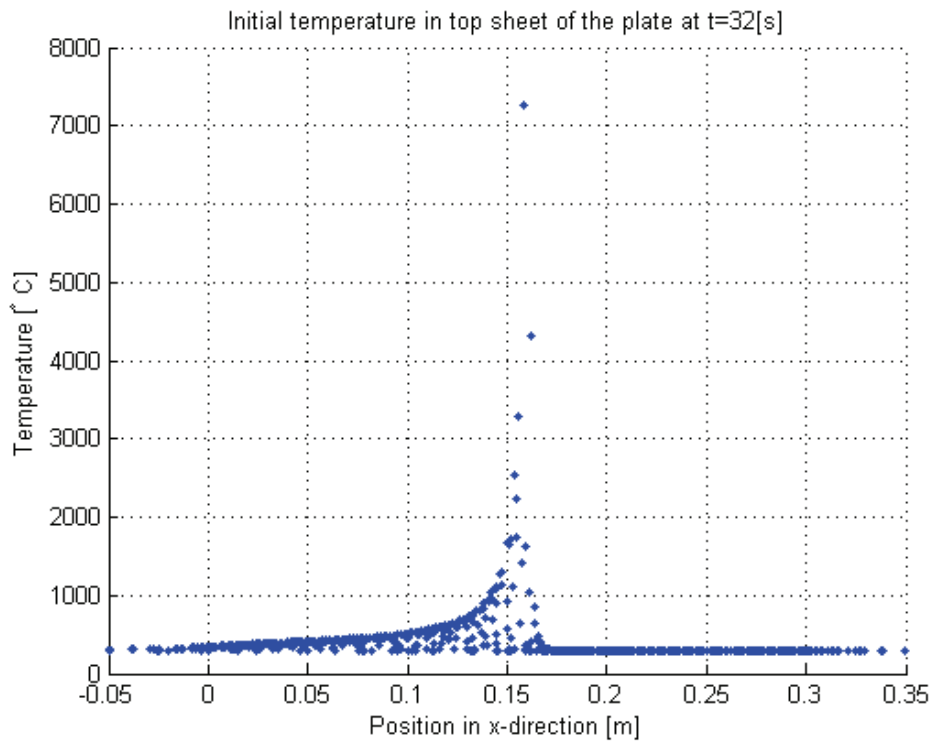
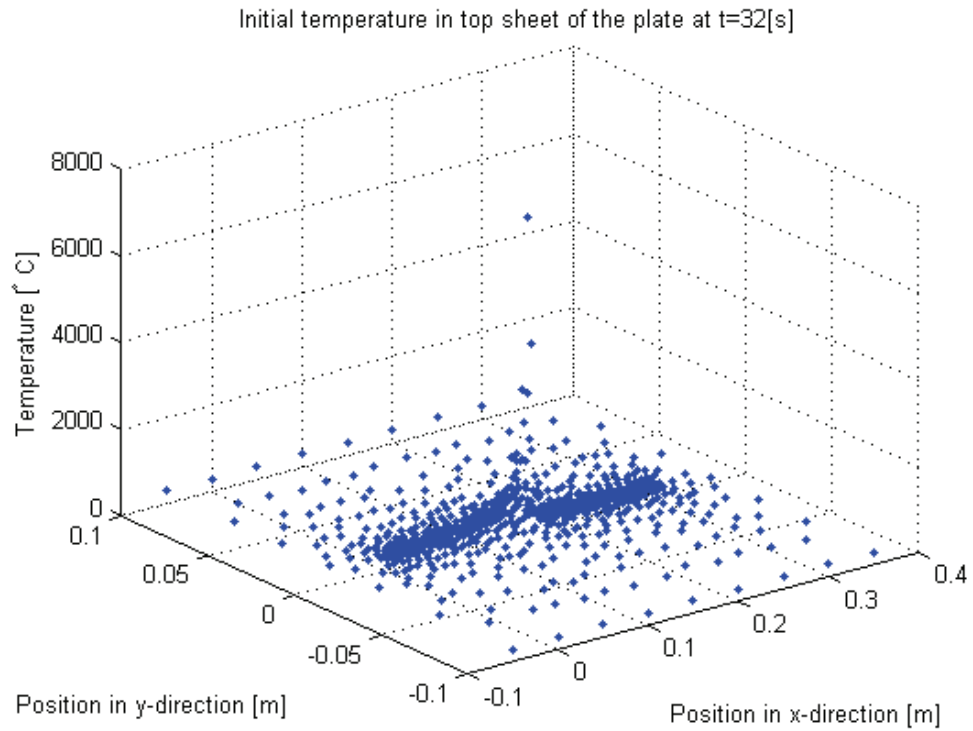


Figure 7.5: Initial value in the top sheet of the plate at $t = 32[s]$.

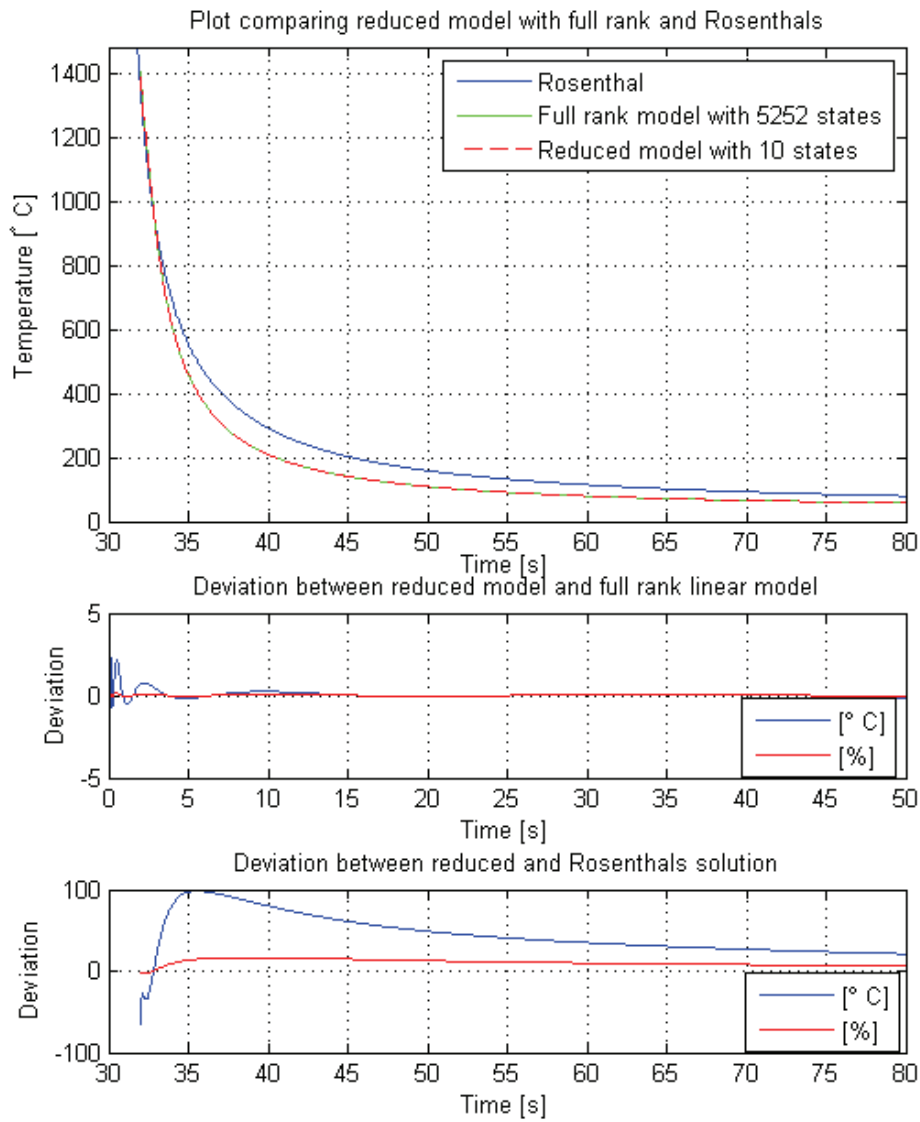


Figure 7.6: Comparison in output between Rosenthals solution and initial value solution for state space linearized around $t_0 = 33[s]$ with initial value set as in Fig.7.5.

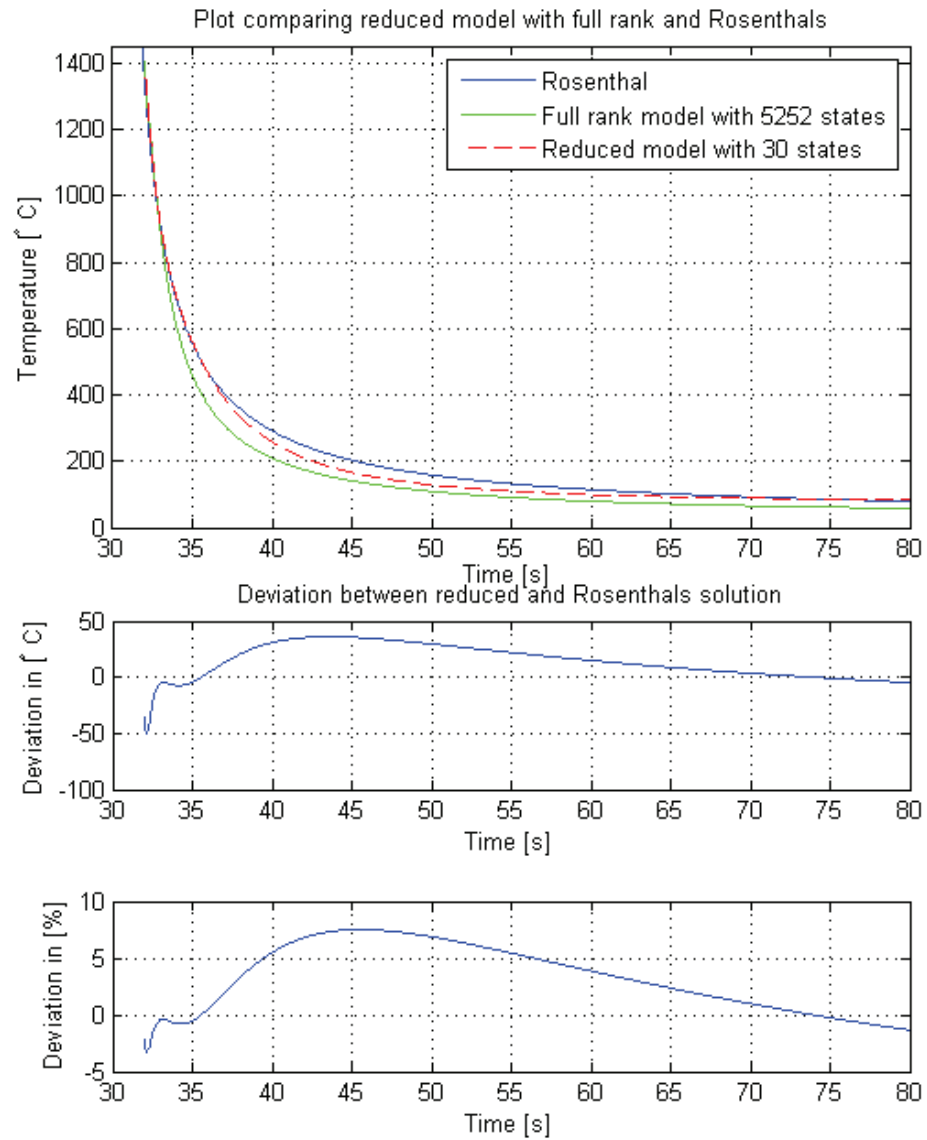


Figure 7.7: Comparison in output between Rosenthals solution and initial value solution for reduced state space linearized around $t_0 = 33[s]$ with initial value set as in Fig.7.5. The snapshot matrix was created with multiple simulations.

Initial value from time t [s]	Seconds within desired deviation	Number of samples
32	1	50
33	1	50
34	1	50
35	4	200
36	13	650
40	5	250
45	15	750
50	10	500
Total number of snapshots		2500

Table 7.1: Build up of the snapshot matrix with state space linearized at $t_0 = 33[s]$

the snapshot matrix with 30 states using (5.9), gives a result of 99.11%. When looking at the deviation in %, the maximum deviation between Rosenthal and the reduced space is well within 10%, with a maximum error of 7.51%. The error in $\Delta t_{8/5}$ is only 0.9%, and well within specifications. Using the same run time for the full rank model as above, with a total of 5727.25[s], the reduced model needs 0.192% of the time, clocking in on 11.00[s].

7.2.3 Snapshot matrix from several simulations including input u

The next step in creating the reduced model, mirroring the dynamics from Rosenthal's thick plate solution was to include a driving input to the system. The objective was to create the "initial value", which was preset in the above sections, with the input u . The first 10[s] from $t = 31[s]$ in Fig.7.3 was added to the snapshot matrix in Tab.7.1. This resulted in a total of 3000 snapshots. Ignoring the region at which the heat source is switched on, the error in Fig.7.8 has a maximum error of 6.29%. The input u is set to 1 in the interval at which the heat source is switched on for a period of 12.5[s]. The reason for this time period being relatively long, and not following the increase in heat as in Rosenthal, is the disadvantage of not having a moving source which is present in the FEM-model. It becomes more clear, when looking at Fig.7.9, that the heat source in the linear model is not capable of creating the same temperature distribution as in Fig.7.5. Looking at the error in $\Delta t_{8/5}$ compared to Rosenthal, the error is 7.9%. And meets the specifications set before hand. From (5.9), one gets that the total amount of energy mirrored from the snapshot matrix is 99.87%. When looking at the run time for the model including the input u , it is more difficult to find a comparison. If only looking at the general run time, the reduced order model with 50 states uses 0.16[s] completing 2500 time steps.

7.2.4 Applying other inputs to the reduced model

To further investigate the performance of the reduced model, the input u was changed according to the input values used in Tab.6.1. Directly comparing the results with Rosenthal, gives the response seen in Fig.7.10, and Fig.C.4-C.6. One may identify that the devia-

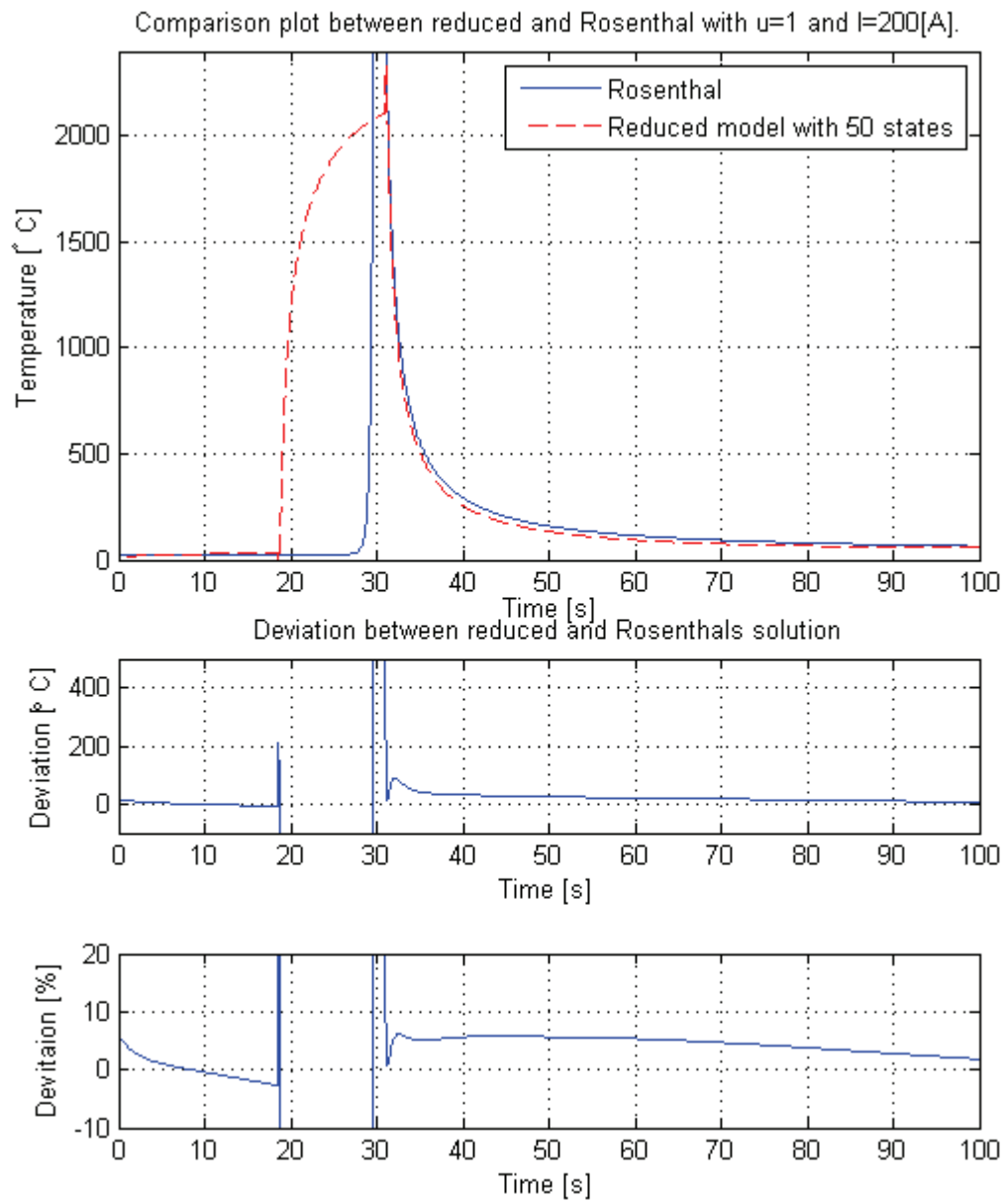


Figure 7.8: Comparison plot between reduced space model, and Rosenthal. The heat input is similar to that of trial no. 2 in Tab.6.1. The reduced model originates from a linear full rank model linearized around $t_0 = 31[s]$.

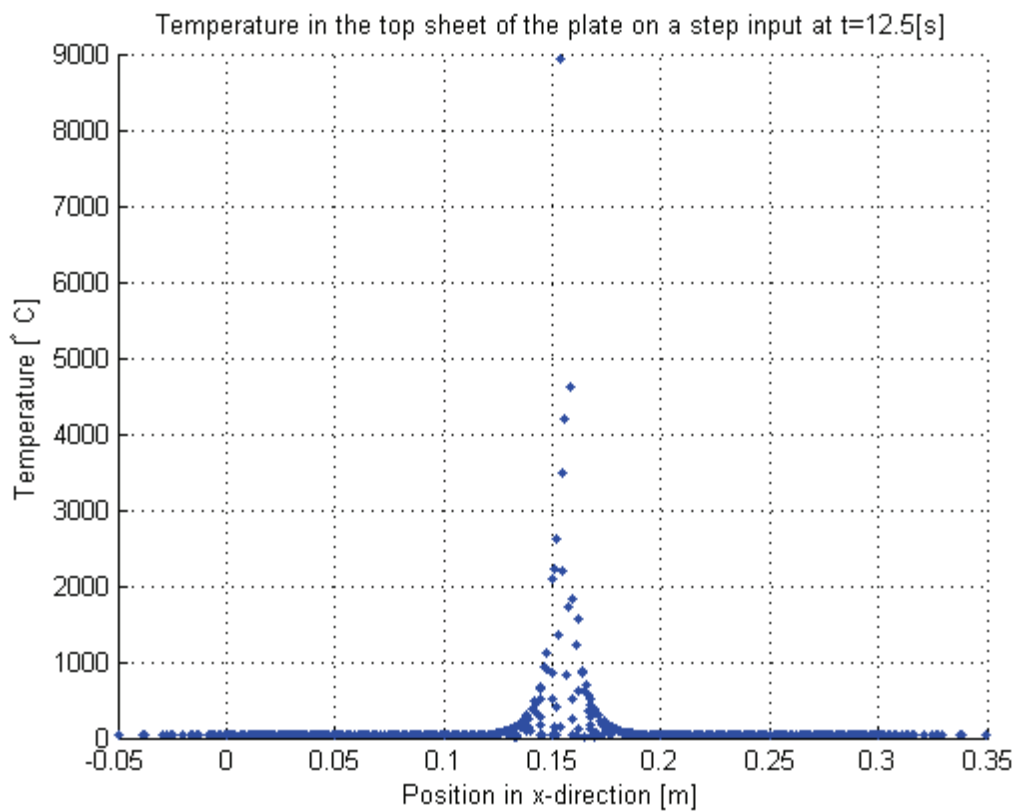
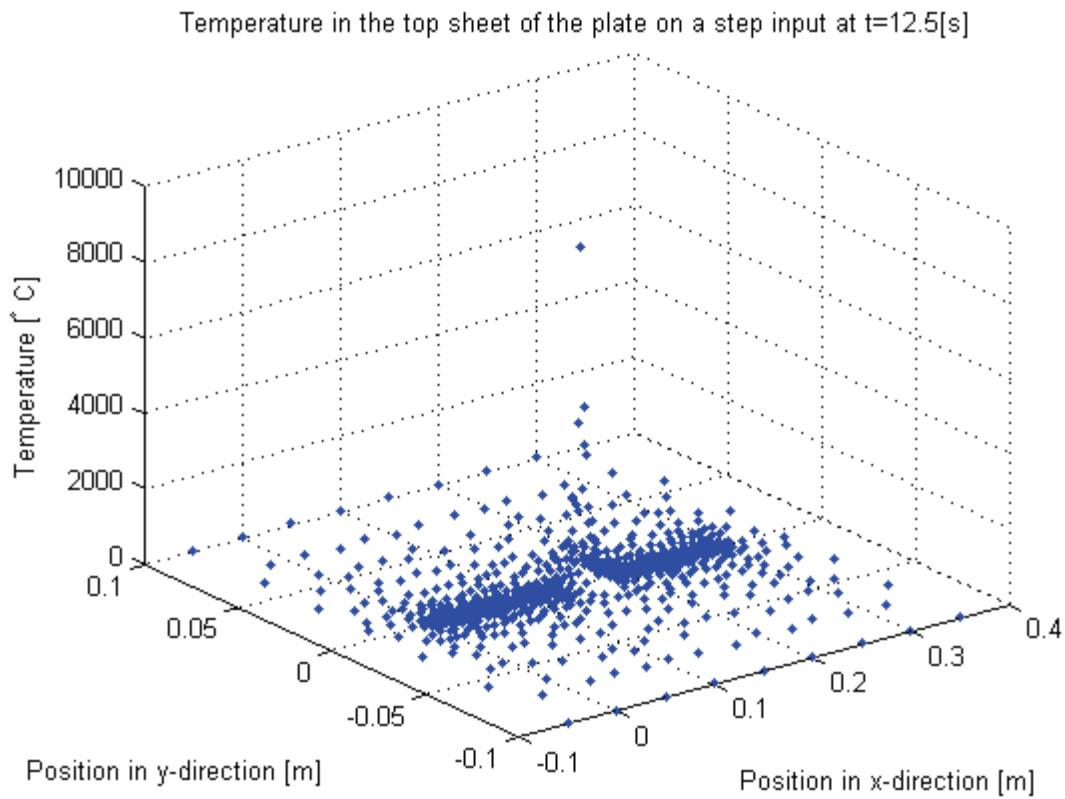


Figure 7.9: View of the top surface temperature in the plate from the step input after 12.5[s].

tion in % is within 10% of the desired trajectory for all cases. The reason for why this is possible, becomes clear when looking at Fig.C.7, showing the difference between the states in two different state space models with linearization around $t_0 = 31[s]$ and different heat inputs u . As one may see, the difference is only in the last 52 states representing the 1D-domain and the heat source as explained earlier in this chapter.

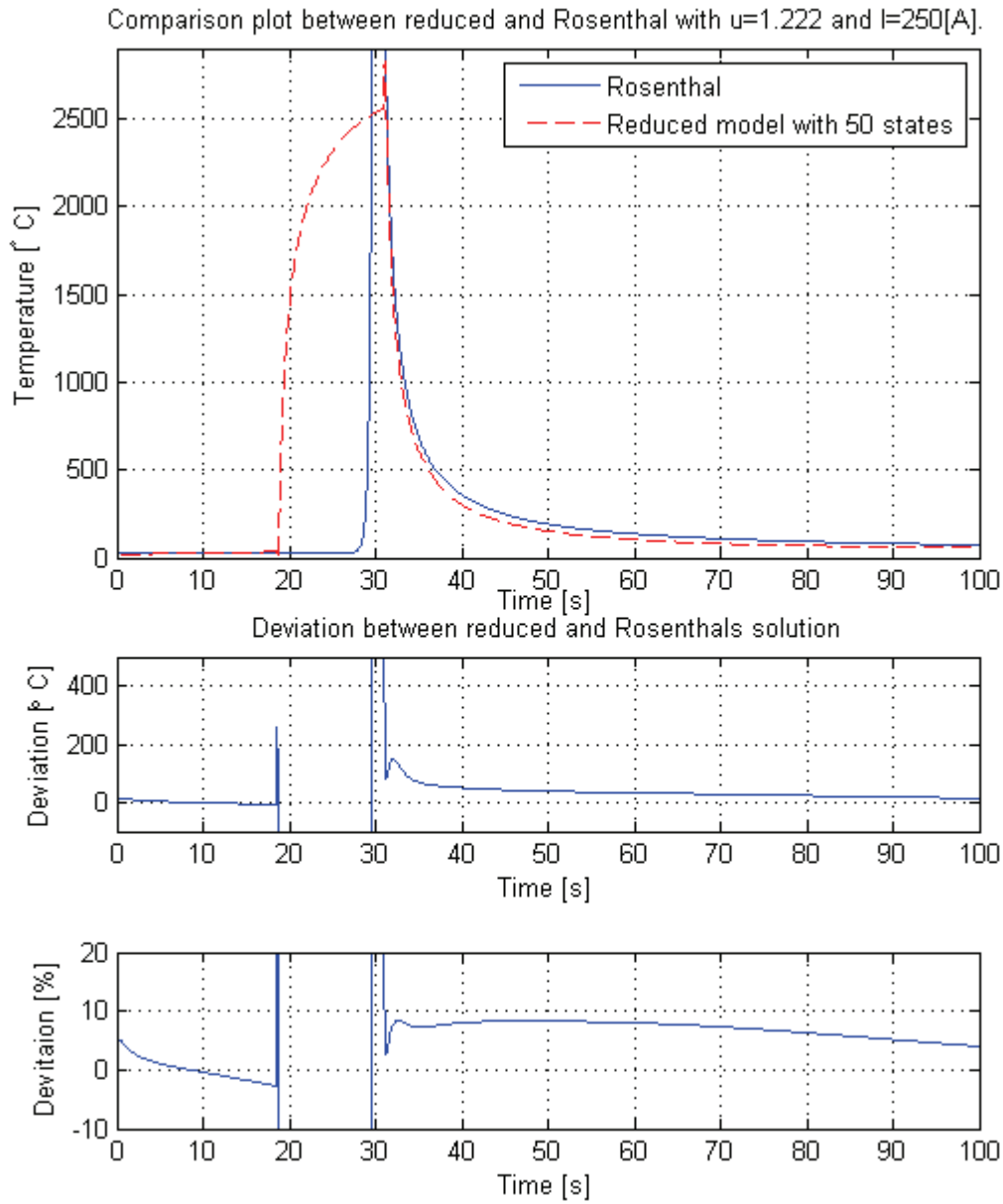


Figure 7.10: Comparison plot between reduced model and Rosenthal. Heat input similar to that of trial no. 3 Tab.6.1 The reduced model originates from a linear full rank model linearized around $t_0 = 31[s]$.

7.3 Discussion and evaluation

Throughout this chapter, the progress in creating a reduced space model has been shown. Looking at the reduced models performance, compared to the reference model deduced by Rosenthal, it is quite clear that the linear model has problems in copying the correct response. Looking at the full-rank linear model response in Fig.7.6, the temperature decreases too fast in the $\Delta t_{8/5}$ transition with an error of 14.1%. The same characteristics repeat themselves in the reduced space.

By manipulating the content of the snapshot matrix, it was possible to lift the response in order to decrease the error in $\Delta t_{8/5}$. This was done without increasing the error in the late response. In Fig.7.7 it is clear that the reduced space model no longer follows the full rank linear model. As a paradox, increasing the number of states forces the response in the $\Delta t_{8/5}$ -region closer to the full rank linear model. This is because the snapshot matrix does not manage to completely copy the response of Rosenthal. If including enough energy in the reduced model, the resulting response will come closer to the linear full rank model. As a trade off, and because the main objective is to follow the response from Rosenthal, the error between reduced and full rank linear model is accepted.

When further introducing the input u to the reduced model, another problem arise. The property in the FEM-model of having a moving source gives rise to the good recreation of the response similar to Rosenthal. This property is not present in the linear model. The source becomes stationary, and does not give the opportunity to create a temperature distribution as in Fig.7.5. When linearizing around $t_0 = 31[s]$ as done for the last sections in this chapter, the stationary source will make the initial value will look like the one in Fig.7.9 after 12.5[s]. Reaching the point at which the sufficient amount of heat was passed to the plate included an extensive amount of trial and error. If having the source switched on for a shorter period of time, trying to exactly copy the Rosenthal response, the decay in temperature is too high when comparing to Rosenthal. This will introduce a major insecurity in the general performance of the model. In an online system, it might prove difficult to recreate the response obtained with the heat input every time. The tests performed here, show good results. However, there are no guarantees that the stationary source will give a valid temperature distribution for every single case. Despite the insecurities regarding the source, the model proves to have a good response for inputs u outside the linearization point. The reason for this is as earlier described due to the fact that the linearization of the FEM-model yields virtually the same linear full rank model for two different heat-inputs linearized around the same point. This is shown in Fig.C.7. This makes the method of creating this model versatile in the sense that it yields good response for a large interval of inputs. When tested for the inputs in Tab.6.1, the deviation never exceed 10% for the response after the heat source is turned off. It is natural that the error is large in the region at which the heat source is switched on. This region will be neglected when evaluating the error.

Chapter 8

Temperature experiments at Aker Kværner Verdal

In this section the procedures for the experiments done at Aker Kværner Verdal (AKV) will be shown. The test contains temperature measurements for welds performed with a wide variety of parameters. The tests were performed within specified procedures worked out at AKV shown in (Helden & Dreyer 1999). The experiments were performed as part of the development of an automated temperature control-system. The measurements will be used as decision parameters when controlling the $\Delta t_{8/5}$ in the welded specimen.

8.1 Test rig and set up

The setup for the test consisted of the following and can be seen in Fig.8.1:

- ThermaCAMTM S65 infrared camera
- Fujitsu Siemens lifebook laptop computer with FireWire interface
- Structural steel sheet with measures $1100mm \times 800mm \times 50mm$
- IRB2400L ABB 6DOF robotic welding manipulator
- Camera tripod mount

8.2 Test procedures

Previous to the tests, a test plan was prepared. The objective of the test plan was to span the entire temperature- and input parameters-interval encountered during normal welding. The tests were divided into sessions, and there were done a total of 8 sessions. Each session was designed to stress relevant settings at distinct situations. To test the consistency and accuracy of $\Delta t_{8/5}$, the analytical solution of Rosenthal (3.10) was used as a reference, and is referred to as the *Calculated* solution. The camera was set up according to (FLI 2006) and resulted in Tab.8.1.



Figure 8.1: The rig set-up, with the camera in front, the steel plate on the work bench and the manipulator behind.

Session no.	Object parameters						
	Object			External optics		Atmosphere	
	Emissivity ϵ	Distance [m]	Reflected temp. [$^{\circ}$ C]	Temperature [$^{\circ}$ C]	Transmission	Atmospheric temp. [$^{\circ}$ C]	Relative humidity %
1	0.92	0.9	20	15	1.00	15	50
2	0.92	0.9	20	15	1.00	15	50
3	0.92	0.9	20	15	1.00	15	50
4	0.92	0.9	20	12	1.00	12	50
5	0.92	0.9	20	12	1.00	12	50
6	0.92	0.85	20	13	1.00	13	50
7	0.92	0.85	20	13	1.00	13	50
8	0.92	0.85	20	13	1.00	13	50

Table 8.1: Object parameters set in the camera for the different sessions

8.2.1 Session 1

A total of four strings were done, where the inter-pass temperature in each consecutive pass was 40°C in average along the centre-line. The strings were lay beside each other, and each string was 200 mm. The reason for the initial temperature being 15°C on the first string, was that the plate was at room temperature. The session was done with a weaving of 2 mm, which will make the string wider, and the resultant heat distribution will be less equal to that of a point source. This will introduce more uncertainties in the measurements compared to the reference calculated temperature.

String no.	Current [A]	Voltage [V]	Weld speed [mm/s]	Initial temp. [°C]	Measured $\Delta t_{8/5}$	Calculated $\Delta t_{8/5}$	Deviation [%]
1	240	26	8	15	2.90	1.76	64.77
2	275	29	9	40	3.81	2.17	75.44
3	275	29	8	40	4.28	2.44	74.86
4	260	27.75	8	40	3.64	2.21	64.37
Average deviation							69.87

8.2.2 Session 2

The session was completed with the same characteristics as in session 1 and with the parameters shown in the table below.

String no.	Current [A]	Voltage [V]	Weld speed [mm/s]	Initial temp. [°C]	Measured $\Delta t_{8/5}$	Calculated $\Delta t_{8/5}$	Deviation [%]
1	250	28	9	15	2.99	1.97	51.57
2	250	28	6	40	4.35	2.86	51.85
3	254	28	6	40	4.36	2.91	49.98
4	254	28	6	40	4.53	2.91	55.89
Average deviation							52.33

8.2.3 Session 3

The plate was preheated with heating elements. This was done in order to simulate a multi-pass environment. By installing heating elements on the work piece, it was possible to manipulate the initial temperature in the plate beyond room temperature and temperature

from previous strings. It proved to be difficult to get a perfectly uniform temperature distribution in the entire plate. The initial temperatures were taken as average temperatures along the line where the weld was supposed to be performed.

String no.	Current [A]	Voltage [V]	Weld speed [mm/s]	Initial temp. [°C]	Measured $\Delta t_{8/5}$	Calculated $\Delta t_{8/5}$	Deviation [%]
1	240	27	6	50	4.25	2.75	54.73
2	252	28	6	100 ¹	5.42	3.61	50.20
3	250	28	6	125 ¹	5.53	3.96	39.79
4	252	28	6	150 ¹	6.28	4.44	41.42
5	247	28	6	175 ¹	7.44	4.87	52.64
6	250	28	6	210	7.85	5.85	34.19
7	252	28	6	250	8.86	7.34	19.89
8	252	28	6	230 ¹	10.23	6.56	55.90
9	253	28	6	270	10.71	8.31	28.88
Average deviation							41.30

8.2.4 Session 4

This session was done with parameters spanning a wide interval regarding heat-input Q . It was done in order to complete the tests where the initial temperature was controlled, in the sense that the consecutive string in the session was not performed until the average temperature along the centre-line was 40 °C.

¹The actual initial temperatures were not measured, but only approximations. This makes the $\Delta t_{8/5}$ just an indication.

String no.	Current [A]	Voltage [V]	Weld speed [mm/s]	Initial temp. [°C]	Measured $\Delta t_{8/5}$	Calculated $\Delta t_{8/5}$	Deviation [%]
1	202	25.3	6	15	3.15	1.92	64.35
2	223	26.5	6	40	3.66	2.41	51.35
3	249	27.5	6	40	4.16	2.80	48.46
4	274	28.8	6	40	5.02	3.22	55.73
5	296	30.0	6	40	6.055	3.63	66.63
6	200	25.3	8	40	2.05	1.55	32.26
7	226	26.5	8	40	2.79	1.84	51.79
8	245	27.0	8	40	3.18	2.03	56.50
9	273	28.5	8	40	4.04	2.39	68.98
10	300	30.0	8	40	5.02	2.76	81.63
Average deviation							57.77

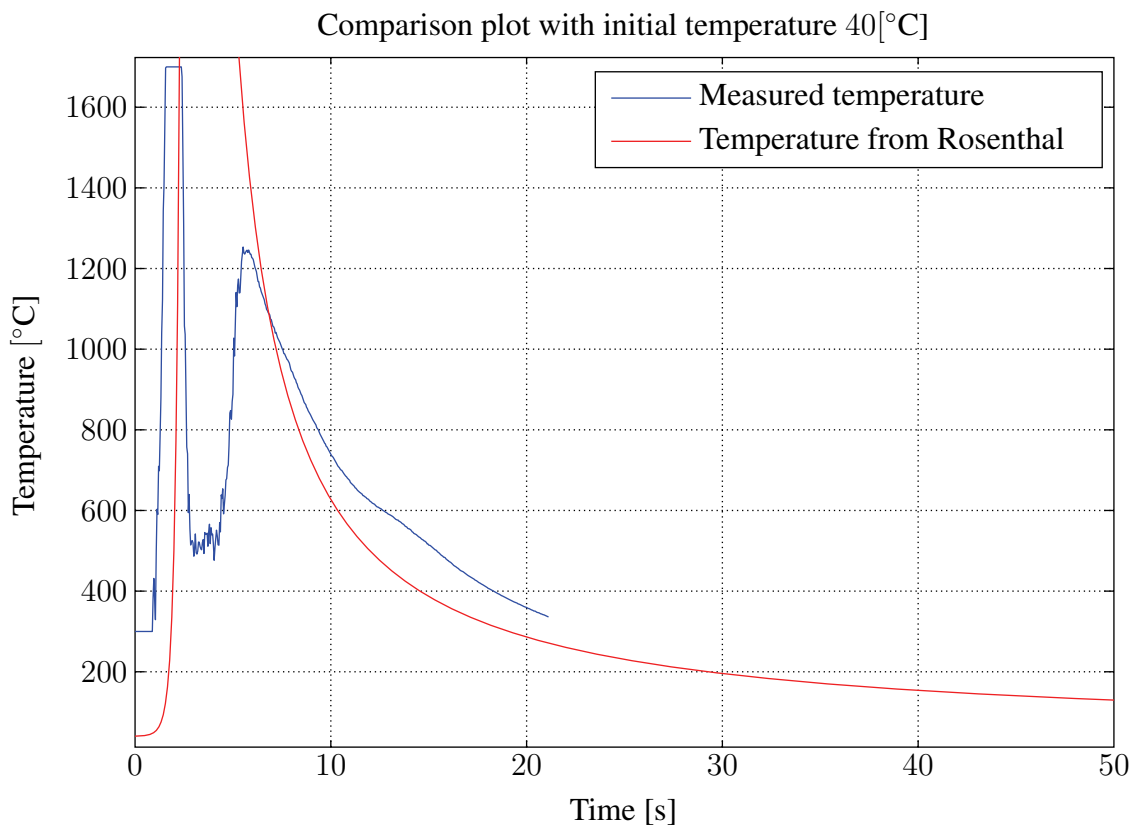


Figure 8.2: Comparison between Rosenthal and weld no.5 from session 4.

8.2.5 Session 5 and 6

There were lay 6 strings with a 10 seconds break in between each consecutive pass. To be able to monitor the initial temperature, two sessions where done with the same parameters. Session 5 was performed with the scale from 350 – 1500°C. Session 6 was done with a camera measurement-scale set to 0 – 500°C. By combining the results from the two sessions, it was possible to make an estimate on the temperature distribution for the entire temperature scale in the plate.

String no.	Current [A]	Voltage [V]	Weld speed [mm/s]	Initial temp. [°C]	Measured $\Delta t_{8/5}$	Calculated $\Delta t_{8/5}$	Deviation [%]
1	300	30	8	50.0	5.01	2.86	75.17
2	300	30	8	118.0	5.37	3.71	44.74
3	300	30	8	165.0	6.00	4.54	32.16
4	300	30	8	200.0	6.51	5.37	21.23
5	300	30	8	217.5	6.94	5.87	18.23
6	300	30	8	233.0	7.55	6.38	18.34
Average deviation							34.98

8.2.6 Session 7 and 8

Session 7 was done with the temperature scale set to 0 – 500°C on the camera. This was done in order to log the initial temperature of the welded specimen when doing session 8. In session 8 the scale was adjusted up to 300 – 1500°C, using the same parameters. It was assumed that the temperature distributions were the same for both sessions, making it possible to use the results from session 7 as initial temperatures when calculating $\Delta t_{8/5}$ for session 8. Both sessions were performed with pre-heating. The welds performed from string no. 3-6 were performed with a too high inter pass temperature according to specifications in (Helden & Dreyer 1999). The test was partially done to see how high a temperature it was possible to obtain in the plate.

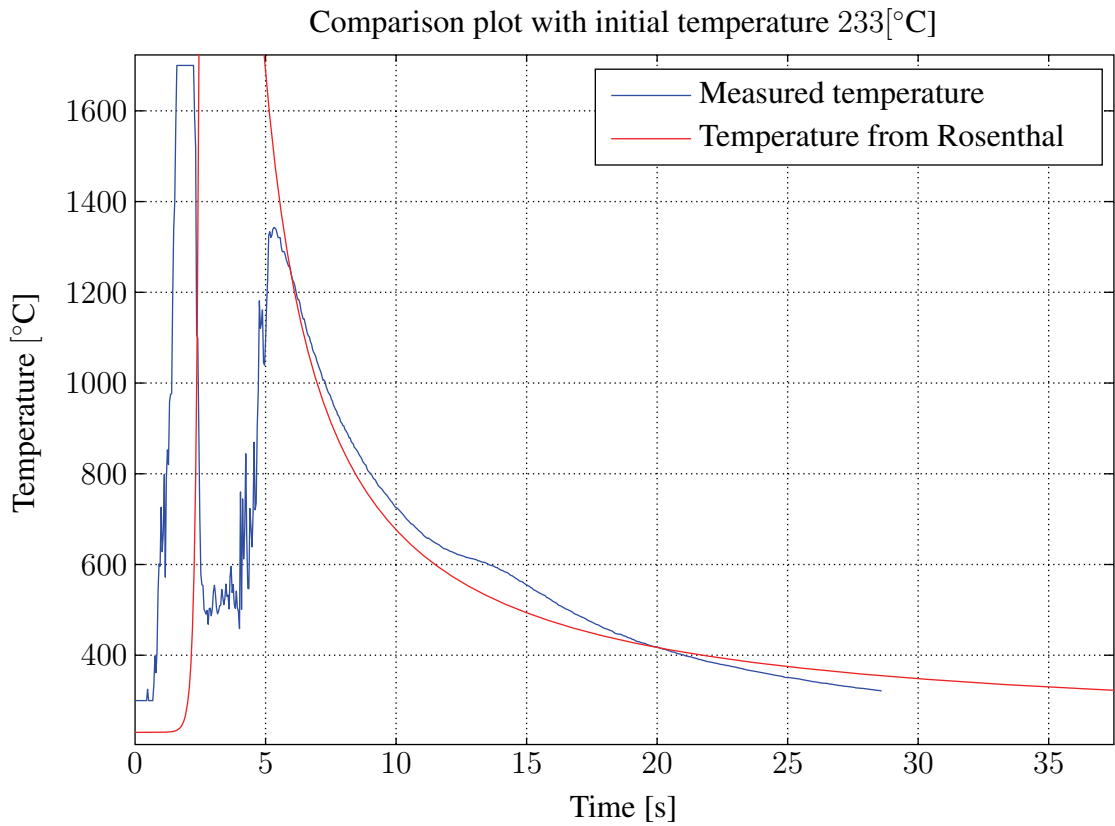


Figure 8.3: Comparison between Rosenthal and weld no.6 from session 5.

String no.	Current [A]	Voltage [V]	Weld speed [mm/s]	Initial temp. [°C]	Measured $\Delta t_{8/5}$	Calculated $\Delta t_{8/5}$	Deviation [%]
1	300	30	8	125.0	6.54	3.82	71.43
2	300	30	8	206.0	7.43	5.53	34.37
3	300	30	8	252.0	8.58	7.11	20.75
4	300	30	8	287.0	9.62	8.84	8.86
5	300	30	8	318.0	10.50	11.01	-4.61
6	300	30	8	337.0	11.26	12.80	-12.00
Average deviation							19.80

8.3 Hardness testing for quality confirmation

To investigate the quality of the welds performed, hardness tests were performed on macros on the welds from session 5 and 7. This was done with Vickers hardness test, which is described in (Hoshford 2005).

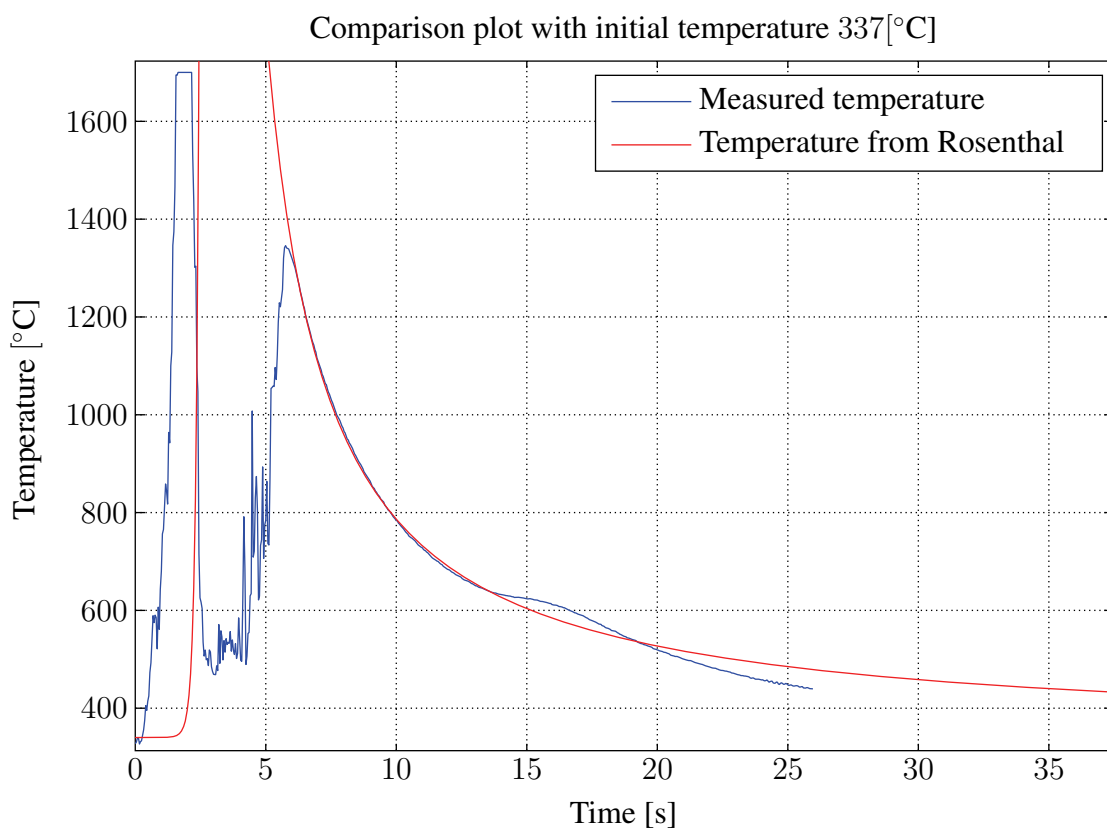


Figure 8.4: Plot comparing weld no. 6 session 8 with the solution of Rosenthal.

8.3.1 Quick review of Vickers hardness test

The test-rig uses a diamond shaped as a square pyramid, with an angle of 136° between opposite faces as an indenter Fig.8.5. The footprint made by the indenter is geometrically independent of the load applied to the material measured. The Vickers pyramid number (H_v) is then determined by the ratio F/A where F is force applied and A is the area made by the indentation. A is determined by

$$A = \frac{d^2}{2\sin(136^\circ/2)} \quad (8.1)$$
$$A \approx \frac{d^2}{1.854},$$

where d is the average length of d_1 and d_2 in Fig.8.5. This then gives rise to the number measuring hardness,

$$H_v = \frac{F}{A} \approx \frac{1.854F}{d^2} \left[\frac{kgf}{mm^2} \right]. \quad (8.2)$$

This is then converted to SI-units and $1kgf/mm^2 = 9.80665 \times 10^6 Pa$. When testing the hardness of the weld, one probes the points from 1-20 as shown in Fig.8.6. The requirements for steel in applications used in for example sub-sea installations, are hardness values H_v below 325. The hardness number will be highest in the transition between the base material and the HAZ, and will thus be the most critical regions.

8.3.2 Results from Vickers hardness test

The results from the hardness tests are summarized in Tab.E.1 and Tab.E.2. When looking at Fig.8.6, there is a total of 16 points to be probed. Because the welds were laid side by side with no space in between, the points close to the weld's surface are heat-affected by the subsequent string. This makes the hardness tested in the regions from point 1 – 7 and 15 – 16 not valid, and thus not tested. When looking at the tables in Appendix E, it may be concluded that all the welds are well within the demands for hardness in welds.

8.4 Discussion

The results in this chapter are obtained through Infra-red measurements of a steel plate at which welding with different parameters has been performed. The ultimate goal from the tests was to investigate the possibility to use the infra red camera to measure the temperature in the welded specimen, and use this information to control the $\Delta t_{8/5}$ in a multi pass welding environment. In order to draw any conclusions, a wide variety of trials were performed. This was done in order to stress relevant situations in a common welding setting. The tests were performed according to the tables seen in Section 8.2.1 through to 8.2.6. There will be put less emphasis on the two first sessions due to the use of weaving during welding. Weaving makes the heat source less equal to a point source, making the calculated solution invalid. The results from the two sessions are only presented as an indication.

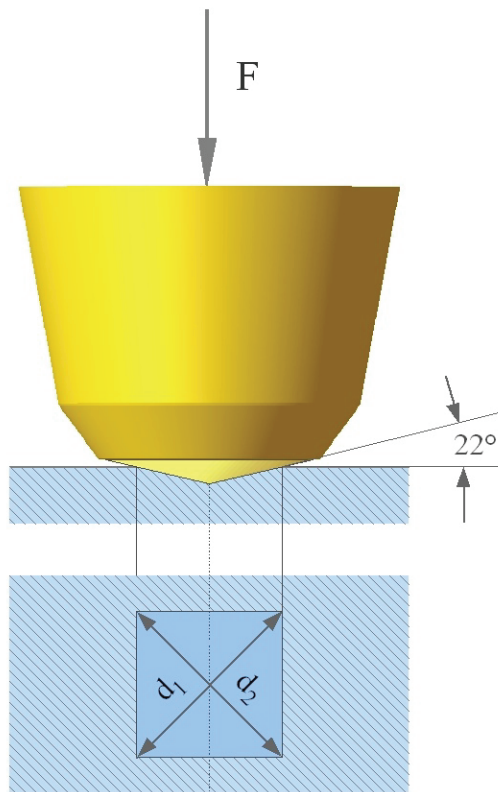


Figure 8.5: Schematic presentation of how the Vicker indenter is designed.

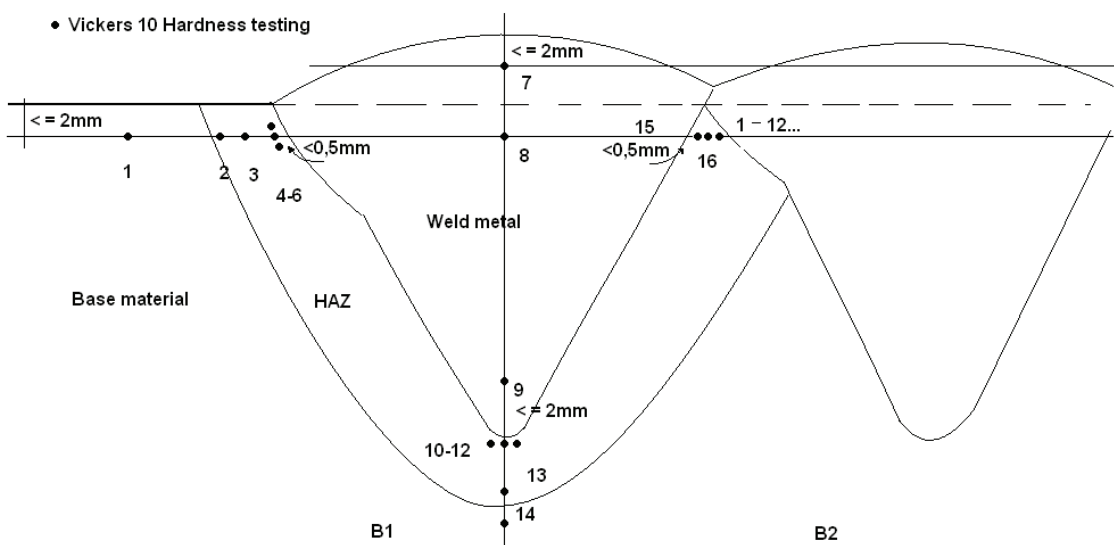


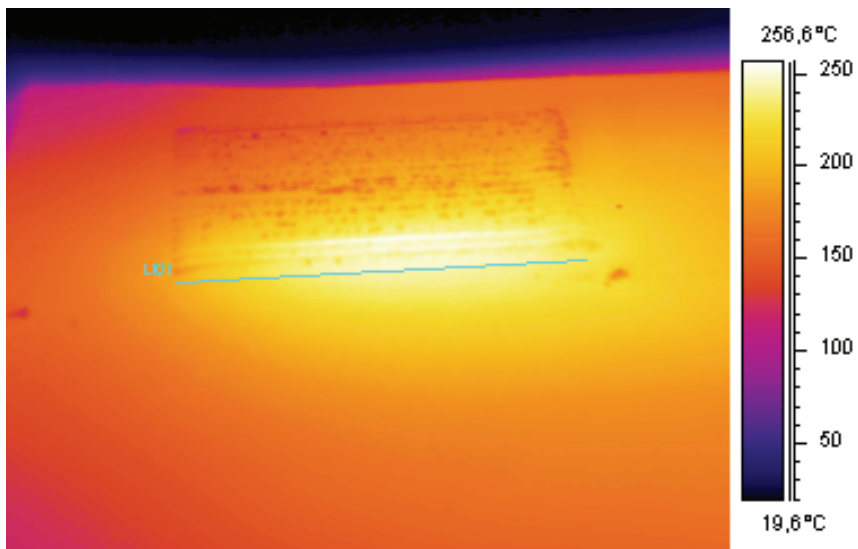
Figure 8.6: Schematic cross-sectional presentation of where the weld is probed to test hardness.

Looking at Section 8.2.3, the welding was performed with pre-heating. The initial temperature was not logged in all the samples, making the initial temperature for many of the strings uncertain. It proved to be difficult to create a uniform temperature distribution along the plate with pre-heating. As a compromise, the initial temperature was set to be the average temperature along the line at which the weld was supposed to be performed. Looking at Fig.8.7a, one can see the temperature distribution in the plate. The initial temperature was set to be the average temperature along the green line in the figure, in this case 230°C. If only concentrating on results from the strings where the initial temperature was known, one can see that the deviation between measured and calculated $\Delta t_{8/5}$ is between 19.89% and 54.73%. With an average of 41.30% on all the strings and an overall goal of 10%, the results are difficult to use.

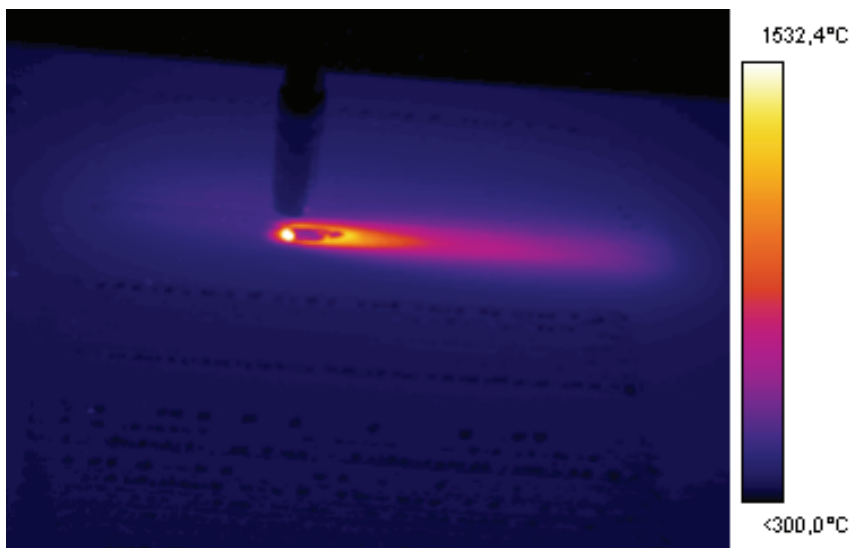
When looking at Section 8.2.4 through to 8.2.6 the same may be said, as above, when looking at the deviation in the $\Delta t_{8/5}$. The errors are averaged between 19.80% and 57.77%, and is clearly outside the desired result. There may be many reasons for this, and part of the problem may become obvious when looking at Fig.8.2 to Fig.8.4. The figures are a comparison between the analytical solution of Rosenthal and the measured temperature. The temperature is measured in a point, similar to that done in Chapter 7.

In general, the shape of the curves from the measurements show a significant difference from that of Rosenthal. In the first part of curve, the temperature has a rapid increase, until it stacks at 1700°C. This increase comes due to the heat in the arc between the weld-gun and the plate, and does not represent the temperature in the plate. After the arc has passed, the point of measurement experiences a decrease in temperature down to around 500°C. This effect may also be observed in Fig.8.7b, where one can see that the temperature behind the source is significantly lower in a certain area behind the heat source. This phenomena may be explained by the shielding gas cooling down the area around the weld-gun, creating a thin crust of solid on top of the liquefied welding pool. When the cooling effect of the shielding gas vanish, the underlying liquefied metal melts the thin solid crust forcing the temperature to rise again. In the late response of the curve, one can see that the decay rate deviates from a normal exponential decay rate. This is because in the interval between 800°C and 500°C, the austenite to ferrite transformation occurs. The plate exhales energy, and the temperature decays at a slower pace. This effect is not taken into account in the analytical model, and gives rise to one of the factors creating an error in the $\Delta t_{8/5}$ when comparing the two.

When closer investigating the tables, the $\Delta t_{8/5}$ is in general longer in the measured values than that in the analytical. It may also be observed that the deviation decreases as the initial temperature increases. When comparing Fig.8.2 through to Fig.8.4, the measured curve coincides with the Rosenthal curve in a significantly better way when the initial temperature is high. Part of the reason for this may be the difficulties in setting the parameters in Tab.8.1. By changing these parameters it is possible to change the temperature response to a certain extent, making the method of measure difficult to get accurate. In particular, the emissivity ϵ , is a parameter associated with great uncertainty. Emissivity in the object is a function of temperature. As the temperature fluctuates rapidly and over a great interval, the emissivity will change constantly.



(a) IR image of the temperature in the plate initially from session 3, weld 8.



(b) IR image of the temperature in the plate during welding from session 8, weld 6 .

Figure 8.7: IR temperature images from the trials.

Chapter 9

Conclusion

In this project there has been constructed a numerical mathematical model describing the complex nature of the partial differential equations governing the process of heat flow in steel plates.

The model itself was made in Chapter 6 with the FEM and compared to the thick plate solution of Rosenthal. Through consistency testing of the numerical model, it was established a relation between the model and the reference. As an initial goal, a temperature decay rate between 800°C and 500 °C within 10% of the reference model was set. This goal was reached with good margins. The maximum error being found to 3.22%, shows that results obtained are well within the scope of the project. This was done despite the fact that the model did not meet the semi-infinite body requirement.

In Chapter 7 the numerical model was put under the method of model reduction, which goal was to recreate the results above with the same goal regarding error. By optimizing the inputs to the linear system, a reduced model was possible to obtain with good performance. Through the tests performed, the reduced model, made with the compound matrix in Tab.7.1, managed to recreate the $\Delta t_{8/5}$ region with a maximum error of 0.9%. This is very good, even when comparing to the FEM-model from which the reduced model originates from. When input u was included into the system, problems regarding the heat input to the system arise. Only through extensive trial and error was it made possible to create an adequate response in the relevant regions. This makes the system vulnerable when used in an automated system, possibly making the wrong decisions if relying on the models response. The general dynamics in the system however, shows great adaptation, and is able to cope with a wide variety of inputs without introducing large errors. The results are promising, and through more research in modelling the heat-source, it should be possible to use the reduced model in an automated welding system.

When looking at the results obtained in Chapter 8, there are large errors present when comparing to the reference $\Delta t_{8/5}$. This then leads to the fact that at the moment, the measurements are not accurate enough to be used as a decision parameter in an automated welding system. However, the results show consistency, and with more tuning on the object parameters and identifying errors in the set up, it is possible to use this method in an automated system. It may also be concluded that the accuracy improved as the initial temperature of the welded specimen increased.

In order to create an automated welding system working under optimal conditions,

this project has found a possible entrance to the path completing the task. It still remains a huge amount work before it can be realized in a live environment.

9.1 Future work

To further close in on the ultimate goal of the project, there are a number of steps to be completed.

- Model a more reliable heat-source creating a temperature distribution in the welded specimen more equal to that of Rosenthal.
- Investigate the errors present in the IR-measurements and reduce the overall error making them suitable as decision parameters.
- Incorporate the reduced model in a closed loop temperature control system, controlling the $\Delta t_{8/5}$.
- Test the entire system in a live environment.

Bibliography

- Astrid, P. (2004), Reduction of Process Simulation Models: a proper orthogonal decomposition approach, PhD thesis, Technische Universiteit Eindhoven.
- Camp, K. A. E. & King, B. B. (1997), 'A comparison of balanced truncation techniques for reduced order controllers'.
URL: citeseer.ist.psu.edu/570217.html
- Cazemier, W. (1997), 'Proper orthogonal decomposition and low dimensional models for turbulent flows'.
URL: <http://irs.ub.rug.nl/ppn/161483305>
- Com (2005), *Comsol Multiphysics User's Guide version 3.2*.
- FLI (2006), *ThermaCAMTM S65 User's manual*, a156 edn.
- Grong, . (1994), *Metallurgical Modelling of Welding*, The Institute of Materials.
- Gugercin, S., Antoulas, A. C. & Beattie, C. A. (2004), 'First-order conditions and an iterative rational krylov algorithm for optimal \mathcal{H}_2 model reduction', *Technical report* .
- Gugercin, S. & Wilcox, K. (2007), 'Krylov projection framework for fourier model reduction', *provisionally accepted in Automatica* p. 7.
- Helden, P. O. & Dreyer, P. H. (1999), *Plate- og Sveise Håndbok*, Sveiseteknisk avdeling.
- Hoshford, W. F. (2005), *Mechanical behavior of materials*, Cambridge University Press.
- Hovland, S. & Gravdahl, J. T. (2006), 'Order reduction and output feedback stabilization of an unstable cfd model', *American Control Conference. Minneapolis, Minnesota* .
- Jiluan, P. (2003), *Arc Welding Control*, Vol. Developments in heat transfer vol. 14, Woodhead Publishing Limited, England.
- Karhunen, K. (1946), 'Zur spektral theorie stochasticher prozesse', *Ann. Acad. Sci. Fennicae, Ser. A1 Math Phys* **34**, 1–7.
- Loève, M. (1946), 'Fonctions aleatoire de second ordre', *Revue science* **84**, 195–206.
- Nguyen, N. (2004), *Thermal Analysis of welds*, WIT Press.

-
- Olsson, K. H. A. (2002), Model order reduction in femlab by dual rational arnoldi, Master's thesis, Göteborg university.
- Pires, J. N., Loureiro, A. & Bolmsjö, G. (2006), *Welding Robots : technology, system issues and applications*, Springer-Verlag London Limited.
- Reddy, J. N. (2006), *An Introduction to the Finite Element Method*, McGraw-Hill.
- Willcox, K. & Megretski, A. (2005), 'Fourier model reduction for large-scale applications in computational fluid dynamics', *SIAM, Journal on Scientific Computing* **Vol. 26, No. 3**, 944–962.

Appendices

Appendix A

Modelling of a single-pass weld

Procedure when creating the model describing a single pass weld in a 50mm thick plate. This procedure was done individually for each heat-input to the model in order to get a different temperature response.

A.1 Application modes and modules used in the model

- A 3D model which physical properties are heat transfer by conduction.
- A 1D model which is in a weak time dependent form.

A.2 Constants used in the model

Name	Expression	Description
u_{weld}	0.005	Welding speed [m/s]
T_0	300	Initial temperature in the plate [K]
Q	3.6×10^6	Heat input [W/m^3]
State	1	Heat source on/off

A.3 Geometries in the model

1. 3D model:

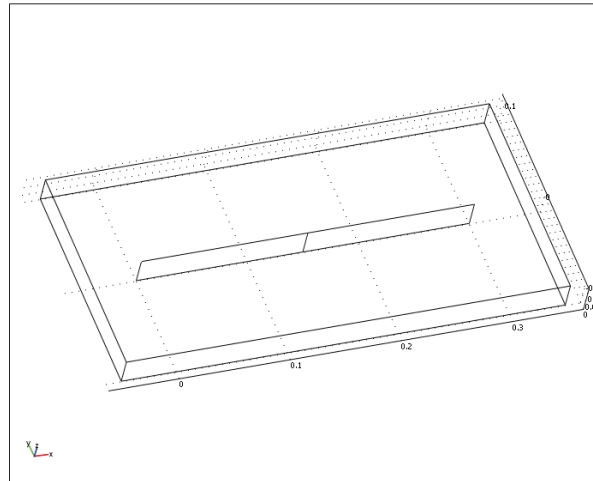


Figure A.1: 3D model geometry. Dimensions: $400 \times 200 \times 50$ [mm]

2. 1D model:

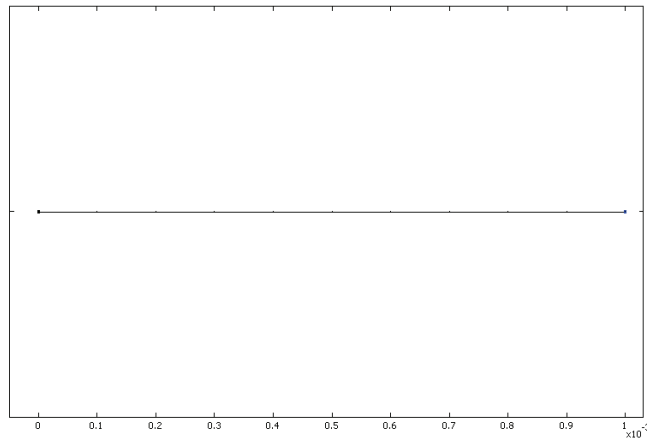


Figure A.2: 1D model geometry. Dimension: 1[mm]

A.4 Geometry 1, 3D

Description of the 3D model parameters and settings.

A.4.1 Mesh statistics

Number of degrees of freedom	5253
Number of edge elements	257
Number of boundary elements	3268
Number of elements	8890
Minimum element quality	0.256

A.4.2 Application mode: Heat Transfer by Conduction (ht)

Application mode type: Heat Transfer by Conduction Application mode name: ht

Application Mode Properties

Property	Value
Default element type	Lagrange - Linear
Analysis type	Transient
Frame	Reference frame
Weak constraints	Off

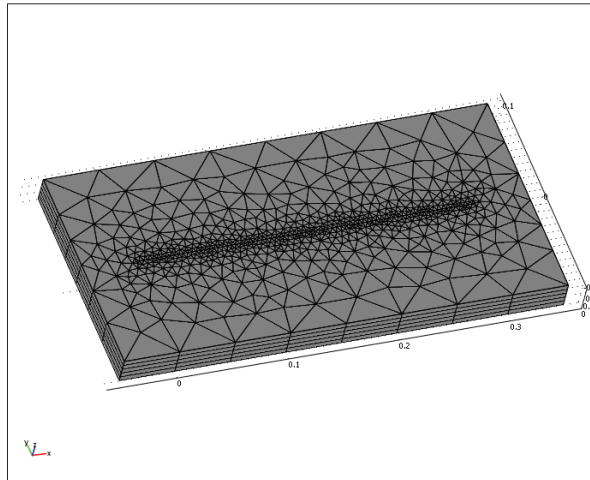


Figure A.3: Meshed 3D geometry

Variables

The variable for which the problem is solved for, is the temperature T .

Boundary Settings

All the boundaries in the model were set to thermal insulation.

Subdomain settings

The model was made in steel, AISI 4340. The following properties of the material was used in the model:

Thermal conductivity (k)	$\frac{W}{m \cdot K}$	44.5
Density (rho)	$\frac{kg}{m^3}$	7850
Heat capacity (C)	$\frac{J}{kg \cdot K}$	475

A.5 Geometry 2, 1D

Description of the 1D model and its parameters.

A.5.1 Scalar Expressions

Name	Expression
k_{abs}	$8 * 10^3 - 10(T - 300)$
u_{abs}	$k_{abs} * u$

A.5.2 Mesh statistics

The following mesh statistics are contained in the 1D-domain:

Number of mesh points	27	
Number of elements	27	
Number of boundary elements	1.0	
Element length ratio	0.159	
Boundary	1	2
Maximum element size	-	10^{-5}
Element growth rate	-	1.1

A.5.3 Application Mode: Weak Form, Subdomain w

Application mode type: Weak Form, Subdomain.

Application mode name: w

Application Mode Properties

Property	Value
Default element type	Lagrange - Quadratic
Wave extension	Off
Frame	Reference frame
Weak constraints	Off

Variables

Dependent variables: u, u_t

Shape functions: $\text{shlag}(2, 'u')$

Interior boundaries are not active.

Point Settings

Point	1	2
constr term (constr)	0	$1 - u$
style	$\{0, \{0, 0, 0\}\}$	$\{0, \{0, 0, 255\}\}$

Subdomain Settings

Subdomain	1
weak term	$(ux - u_{abs}) * State * u_{test} + Q * T_{test}$
dweak term	0
Subdomain initial value	1
u	1

A.6 Geometry 3

Space dimensions: 2D Independent variables: x,y and z.

Mesh Statistics

Number of boundary elements	104
Number of elements	1270
Minimum element quality	0.738
Number of mesh points	650

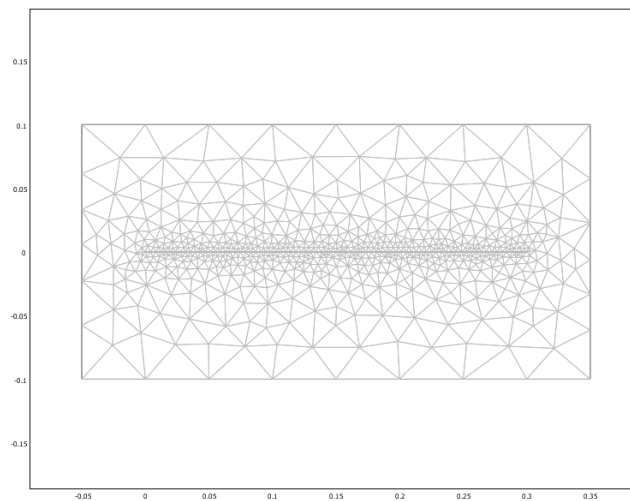


Figure A.4: 2D geometry after initialized mesh

A.7 Materials/Coefficients Library: Steel AISI 4340

Parameter	Value
Heat capacity (C)	475
Young's modulus (E)	$205 * 10^9$
Thermal expansion coeff. (alpha)	$12.3 * 10^{-6}$
Relative permittivity (epsilon _r)	1
Thermal conductivity (k)	44.5
Relative permeability (mu _r)	1
Poisson's ratio (nu)	0.28
Density (rho)	7850
Electrical conductivity (sigma)	$4.032 * 10^6$

A.8 Extrusion Coupling Variables: Geom 1, Source Subdomain: 1

Name	Value
Expression	T
Transformation type	General
Source transformation	x, y, z
Destination Subdomain	1 (Geom2) $u_weld * t, 0, x$

A.9 Solver Parameters

Analysis type	Transient
Auto select solver	On
Solver	Time dependent
Solution form	Automatic
Symmetric	Off
Adaption	Off

A.9.1 Direct(UMFPACK)

Solver type: Linear system solver.

Parameter	Value
Pivot threshold	0.1
Memory allocation factor	0.7

A.9.2 Time Stepping

Parameter	Value
Relative tolerance	0.01
Absolute tolerance	1
Times to store in output	Specified times
Time steps taken by solver	Free
Initial time step	0.0010
Maximum time step	1.0
Maximum BDF order	5
Singular mass matrix	Maybe
Consistent initialization of DAE systems	Backward Euler
Error estimation strategy	Include algebraic
Allow complex numbers	Off

A.9.3 Advanced options

Parameter	Value
Constraint handling method	Elimination
Null-space function	Automatic
Assembly block size	5000
Use Hermitian transpose of constraint matrix	Off
Use complex functions with real input	Off
Type of scaling	Automatic
Row equilibration	On
Manual control of reassembly	On
Load constant	On
Constraint constant	On
Mass constant	On
Damping (mass) constant	On
Jacobian constant	On
Constraint Jacobian constant	On

A.10 Variables

A.10.1 Boundary Variables

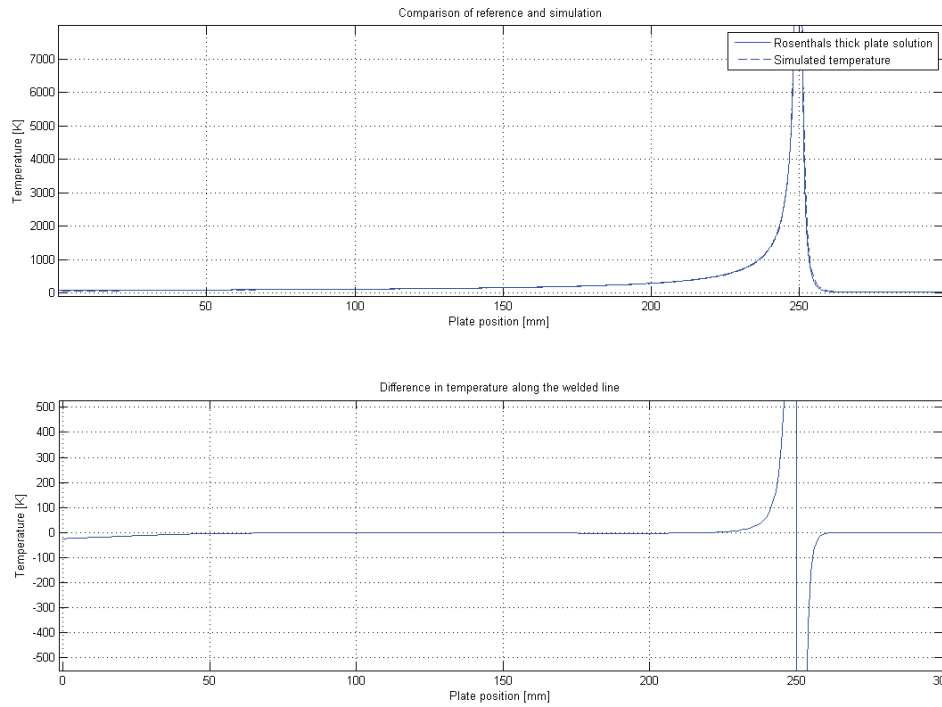
Name	Description	Expression
$nflux_{ht}$	Normal heat flux	$n_{x_{ht}} * flux_{x_{ht}} + n_{y_{ht}} * flux_{y_{ht}} + n_{z_{ht}} * flux_{z_{ht}}$

A.10.2 Subdomain Variables

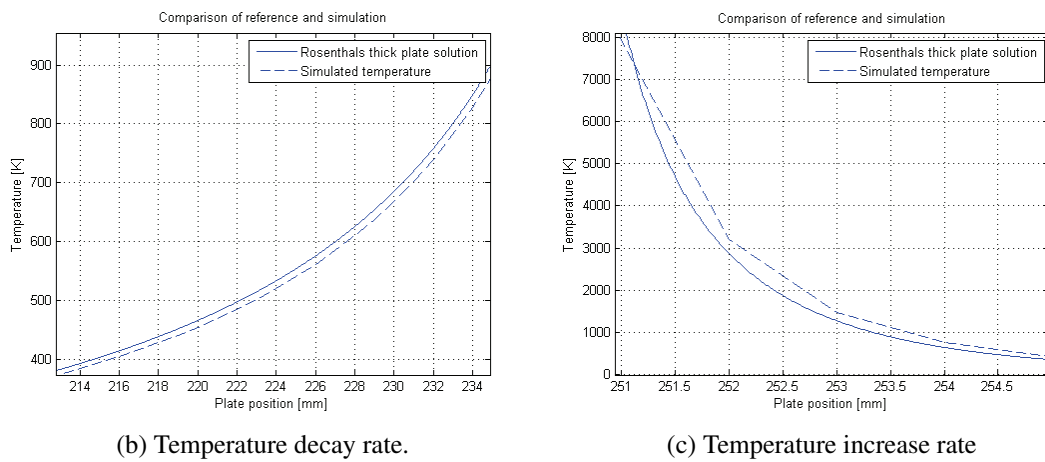
Name	Description	Expression
$flux_{x_{ht}}$	Heat flux, x component	$-(k_{xx_{ht}} * T_x + k_{xy_{ht}} * T_y + k_{xz_{ht}} * T_z)$
$flux_{y_{ht}}$	Heat flux, y component	$-(k_{yx_{ht}} * T_x + k_{yy_{ht}} * T_y + k_{yz_{ht}} * T_z)$
$flux_{z_{ht}}$	Heat flux, z component	$-(k_{zx_{ht}} * T_x + k_{zy_{ht}} * T_y + k_{zz_{ht}} * T_z)$
$gradT_{ht}$	Temperature gradient	$\sqrt{T_x^2 + T_y^2 + T_z^2}$
$flux_{ht}$	Heat flux	$\sqrt{flux_{x_{ht}}^2 + flux_{y_{ht}}^2 + flux_{z_{ht}}^2}$

Appendix B

Figures relevant for Chapter 6



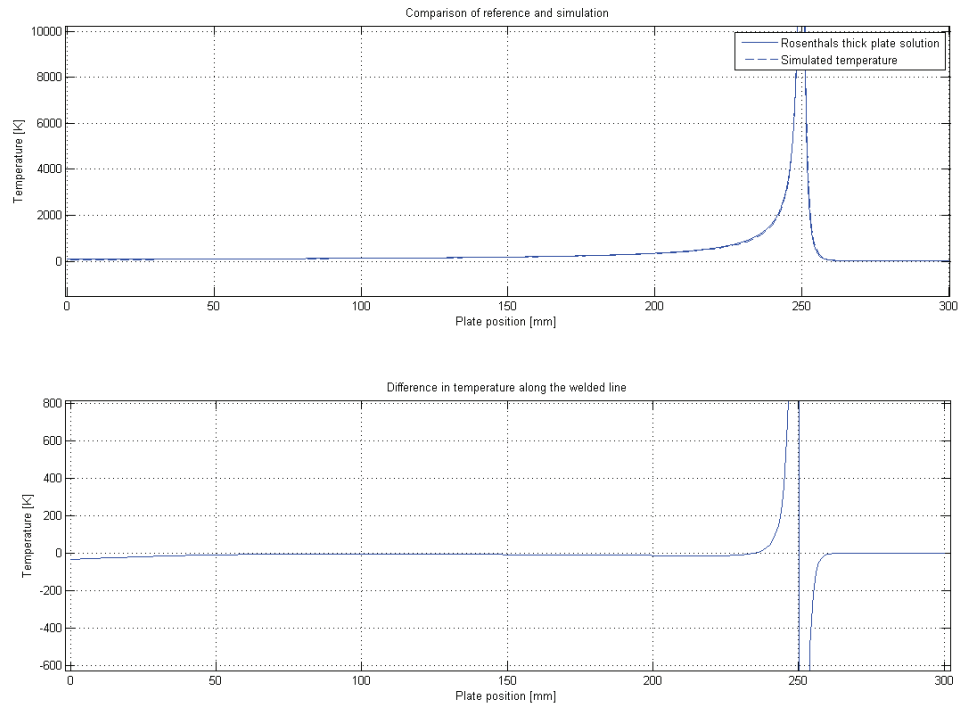
(a) Direct comparison of the temperature and temperature-difference in the responses.



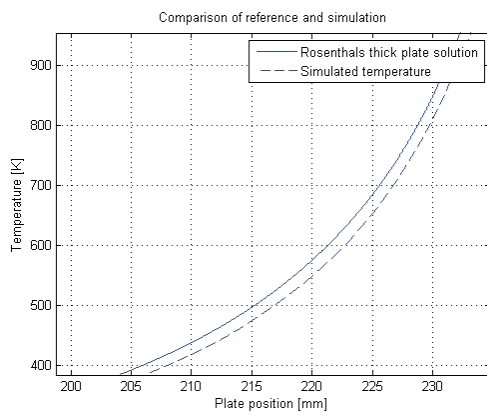
(b) Temperature decay rate.

(c) Temperature increase rate

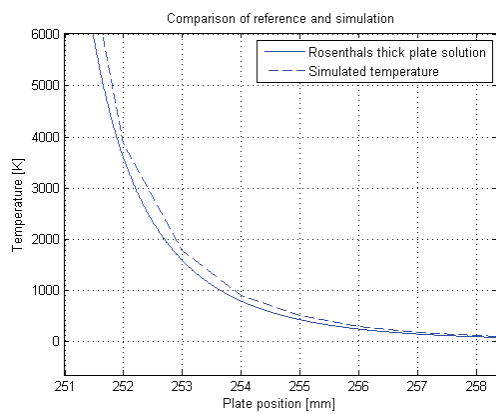
Figure B.1: Comparison plots of the from trial number 2. Input into Rosenthal: $I = 200$ [A], $U = 23$ [V] and $\eta = 0.8$.



(a) Direct comparison of the temperature and temperature-difference in the responses.

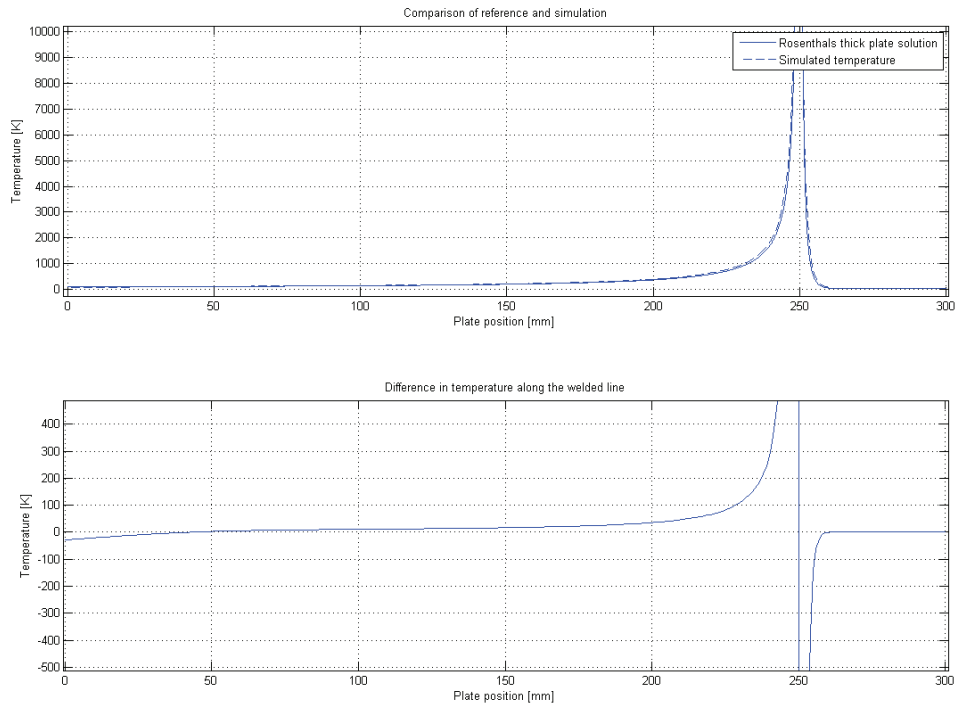


(b) Temperature decay rate.

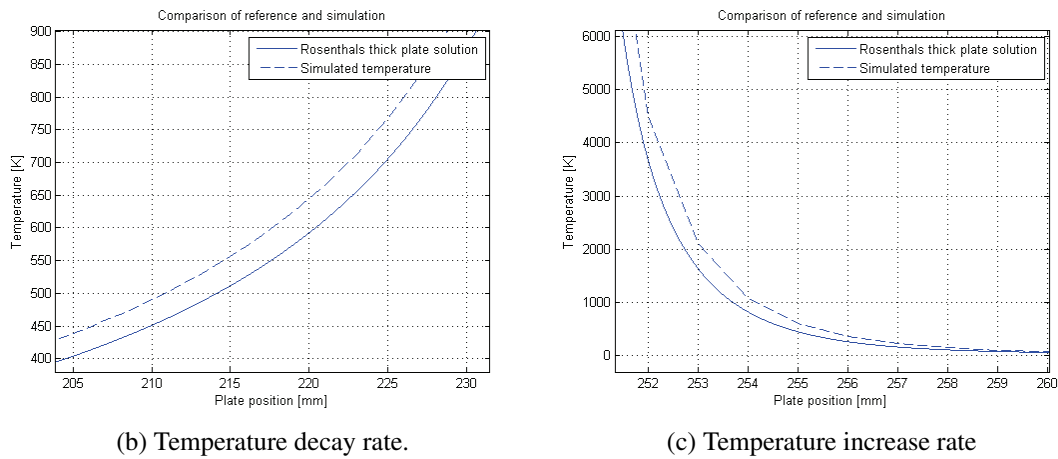


(c) Temperature increase rate

Figure B.2: Comparison plots of the from trial number 3. Input into Rosenthal: $I = 250$ [A], $U = 23$ [V] and $\eta = 0.8$.



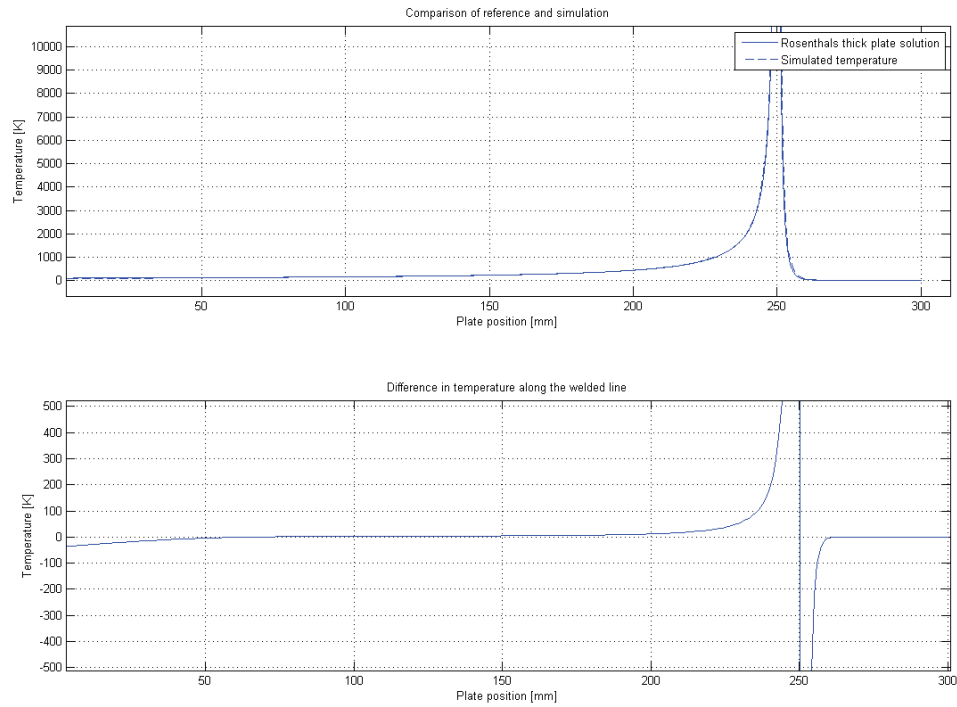
(a) Direct comparison of the temperature and temperature-difference in the responses.



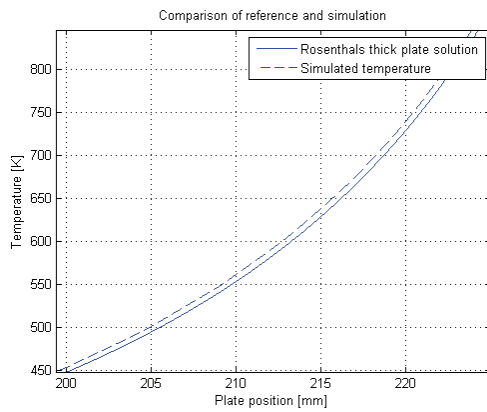
(b) Temperature decay rate.

(c) Temperature increase rate

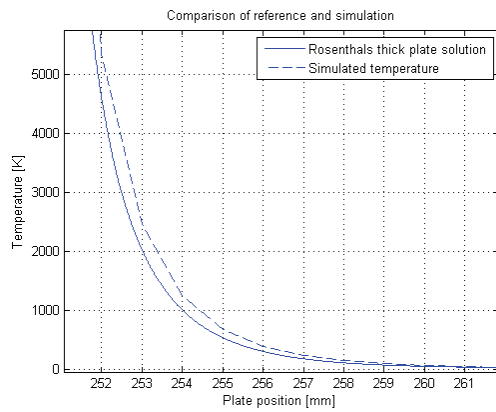
Figure B.3: Comparison plots of the from trial number 4. Input into Rosenthal: $I = 275$ [A], $U = 23$ [V] and $\eta = 0.8$.



(a) Direct comparison of the temperature and temperature-difference in the responses.



(b) Temperature decay rate.



(c) Temperature increase rate

Figure B.4: Comparison plots of the from trial number 5. Input into Rosenthal: $I = 320$ [A], $U = 23$ [V] and $\eta = 0.8$.

Appendix C

Figures relevant to Chapter 7

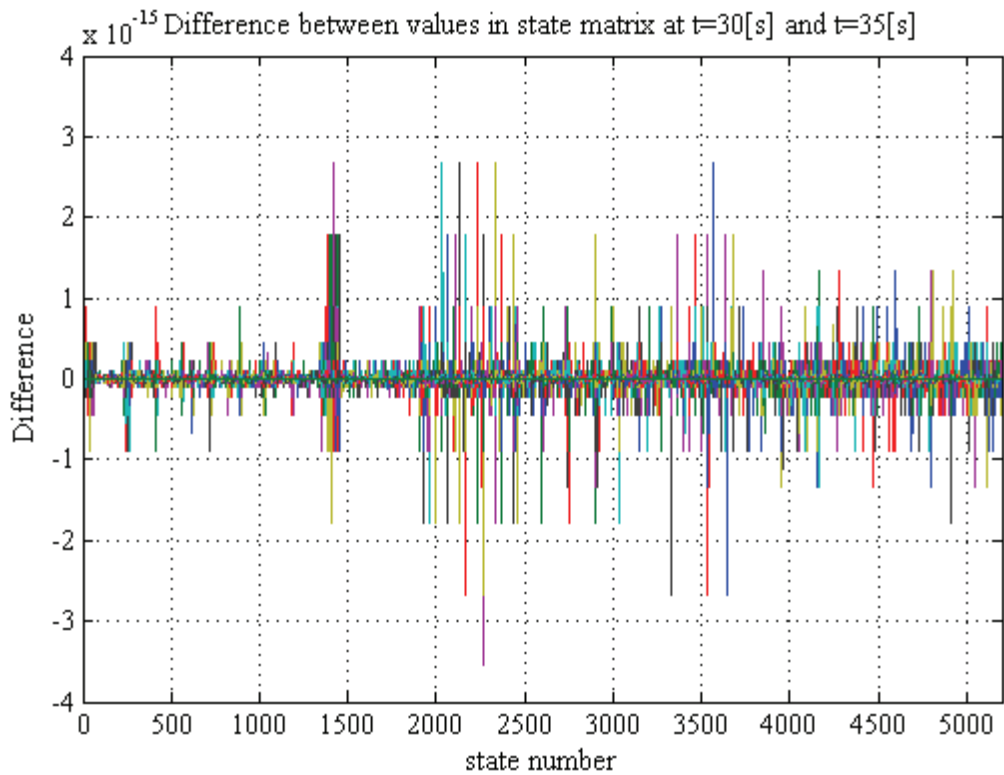
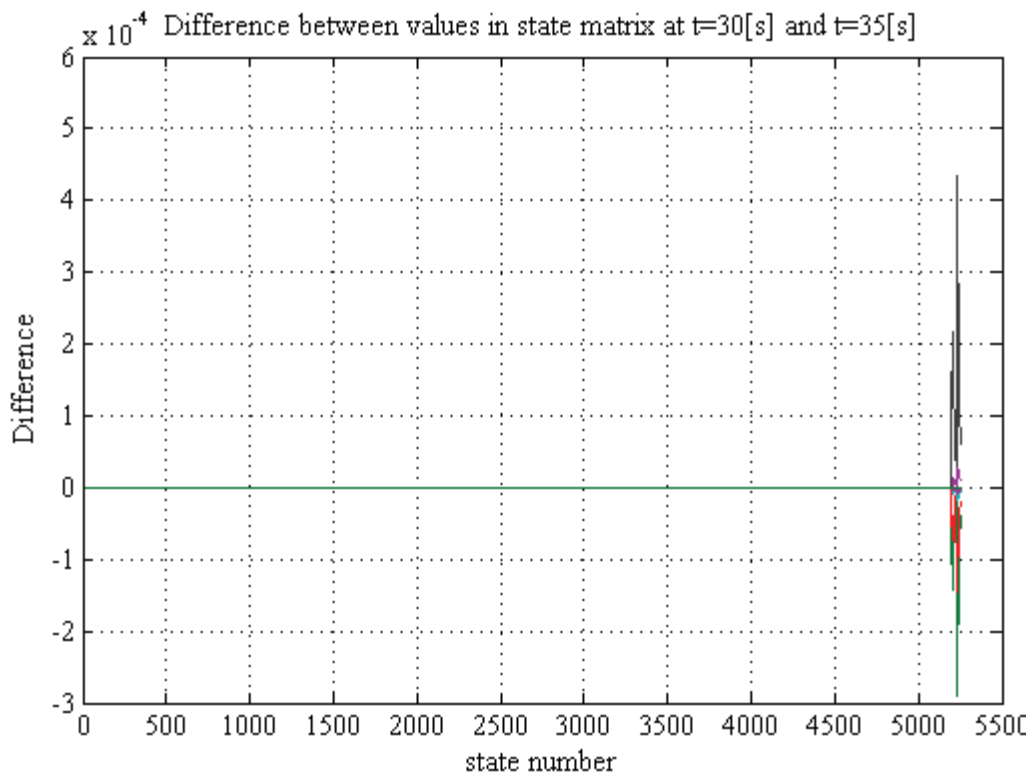


Figure C.1: Difference in the state matrix values from linearization time $t_0 = 30[s]$ and $t_0 = 35[s]$.

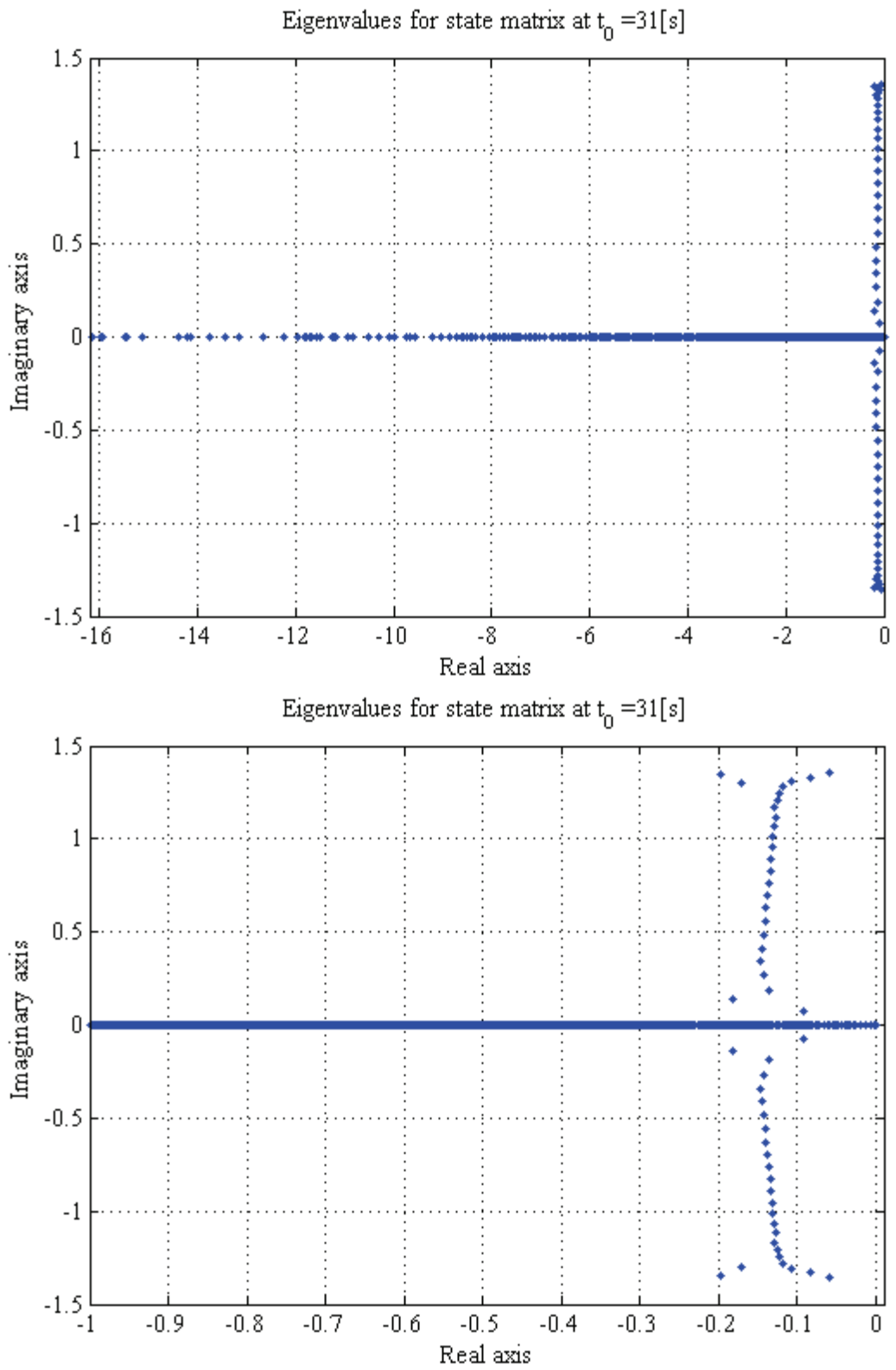


Figure C.2: The state matrix eigenvalues for linearization point $t_0 = 31[s]$

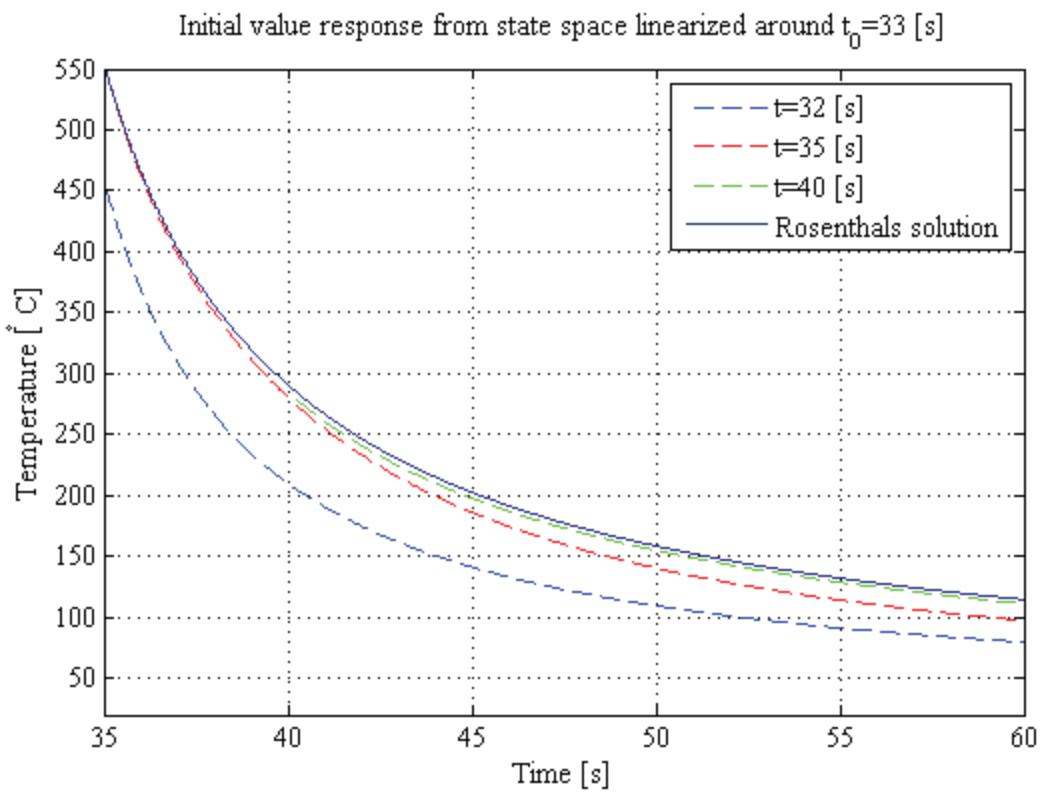
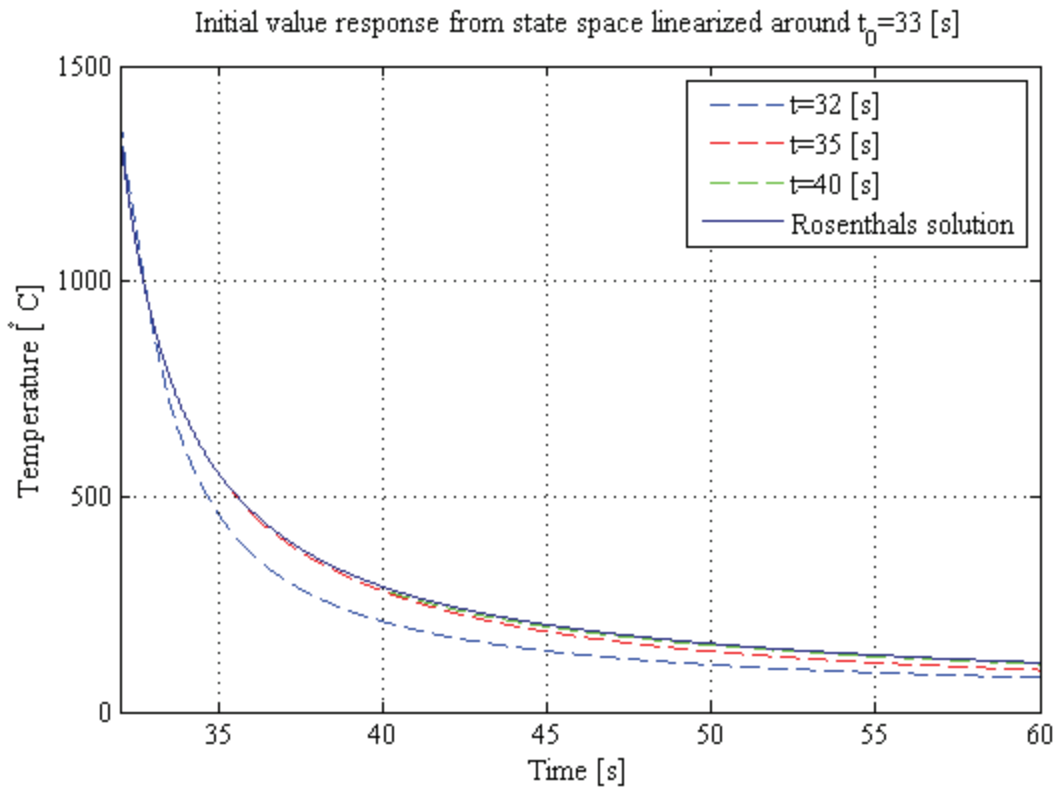


Figure C.3: Comparison plot of different full rank linear model initial value problems and Rosenthal.

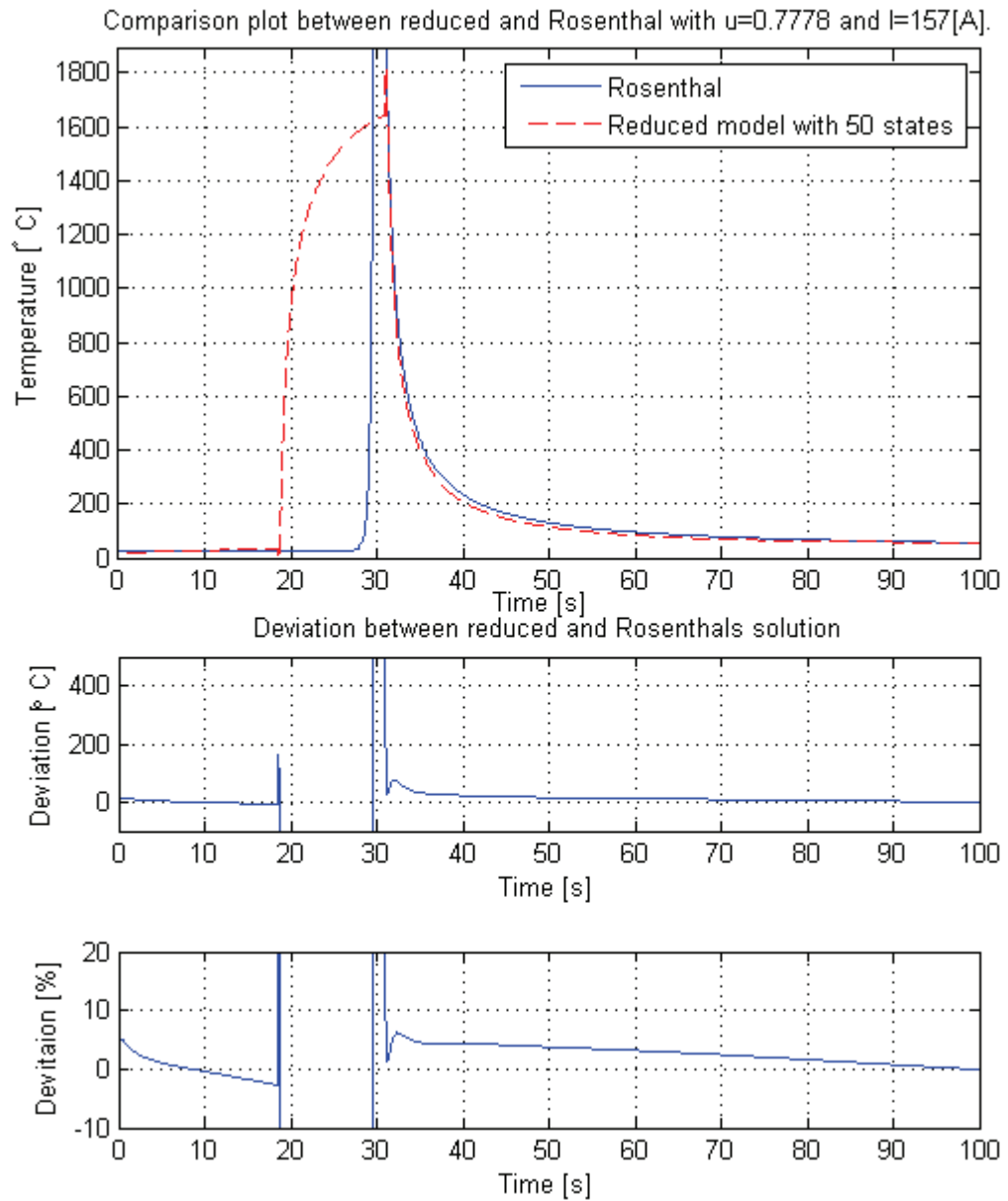


Figure C.4: Comparison plot between reduced model and Rosenthal. Heat input similar to that of trial no. 1 Tab.6.1

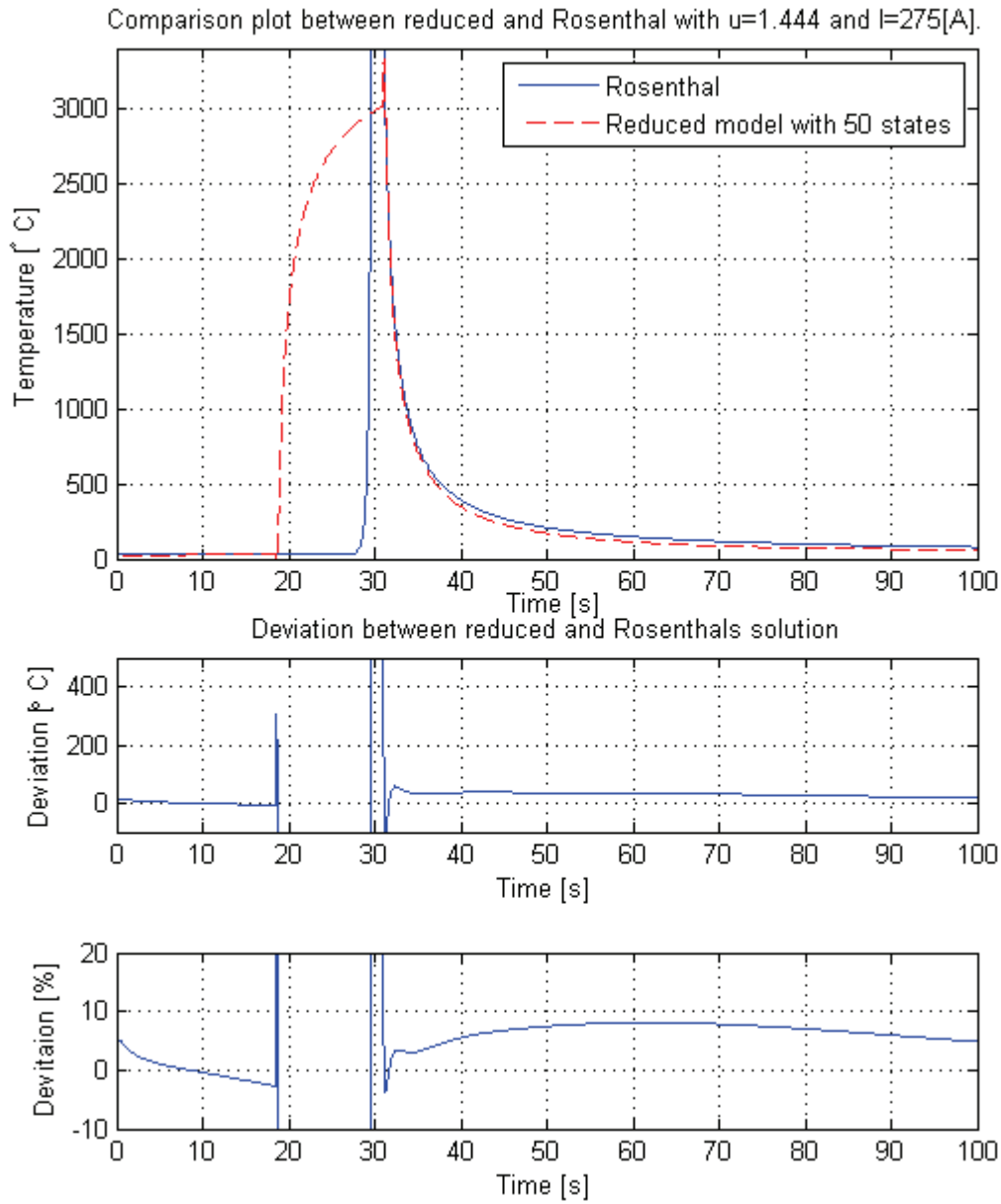


Figure C.5: Comparison plot between reduced model and Rosenthal. Heat input similar to that of trial no. 4 Tab.6.1

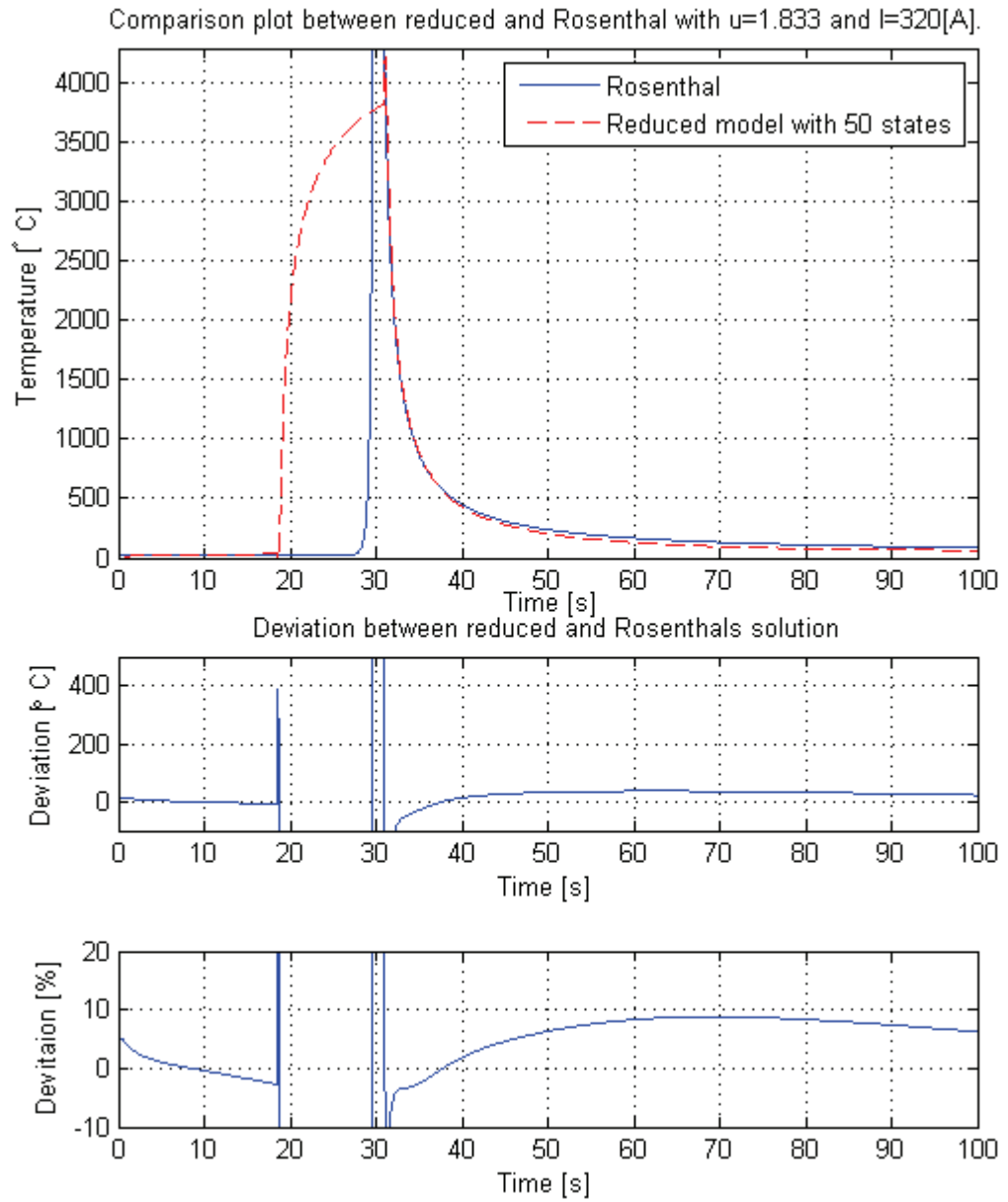


Figure C.6: Comparison plot between reduced model and Rosenthal. Heat input similar to that of trial no. 5 Tab.6.1

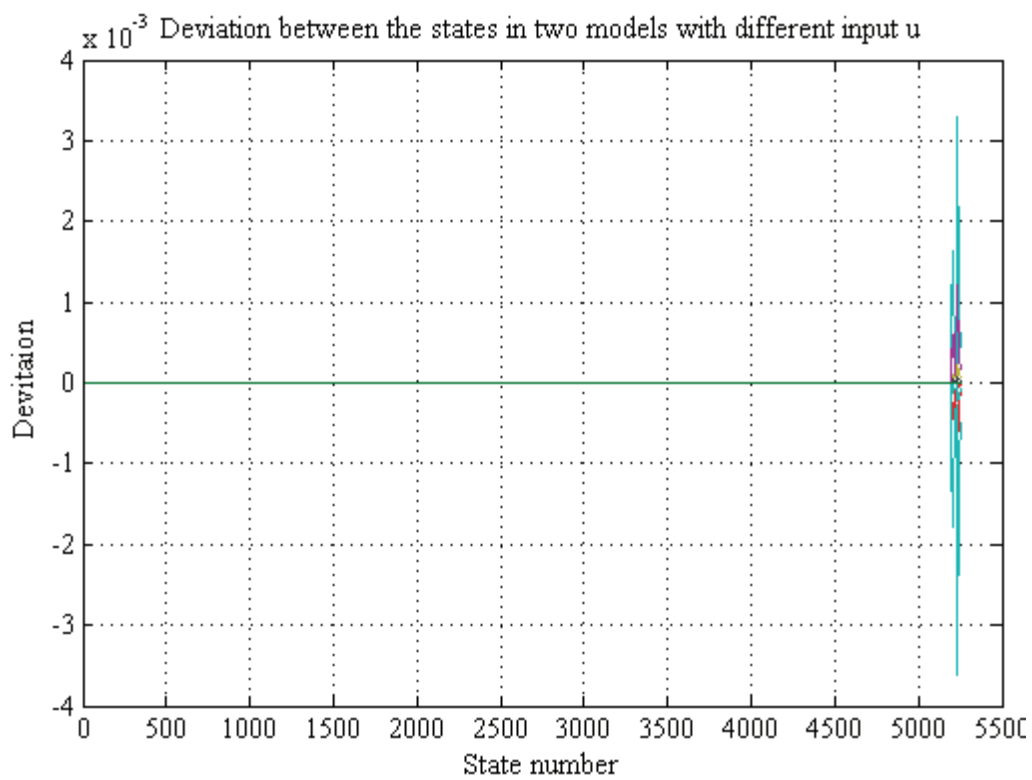


Figure C.7: Comparison between full rank state space models linearized around $t_0 = 31[s]$ with two different heat inputs u . The difference is between models from trial no. 2 and 4 in Tab.6.1.

Appendix D

ThermaCAMTM S65



Figure D.1: The ThermaCAMTM S65 infrared camera

IMAGING PERFORMANCE

Field of view/min focus distance	24° × 18° /0.3 m (with 35 mm lens)
Spatial resolution	1.3 mrad
Accuracy	2°C
Thermal sensitivity	0.08°C at 30°C
Focusing	Automatic or manual focus
Electronic zoom function	2x, 4x, 8x interpolating
Digital image enhancement	Adaptive digital noise reduction
Built-in digital video	640 × 480 pixels, full color
Detector type	Focal Plane Array (FPA), uncooled micro bolometer (320 × 240 pixels)
Spectral range	7.5 to 13μm
Image frequency	50/60 Hz, non-interlaced

IMAGE PRESENTATION

Image output	RS170 EIA/NTSC or CCIR/PAL analog composite video and FireWire (IEEE-1394) 8/16-bit digital image output.
--------------	---

MEASUREMENT

Temperature ranges	−40°C up to +1500°C
Accuracy	±2°C, ±2% of reading
Measurement modes	Spot (up to 6), area (4), isotherm, Δ T
Emissivity corrections	Variable from 0.1 to 1.0
Reflected ambient temperature	Automatic, based on input of reflected temperature correction
External optics / window correction	Automatic, based on input of optics/window transmission and temperature

POWER SOURCE

AC operation	AC adapter 110/220 V AC, 50/60 Hz
Voltage	10/30V nominal, < 6W

ENVIRONMENTAL SPECIFICATIONS

Operating temperature range	-15°C to +55°C
Storage temperature range	-40°C to +70°C
Humidity	Operating and storage 10% to 95%, non condensing
Encapsulation	IP 40 (determined by connector type)
Shock	Operational: 25 G, IEC 68-2-29
Vibration	Operational: 2 G, IEC 68-2-6

PHYSICAL CHARACTERISTICS

Weight, including battery and RC	2.17kg
Size	234mm×124mm×161mm
Tripod mounting	Standard 1/4" – 20

INTERFACES

Digital image output and camera control	6-pin FireWire (IEEE-1394) connector handling isochronous. 16-bit digital image data and asynchronous control data
BNC	Composite video (NTSC/PAL)
6-pin screw terminal (upper)	Digital I/O: 3 Output- 1 Input 1 Input/Output selectable. User configurable*
6-pin screw terminal (lower)	Analog I/O: 2 Output - 1 Input, User configurable*

USER CONFIGURATION TABLE*		
TYPE	FUNCTION	REMARK
Digital input	TTL: Shutter disable, Store image, Batch enable	Isolation and relay function in external module
Digital output	TTL Level: Spot / Area threshold alarm, Internal temperature sensor alarm, V-sync	Isolation and relay function in external module
Analog Output	Spot/Area out 0 – 5 V, Internal temperature sensor alarm, V-sync	Scaled to T-low - T-high isolation in external module
Analog input	External temperature sensor in 0 – 10V	Scaled to T-low - T-high isolation external module

Appendix E

Results from Vicker 10 hardness test

The following tables are the results obtained from the hardness tests performed on the macros made after the weld-experiments at AKV.

1	String no.	8	9	10	11	12	13	14
	Diag1	282	277	285	294	301	303	308
	Average	279.4	289.3	291.0	292.0	302.0	305.0	309.0
2	Vicker 10 H_v	237.5	221.6	219	217.4	203.3	199.3	194.2
	Trial no./String no.	8	9	10	11	12	13	14
	Diag1	278	272	300	298	305	308	310
3	Average	274.7	289.5	299.0	302.5	306.5	310.0	320.5
	Vicker 10 H_v	245.6	229.0	207.4	202.6	197.3	193.0	180.5
	Trial no./String no.	8	9	10	11	12	13	14
4	Diag1	278	285	300	293	307	303	312
	Average	281.5	286.0	299.0	296.5	305.0	305.0	313.5
	Vicker 10 H_v	234.0	226.6	207.4	211.0	199.3	199.3	188.6
5	Trial no./String no.	8	9	10	11	12	13	14
	Diag1	292	286	295	301	310	302	310
	Average	288.7	288.5	290.7	300.0	306.0	310.7	319.5
6	Vicker 10 H_v	222.4	222.7	219.4	206.0	198.0	192.0	181.6
	Trial no./String no.	8	9	10	11	12	13	14
	Diag1	292	290	300	312	306	305	316
7	Average	291.0	292.5	297.0	309.0	307.0	310.5	314.5
	Vicker 10 H_v	218.9	216.7	210.2	194.2	196.7	192.3	187.4
	Trial no./String no.	8	9	10	11	12	13	14
8	Diag1	286	290	310	304	305	300	316
	Average	288.0	294.5	308.0	309.5	304.5	308.0	316.5
	Vicker 10 H_v	223.5	213.7	195.4	193.5	200.0	195.4	185.0

Table E.1: Hardness results from session 5.

String no.	8	9	10	11	12	13	14
Diag1	297	299	296	291	300	304	307
Diag2	297	299	304	291	300	299	318
Average	298.0	296.0	304.0	295.5	299.5	305.5	318.0
Vicker 10 H_v	209.0	212.0	201.0	212.3	206.7	198.6	183.0
Trial no./String no.	8	9	10	11	12	13	14
Diag1	283	297	281	285	293	298	296
Diag2	283	297	281	285	293	298	296
Average	290.0	283.0	295.5	291.5	298.0	311.0	317.0
Vicker 10 H_v	220.5	231.2	212.3	218.2	208.7	191.7	185.0
Trial no./String no.	8	9	10	11	12	13	14
Diag1	286	282	284	288	299	286	287
Diag2	286	282	284	288	299	286	287
Average	283.5	286.0	299.0	292.5	289.4	307.5	303.5
Vicker 10 H_v	230.6	226.6	207.4	216.7	221.3	196.1	201.3
Trial no./String no.	8	9	10	11	12	13	14
Diag1	279	281	291	284	304	303	303
Diag2	279	281	291	284	304	303	303
Average	280.0	287.7	304.5	307.0	305.5	307.5	304.2
Vicker 10 H_v	236.5	224.0	200.0	196.7	198.6	196.0	200.3
Trial no./String no.	8	9	10	11	12	13	14
Diag1	297	288	322	311	318	294	301
Diag2	297	288	322	311	318	294	301
Average	292.5	316.5	316.0	304.0	317.5	297.5	327.0
Vicker 10 H_v	217.0	185.0	185.6	200.6	183.9	209.5	173.4
Trial no./String no.	8	9	10	11	12	13	14
Diag1	279	290	288	287	284	292	297
Diag2	279	290	288	287	284	292	297
Average	284.5	287.5	295.0	284.5	288.0	297.0	311.5
Vicker 10 H_v	229.0	224.3	213.0	229.1	223.5	210.5	191.1

Table E.2: Hardness results from session 7.

Appendix F

Sample Welding

AKER KVÆRNER™		WELDING PROCEDURE QUALIFICATION RECORD (WPQR)				WPQR no: Test					
Ref.:		Date:		Ref. stand.:		Rev.:					
Prod. by: AKV		Client:		Ref. stand.:		Page 1 of 2					
Project:		Ref. spec.:		Exam. body:							
Location:		Ref. pWPS:									
Welding processes		1 G-TIG (ROBOT)		2		3					
Shielding gas types		Ar-CO ₂									
Weaving (yes/no)		yes max.: 2 mm		max.: mm		max.: mm					
Purging gas type		l/min									
Welding positions											
Joint type											
Joint preparation											
Cleaning method											
Backing											
Single/double											
Back gouging											
Flux designation											
Flux handling											
Tungsten electrode		mm									
Torch angle		90°									
Stand off distance		15 mm									
Nozzle diameter(s)											
Tack welding proc.		Rev.									
Identification of parent metal		I C max:		CE max:		PCM max:					
II C max:		CE max:		PCM max:							
Part	Name/Grade	Standard	Group	Delivery cond.	Heat no.	Thickness (mm)	Diameter (mm)				
I											
II											
Identification of filler metal											
Index	Trade name	Classification		Group	Filler handling						
1											
2											
3											
Welding parameters											
Equipment:											
Pass no.	Index	Dia. (mm)	Welding process	Wire feed speed (m/min)	Current (A)	Voltage (V)	Current / Polarity	Welding speed (mm/min)	Run-out length (mm)	Gas (l/min)	Heat Input (kJ/mm)
10	C4			9.5 -	257 ± 3	22.5-23.5	+	348 - 5.8			1.619 -
11	C5			8.5 -	240 ± 3			348 - 5.8			-
12	C6			8.5 -	245 ± 3			342 - 6.2			-
13	B6			9.5 -	270 ± 3			342 - 6.2			-
14	B5			7.0 -	210 ± 3			330 - 5.5			-
15	B3			6.5 -	195 ± 3			330 - 5.5			-
16	B4			6.0 -	200 ± 3			330 - 5.5			-
17	B2			5.5 -	185 ± 3			330 - 5.5			-
18	B1			5.0 -	175 ± 3			330 - 5.5			-
				5.5	185 ± 3			306			-
Heat treatment											
Preheat min: °C		Interpass temp. max.: °C		Heat treatment proc.:		Temp. control:					
PWHT min: °C		max.: °C		Soaking: min.		Heating rate: °C/h					
						Cooling rate: °C/h					
Remarks:				Name of welder		Stamp					
				Additional info enclosed (Yes/No):		Date/signature:					
						Approved					

Appendix G

Matlab code and FEM-model

The CD contains Matlab files making it possible to recreate the results obtained throughout the project in addition to the FEM-model used.